

ADVANCED CHARACTERIZATION OF ULTRA-THIN TETRAHEDRAL
AMORPHOUS CARBON OVERCOATS FOR HIGH AREAL DENSITY
MAGNETIC RECORDING



A Thesis Submitted in Partial Fulfillment of the Requirements for the
Degree of Doctor of Philosophy in Applied Physics
Suranaree University of Technology
Academic Year 2021

การวิเคราะห์ชั้นสูงของฟิล์มทีเอ-คาร์บอนชนิดบางมาก
สำหรับฮาร์ดดิสก์ที่มีความจุสูง



นายวรินทร์ ชาตะรัตน์

วิทยานิพนธ์นี้เป็นส่วนหนึ่งของการศึกษาตามหลักสูตรปริญญาวิทยาศาสตรดุษฎีบัณฑิต
สาขาวิชาฟิสิกส์ประยุกต์
มหาวิทยาลัยเทคโนโลยีสุรนารี
ปีการศึกษา 2564

ADVANCED CHARACTERIZATION OF ULTRA-THIN TETRAHEDRAL
AMORPHOUS CARBON OVERCOATS FOR HIGH AREAL DENSITY MAGNETIC
RECORDING

Suranaree University of Technology has approved this thesis submitted in
partial fulfillment of the requirements for a Degree of Doctor of Philosophy

Thesis Examining Committee



(Assoc. Prof. Dr. Panomsak Meemon)

Chairperson



(Assoc. Prof. Dr. Prayoon Songsiriritthigul)

Member (Thesis Advisor)



(Assoc. Prof. Dr. Saroj Rujirawat)

Member (Thesis Co-Advisor)



(Dr. Narong Chanlek)

Member (Thesis Co-Advisor)



(Prof. Dr. Rattikorn Yimnirun)

Member



(Assoc. Prof. Dr. Prapun Manyum)

Member



(Dr. Wiwat Nuansing)

Member



(Prof. Dr. Santi Maensiri)

Dean of Institute of Science



(Assoc. Prof. Dr. Chatchai Jothityangkoon)

Vice Rector for Academic Affairs
and Quality Assurance

วรินทร์ ชาตะรัตน์ : การวิเคราะห์ชั้นสูงของฟิล์มที่เอ-คาร์บอนชนิดบางมาก สำหรับฮาร์ดดิสก์ที่มีความจุสูง (ADVANCED CHARACTERIZATION OF ULTRA-THIN TETRAHEDRAL AMORPHOUS CARBON OVERCOATS FOR HIGH AREAL DENSITY MAGNETIC RECORDING) อาจารย์ที่ปรึกษา : รองศาสตราจารย์ ดร.ประยูร ส่งสิริฤทธิกุล, 145 หน้า.

คำสำคัญ: การบันทึกด้วยแม่เหล็กช่วยด้วยความร้อน/ คุณสมบัติทางไดรโบลีย์/ อัตราส่วน I_D/I_G

เทคโนโลยีการบันทึกข้อมูลด้วยแม่เหล็กในอนาคต เช่น การบันทึกด้วยแม่เหล็กช่วยด้วยความร้อน (HAMR) จะมีความจุหนาแน่นของพื้นที่สูงขึ้นและความหนาของฟิล์มคาร์บอนที่บางลง ช่วยทำให้ระยะห่างของหัวอ่านแผ่นดิสก์ (HMS) ลดลงเพื่อเพิ่มความจุ ดังนั้นจะทำให้ประสิทธิภาพของฟิล์มคาร์บอนลดลงที่มีความจำเป็นในการปกป้องหัวอ่านและแผ่นดิสก์ ในวิทยานิพนธ์นี้ เติตระฮีดรัลฟิล์มคาร์บอน ($ta-C$) บางเฉียบจำนวนมากสำหรับฮาร์ดดิสก์ไดรฟ์ (HDD) ถูกสังเคราะห์และตรวจสอบในแง่ของคุณสมบัติทางไดรโบลีย์ สภาพแวดล้อม ในการยึดติดทางเคมี และโครงสร้างจุลภาคของคาร์บอน การศึกษานี้แบ่งออกเป็นสองส่วน: (i) โครงสร้างคล้ายเพชรของเติตระฮีดรัลฟิล์มคาร์บอนที่บางเฉียบพึ่งพาความหนาของฟิล์ม สำหรับการบันทึกด้วยสนามแม่เหล็กที่มีความหนาแน่นของพื้นที่สูงและ (ii) อิทธิพลของความหนาของชั้นอินเตอร์เลเยอร์ที่มีต่อโครงสร้างคล้ายเพชรของเติตระฮีดรัลฟิล์มคาร์บอนที่บางเฉียบ เกี่ยวกับ (i) : ชั้นเคลือบบางเฉียบของเติตระฮีดรัลฟิล์มคาร์บอน ถูกประดิษฐ์ขึ้นในช่วงความหนาระหว่าง 0.5 ถึง 5.0 นาโนเมตร บนชั้นซิลิกอนอินเตอร์เลเยอร์ บนพื้นผิวของนิเกิลเฟอร์ไรต์ (NiFe) โดยใช้แบบพัลส์ฟิลเตอร์แคโทดิกอาร์คในสุญญากาศ (PFCVA) เทคนิคโดยความหนาของชั้นเคลือบเติตระฮีดรัลฟิล์มคาร์บอนถูกวัดความหนาของฟิล์ม โดยใช้ กล้องจุลทรรศน์อิเล็กตรอนแบบส่องผ่านความละเอียดสูง (HRTEM) และเอ็กซ์เรย์เรืองแสงกระจายคลื่น (WDXRF) และการวิเคราะห์ชั้นผิวชั้นสูง เช่น AFM XPS NEXAFS และ Raman spectroscopy ระบุลักษณะทางสัณฐานวิทยาของพื้นผิว องค์ประกอบทางเคมี และโครงสร้างของฟิล์ม วิเคราะห์สมบัติทางไดรโบลีย์ด้วยการสีกหรือแบบบอลไปกลับบนแผ่นดิสก์และ ความขรุขระของพื้นผิวของสารเคลือบ ถูกรายงานว่าต่ำกว่า 0.23 นาโนเมตร ชั้นเคลือบของเติตระฮีดรัลฟิล์มคาร์บอน แสดงสัดส่วนพันธะ $sp^3 C$ สูง อย่างไรก็ตาม เนื่องจากความหนาของฟิล์มลดลงมาในระดับ 1.0 นาโนเมตร สัดส่วนของพันธะ sp^2 ขยายตัว เพิ่มสัมประสิทธิ์แรงเสียดทาน (COF) อย่างมีนัยสำคัญ ผลลัพธ์ที่ได้แสดงให้เห็นถึงข้อจำกัดของความหนาของเติตระฮีดรัลฟิล์มคาร์บอน ที่ประดิษฐ์ขึ้นโดยพัลส์ฟิลเตอร์แคโทดิก-อาร์คในสุญญากาศเทคนิคเพื่อเป็นสารเคลือบป้องกันสำหรับอุปกรณ์จัดเก็บแม่เหล็กความหนาแน่นสูง เกี่ยวกับ (ii) : การสปีดเตอร์ที่ใช้ในการเคลือบชั้นอินเตอร์เลเยอร์ชั้นซิลิกอนและซิลิกอนไนไตรด์ที่มีความหนาตั้งแต่ 0.5 ถึง 1.0 นาโนเมตร ตามด้วยเคลือบ 1.0 นาโนเมตร ของเติตระฮีดรัลฟิล์มคาร์บอน ด้วย พัลส์ฟิลเตอร์แคโทดิกอาร์ค

ในสุญญากาศ การทดสอบแบบ Ball-on-disk เปิดเผยว่า ซิลิกอน-คาร์บอน และซิลิกอนไนไตรด์ คาร์บอนจะมีค่าสัมประสิทธิ์แรงเสียดทาน (COF) ที่มีต่ำกว่า ฟิล์มไม่มีอินเตอร์เลเยอร์ จากการวิเคราะห์ XPS เปิดเผยว่าพันธะ Si และ Si-N ถูกแปลงเป็นพันธะ Si-C และ C-N โดยเฉพาะอย่างยิ่ง การเคลื่อนชั้นอินเตอร์เลเยอร์ของซิลิกอนไนไตรด์ ระหว่างชั้น-เตตระฮีดรัลฟิล์มคาร์บอน และนิเกิลเฟอร์ไรต์ (NiFe) ตามหลักฐานพบชั้นประสานที่ก่อตัวขึ้นระหว่างสองชั้นดังกล่าว ทำหน้าที่เป็นชั้นกันป้องกันการอพยพของน้ำและออกซิเจนผ่านมายังเตตระฮีดรัลฟิล์มคาร์บอน จากพื้นผิวของนิเกิลเฟอร์ไรต์ ซึ่งบ่งชี้ว่าเตตระฮีดรัลฟิล์มคาร์บอนแสดงองค์ประกอบออกซิเดชันที่ลดลงซึ่งสนับสนุนให้มีการยึดเกาะ sp^3 C พิจารณาว่าความหนาและความได้เปรียบของ อินเตอร์เลเยอร์ของซิลิกอนไนไตรด์มีส่วนช่วยในการเพิ่มเนื้อหา sp^3 C ได้ดีเพียงใด ซึ่งยืนยันการค้นพบของ Raman เกี่ยวกับอัตราส่วน I_D/I_G ที่ลดลง ตามความหนาของอินเตอร์เลเยอร์เป็นปัจจัยสำคัญในการออกแบบระบบบันทึกแม่เหล็กความหนาแน่นสูงด้วยสถาปัตยกรรมเตตระฮีดรัลฟิล์มคาร์บอนที่เหมาะสม



สาขาวิชาฟิสิกส์
ปีการศึกษา 2564

ลายมือชื่อนักศึกษา วิมล อมร
 ลายมือชื่ออาจารย์ที่ปรึกษา ช. ฐ. อ.
 ลายมือชื่ออาจารย์ที่ปรึกษาร่วม ศ. ฐ. อ.
 ลายมือชื่ออาจารย์ที่ปรึกษาร่วม กมล อ. อ.

WARINTORN CHATARAT : ADVANCED CHARACTERIZATION OF ULTRA-THIN TETRAHEDRAL AMORPHOUS CARBON OVERCOATS FOR HIGH AREAL DENSITY MAGNETIC RECORDING. THESIS ADVISOR : ASSOC. PROF. PRAYOON SONGSIRIRITTHIGUL, PH.D. 145 PP.

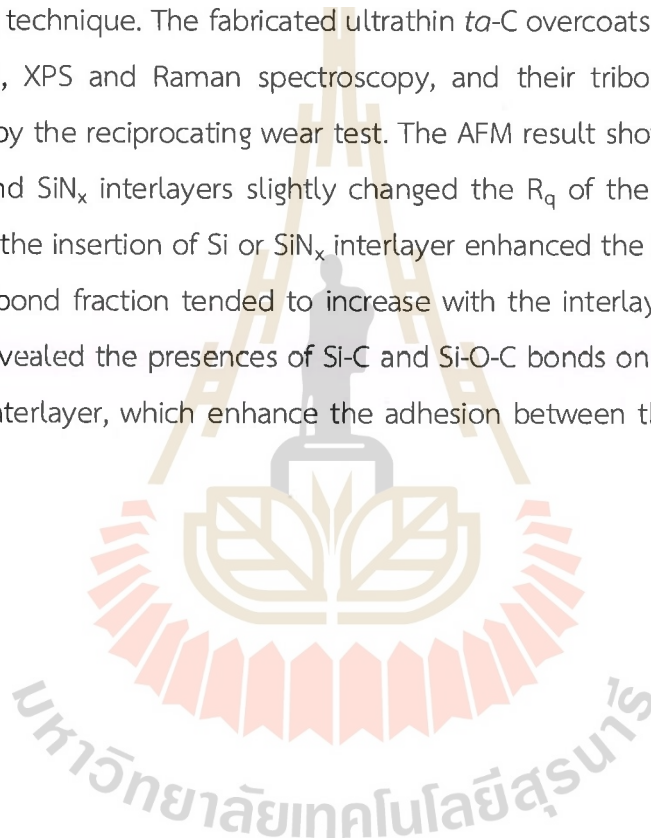
Keyword: heat-assisted magnetic recording/ tribological properties/ I_0/I_G ratio

Tetrahedral amorphous carbon (*ta*-C) films is a class of diamond-like carbon films that contains a high fraction of tetrahedral sp^3 bonded carbon in its structure. It has been commonly used as an overcoat to provide protection against corrosion and mechanical wear for magnetic recording device and hard disk drive (HDD) components, such as, sliders, read/write heads, and media. For this application, it is desirable to reduce the overcoat thickness as thin as possible, down to a few nanometers, in order to increase the density and capacity of magnetic recording devices and HDDs. However, as the thickness reaches the nanometer range, the *ta*-C overcoats may not be able to maintain their chemical bonding structure, especially their high sp^3 bonds fraction, which directly associated with their mechanical properties, such as density, wear, corrosion, thermal stability, and hardness.

This thesis reports on a comprehensive study on chemical structures and tribological properties of ultrathin *ta*-C overcoats with thicknesses of between 0.5 and 5.0 nm for high areal density magnetic recording. The *ta*-C overcoats were fabricated on NiFe substrates using a pulsed filtered cathodic vacuum arc technique. The *ta*-C overcoat thicknesses were accurately determined by high-resolution transmission electron microscopy and wavelength dispersive X-ray fluorescence techniques (WDXRF). The surface morphology, chemical composition, microstructure, and tribological properties were systematically investigated by atomic force microscopy (AFM), X-ray photoelectron spectroscopy (XPS), near-edge X-ray absorption fine structure, Raman spectroscopy techniques, and a reciprocating wear test. The results showed that the surface morphologies of *ta*-C overcoats were atomically smooth with a root mean square surface roughness (R_q) below 0.23 nm. The *ta*-C overcoats had high sp^3 bonds fraction. However, as the overcoat thickness was thinner than 1 nm, the sp^2 bonds fraction suddenly increased resulting in a significant increase in the

coefficient of friction. The obtained results demonstrated the limitation of the thickness of the *ta*-C overcoat fabricated by the PFCVA technique as a protective coating for high-density magnetic storage devices.

In addition, the influence of interlayers on the structure and tribological properties of ultrathin *ta*-C overcoats were investigated. Two different interlayers, Si and SiN_x, with thicknesses of between 0.5 and 5.0 nm were applied to the interface between the substrate and overcoat layer with a thickness of 1 nm. This was achieved by sputtering technique. The fabricated ultrathin *ta*-C overcoats were characterized by WDXRF, AFM, XPS and Raman spectroscopy, and their tribological properties were investigated by the reciprocating wear test. The AFM result showed that the insertion of both Si and SiN_x interlayers slightly changed the R_q of the overcoat. The results showed that the insertion of Si or SiN_x interlayer enhanced the formation of sp³ bond and the sp³ bond fraction tended to increase with the interlayer thickness. The XPS result also revealed the presences of Si-C and Si-O-C bonds on the interfaces of both Si and SiN_x interlayer, which enhance the adhesion between the overcoat layer and substrate.



School of Physics
Academic Year 2021

Student's Signature ปิยนันท์ อมร
 Advisor's Signature อภิสิทธิ์ อ.
 Co-advisor's Signature สงกรานต์
 Co-advisor's Signature พญานันท์

ACKNOWLEDGEMENT

I would like to express my heartfelt appreciation and gratitude to several people who help me, directly or indirectly, during my Ph.D. journey of research and learning at Suranaree University of Technology (SUT), Thailand.

First and foremost, I would like to thank my graduate advisors and mentors at SUT, Assoc. Prof. Dr. Prayoon Songsiriritthigul, Assoc. Prof. Dr. Saroj Rujirawat, and Assoc. Prof. Dr. Panomsak Meemon, Assoc. Prof. Dr. Prapan Manyum and Dr. Wiwat Nuansing for their guidance, encouragement, and support throughout my Ph.D. I also would like to thank Prof. Dr. Rattikorn Yimnirun Vidyasirimedhi Institute of Science and Technology (VISTEC) for his guidance, help and provision of some of the instruments and resources used in this thesis.

I really appreciate Dr. Narong Chanlek not only for his insightful comments, helpful discussions, and valuable suggestions, but also for his challenging questions, which motivated me to broaden my research to include a variety of perspectives and encourage me to broaden my research as well. Additionally, I would like to thank the BL5.3 staff at the Synchrotron Light Research Institute (SLRI), Thailand, for all of their assistance.

Dr. Chanan Euaruksakul, Dr. Hideki Nakajima, and Dr. Natthaphong Konkhunthot owe me a debt of gratitude for their thorough instruction and patience in transferring their expertise and research abilities in NEXAFS characterization, which have been invaluable to my work. I cannot thank them enough for their time spent with me ensuring that I received all necessary training. I would like to express my gratitude to the entire crew of the BL3.2U PES/PEEM at the Synchrotron Light Research Institute (SLRI) in Thailand. I also would like to thank Dr. Somlak Ittisanronnachai, VISTEC, for her help and provision of some of the instruments and resources used in this thesis.

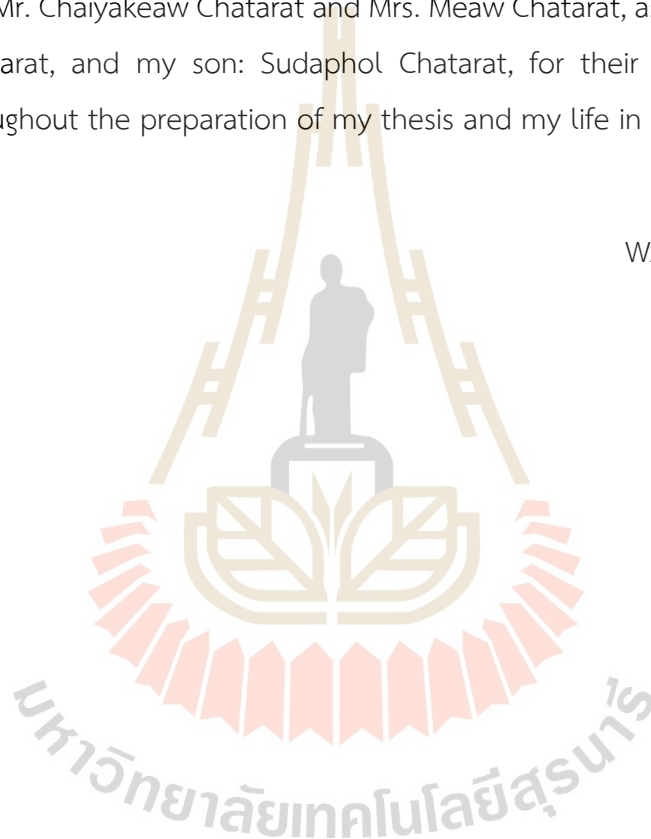
I am so grateful to Mr. Jesada Rasamiputi, a former senior director of slider engineering at Seagate Technology, with whom I worked for many years (Thailand). You have always shown a high level of respect in your leadership. I am proud fact

that I learned this quality from you makes, and I am grateful for your encouragement and faith in me, which is my greatest motivation.

The author is profoundly grateful to the external grants and scholarships for graduate student (contact no. 74/2559), Seagate Technology (Thailand) Co., Ltd. (Korat), and Research Network NANOTEC SLRI for financial support over the year of my doctoral program.

Finally, I really would like to convey my most profound appreciation to my great family: Mr. Chaiyakeaw Chatarat and Mrs. Meaw Chatarat, as well as my wife, Mrs. Kannika Chatarat, and my son: Sudaphol Chatarat, for their continuous love and support throughout the preparation of my thesis and my life in general.

WARINTORN CHATARAT



CONTENTS

	Page
ABSTRACT IN THAI.....	I
ABSTRACT IN ENGLISH.....	III
ACKNOWLEDGEMENT.....	V
CONTENTS.....	VII
LIST OF TABLES.....	X
LIST OF FIGURES.....	XI
LIST OF ABBREVIATIONS.....	XVIII
CHAPTER	
I INTRODUCTION.....	1
1.1 Background and motivation.....	1
1.2 The research objective of this thesis.....	5
II LITERATURE REVIEW.....	7
2.1 Carbon material and electronic configuration.....	7
2.2 Diamond-like carbon film (DLC).....	9
2.3 Classification of diamond-like carbon films.....	12
2.3.1 Hydrogenated amorphous carbon.....	12
2.3.2 Hydrogen-Free diamond-like carbon.....	14
2.3.3 Nitrogenated amorphous carbon films.....	15
2.3.4 Alloyed amorphous carbon films.....	15
2.4 Ultrathin DLC overcoats.....	16
2.5 Deposition Mechanism of sp^3 bond formation of DLC.....	18
2.6 DLC Fabrication Techniques.....	20
2.6.1 Ion beam deposition.....	21
2.6.2 Plasma enhanced chemical vapor deposition.....	21

CONTENTS (Continued)

	Page
2.6.3 Filtered Cathodic Vacuum Arc.....	23
2.7 Influence of deposition conditions on a <i>ta</i> -C structure.....	24
2.7.1 Incident carbon ion energy.....	25
2.7.2 Incident energetic carbon ion angle.....	29
2.7.3 Substrate temperature and deposition rate.....	31
2.7.4 Substrate morphology.....	35
2.8 Ultrathin of DLC Films.....	36
2.8.1 Applications of interlayer or adhesive layer.....	36
2.8.2 Influence of the Environment on DLC Film Tribology.....	39
2.8.3 Physical and mechanical interactions.....	43
2.9 Application of DLC.....	44
2.9.1 Magnetic recording industry.....	44
2.9.2 Automotive parts.....	46
III EXPERIMENTAL PROCEDURE.....	48
3.1 Sample preparation and procedure experiments.....	48
3.1.1 Materials.....	48
3.1.2 Experiment Procedures.....	48
3.2 Fabrications of ultrathin <i>ta</i> -C films.....	51
3.2.1 Deposition setup.....	51
3.2.2 Deposition process.....	53
3.3 Characterization techniques.....	55
3.3.1 High-Resolution Transmission Electron Microscopy (HRTEM).....	55
3.3.2 X-Ray Fluorescence spectrometry (XRF).....	55
3.3.3 X-ray Photoelectron Spectroscopy (XPS).....	58
3.3.4 Near Edge X-ray Absorption Fine Structure spectroscopy.....	59

CONTENTS (Continued)

	Page
3.3.5 Raman spectroscopy.....	65
3.3.6 Atomic force microscopy (AFM).....	68
3.3.7 Tribological Properties characterization.....	69
IV RESULTS AND DISCUSSION.....	71
PART I - Structural dependence on thickness of ultra-thin	
<i>ta</i>-C overcoats.....	71
4.1 Overcoat thickness and surface morphology.....	71
4.2 Chemical composition and structure.....	74
4.3 Tribological performances.....	84
4.4 Discussion.....	85
PART II- Influence of an interlayer on ultrathin	
<i>ta</i>-C overcoats.....	90
4.5 Influence of interlayers on surface morphology.....	90
4.6 Tribological properties.....	93
4.7 Raman analysis.....	95
4.8 Chemical and interfacial bonding analysis.....	98
V CONCLUSIONS AND SUGGESTIONS FOR FUTURE WORK.....	104
REFERENCES.....	107
APPENDIX.....	131
CURRICULUM VITAE.....	145

LIST OF TABLES

Table	Page
2.1 Comparison of characteristic properties of amorphous carbon with diamond, graphite, C60, and polyethylene (Robertson, 2002).....	12
2.2 The Coefficient of friction values and the wear rate of the hydrogen-free DLC coating testing different environment (Donnet et al., 2007).....	41
4.1 Thicknesses of the fabricated <i>ta</i> -C overcoats derived from WDXRF spectra and cross-sectional HRTEM images.....	73
4.2 Relative atomic percentage of carbon bond estimated from C1s peak.....	78
4.3 Thickness of interlayer and tetrahedral amorphous carbon.....	91
4.4 Chemical bonding and binding energies of the C bonding configurations for composite Si <i>ta</i> -C and SiN _x / <i>ta</i> -C films.....	100
4.5 Binding energies (B.E) and associated atomic percentage in the Si and SiN _x interlayer XPS Si2p spectra.....	101

LIST OF FIGURES

Figure	Page
1.1 Industry Road map magnetic recording technology development by the Advanced Storage Industry Consortium (ASTC) (ASTC, 2014).....	2
1.2 Hard disk media structures. (a) Schematic illustrating the cross-section of a hard disk drive's head media spacing (Dwivedi et al., 2021). (b) Based on the projections of the HMS for area densities of 1, 4, and 10 Tb/in ² . The HMS trend is projected by linearly extrapolating the HMS trend (Yeo, 2015).....	3
2.1 Schematic represent electron density of carbon valence electrons in the s and P _z , P _x , and P _y state of free carbon atoms. Modified from (PIERSON, 1993).....	8
2.2 The scheme of hybridizations of carbon during bonding. Adapted from (Robertson, 2002).....	9
2.3 Various allotropes of carbon material. (a) Hexagonal crystalline graphite, (b) cubic diamond, (c) C ₆₀ fullerene, (d) carbon nanotube, and (e) graphene (Scarselli et al., 2012).....	10
2.4 Amorphous carbon bonding distributions at 1.5 g/cm ³ , 2 g/cm ³ , 2.5 g/cm ³ , 3 g/ g/cm ³ , and 3.5 g/ g/cm ³ density are depicted in the graphic. The C atom that is sp/sp ² /sp ³ -bonded is represented by the colors yellow, green, and blue, respectively. Reprinted with permission (Liu et al., 2019).....	11
2.5 Amorphous carbon's ternary phase diagram, the three corners represent diamond, graphite, and hydrocarbons (Casiraghi et al., 2007).....	13

LIST OF FIGURES (Continued)

Figure	Page
2.6 The subplantation model developed by Lifshitz et al. (Lifshitz et al., 1990): energetic carbon species penetrate the developing carbon film's surface, and preferentially displace sp ² -bonded carbon atoms, resulting to. to the increase of film's density and sp ³ bond content. Reprinted (Robertson, 2002; Sánchez-López et al., 2008).....	19
2.7 Flow diagram illustrating the fraction of incoming ions that contribute to film densification, interstitial trapping, and surface relaxation. Reprinted (Robertson, 2002).....	20
2.8 Schematic diagram of an IBD system (Zhou and Wadley, 2000).....	22
2.9 Schematic diagram of plasma-enhanced chemical vapor system, reprint (WIKI).....	22
2.10 Photograph of FCVA deposition system with an S-bend macroparticle filter with two 90° bends. Bright streaks are macroparticles that are being filtered out of the plasma (Anders et al., 2001).....	24
2.11 Coordination configurations of films under different incident energies, where colors represent the different coordination numbers (Li et al., 2013).....	26
2.12 Dependence of (a) density, stress, and (b) sp ³ bond fraction on incident energies (Li et al., 2013).....	28
2.13 The interdependency of the sp ² fraction and the surface roughness on ion energy up to 20 keV. Reprinted (Grossman et al., 1996).....	29
2.14 Dependence of (a) total thickness of ta-C films and (b) thickness of intermixing layer obtained from T-DYN simulations. C ⁺ ion influence is in the range of (0.9-9.0) ×10 ¹⁶ ions/cm ² (Wang and Komvopoulos, 2012).....	30

LIST OF FIGURES (Continued)

Figure	Page
2.15	XPS C1s spectra peak of a graphite sample and the DLC films obtained at various deposition angles.....31
2.16	The relationships between the surface roughness and density of 1000 Å carbon films deposited using MSIBD with 120 eV ions and deposition temperature (Lifshitz et al., 1995).....32
2.17	The evolution of Raman spectra of the carbon film deposited at (a) room temperature, (b) 400°C, and (c) 800°C.....33
2.18	The relationship between the sp ³ bond content of DLC films and deposition temperature for deposition by high current pulsed vacuum arc discharges (ion energy ≈ 50 eV) with high instantaneous growth rates during the pulse (Gago et al., 2005; Koskinen et al., 1998; Schultrich, 2018).....34
2.19	Dependence of sp ³ fraction and density on the substrate temperature for DLC films deposited by DC vacuum arc discharge with MSIB at the growth rate of 2 nm/s (Chhowalla et al., 1997).....34
2.20	Proposed growth mechanism for a DLC film on a rough silicon substrate (a) Si substrate, (b) initial smoothing stage: island nucleation generated by the favored growth of valley, (c) roughening stage: island expansion, and (d) ultimate smoothing stage: island coalescence. Reprint (Zhong et al., 2008).....36
2.21	Variation of G position, ID/IG, and G intensity with the Si seed layer thickness varying from 0 to 30 Å. Reprinted (Liu et al., 2013).....38
2.22	The friction coefficient of the DLC films with various SiN _x interlayer Thicknesses. In the measurement, the tip was translated with a consistent load allow the penetration into the film.....38

LIST OF FIGURES (Continued)

Figure	Page
2.23 The influence of relative humidity on the coefficient of friction of hydrogen-free, hydrogenated, and DLC films with varied hydrogen concentrations. Reprinted (Ronkainen and Holmberg, 2008).....	39
2.24 Surface roughness influences initial and steady-state DLC film friction coefficients. Reprinted from (Erdemir et al., 2006).....	44
2.25 The relationship between the dispersion of the G peak and the scratch resistance of an a-C: N film is grown using magnetron sputtering and FCVA (Vetter, 2014).....	46
2.26 Selected engine parts coated by diamond-like carbon (DLC) (Vetter, 2014).....	47
3.1 DLC film deposition and characterization experiment methodology flow chart.....	49
3.2 DLC film deposition and characterization experiment methodology flow chart.....	50
3.3 Illustrates the Pulse filtered cathodic vacuum arc (PFCVA) deposition system (Veeco Instruments Inc, 2012).....	52
3.4 PFCVA chamber and cathodic arc source, (a) Assembly cathodic arc source, (b) schematic diagram of PFCVA chamber and cathodic arc source.....	53
3.5 Schematic diagram of the PFCVA deposited of ultrathin DLC layer with adhesion layer on the NiFe.....	54
3.6 Schematic illustration of XRF spectrometry system: Comparison Between (a). Energy Dispersive type (EDXRF) and (b). Wavelength Dispersive Type (WDXRF) analysis of the standard synthetic system elements. Reprinted (Brouwer, 2006).....	57

LIST OF FIGURES (Continued)

Figure	Page
3.7	Infographic illustration the basic principle of the XPS technique.....59
3.8	Schematic diagram of an X-ray absorption spectrum for the NEXAFS (XANES) and the EXAFS regions (Oguz Er et al., 2012; Stöhr, 2013).....60
3.9	Schematic diagram of NEXAFS measurement in electrons yield (total, partial, and Auger) modes and transmission modes modified from Stöhr (1992); Hähner (2006); Watt et.al.....62
3.10	The schematic illustrates the absorption of an X-ray photon with the excitation of a core electron to an unoccupied molecular orbital. Reprinted (Dienwiebel et al., 2018).....64
3.11	(a) Incident light interacts with a vibrating molecule. (b) Jablonski diagram representing Quantum Energy transitions for Rayleigh and raman scattering. Reprinted (Chu and Li, 2006; Ferrari and Robertson, 2000; Ismail and Ismail, 2015).....67
3.12	Vibration modes in graphitic carbon illustrated the stretching mode for (a) chain configuration, (b) ring configuration and the breathing mode for (c) a ring configuration. Result in (a) and (b) leads to the G peak, and (c) leads to the D peak in the Raman spectrum (Ferrari and Robertson, 2000; Ong et al., 2007).....67
3.13	Schematic illustration of the principle of AFM. Reprinted (Garcia et al., 2002).....68
3.14	Tribometer (UMT-2 Bruker) graphic. Normal load (N) is applied while the surface of the steel ball slides on the DLC film (Vieira et al., 2020).....70
4.1	Cross-section HRTEM images of the fabricated <i>ta</i> -C films with Si Interlayers on NiFe substrates. The <i>ta</i> -C film thickness was varied between 0.5-5.0 nm.....72

LIST OF FIGURES (Continued)

Figure	Page
4.2 High-resolution XPS spectra of (a) C1s and (b) Si2p peaks of <i>ta</i> -C films with thicknesses of 0.5-5.0 nm.....	75
4.3 High resolution XPS spectra of (a) Fe2p and (b) Ni2p peaks of the fabricated <i>ta</i> -C films with thicknesses of 0.5-5.0 nm.....	76
4.4 Carbon (C) K-edge NEXAFS spectra of HOPG and ultrathin <i>ta</i> -C overcoats deposited by PFCVA technique presenting the evolution of the C1s $\rightarrow \pi^*$ and C1s $\rightarrow \sigma^*$ transitions with <i>ta</i> -C overcoat thickness.....	80
4.5 (a) The π^* resonance intensity and (b) the sp^2 fraction and C-H content were deduced from the NEXAFS spectra as a function of film thickness.....	81
4.6 Normalized Raman spectra excited by a laser wavelength of 532 nm in the range of 800-2200 cm^{-1} of the fabricated ultrathin <i>ta</i> -C overcoats.....	82
4.7 I_D/I_G ratio and size of sp^2 clusters dependent on the thickness of <i>ta</i> -C films, deposited by pulsed filtered cathodic vacuum arc.....	83
4.8 (a) Plots between $sp^3/(sp^2+sp^3)$ ratio estimated from XPS spectra and I_D/I_G ratio as a function of the <i>ta</i> -C overcoat thickness. (b) The correlation of $sp^3/(sp^2+sp^3)$ ratio and I_D/I_G ratio of <i>ta</i> -C overcoats.....	83
4.9 (a) Friction curves and (b) COF of the cleaned NiFe, Si-interlayer deposited, and fabricated <i>ta</i> -C overcoat with thicknesses of 0.5-5.0 nm.....	88
4.10 Optical images of a NiFe substrate, a Si interlayer, and <i>ta</i> -C overcoats with thicknesses of 0.5-5.0 nm after slide reciprocating tribological test.....	89
4.11 Plot of R_q , I_D/I_G ratio, sp^2 fraction estimated from NEXAFS, and COF as a function of <i>ta</i> -C overcoat thickness.....	90

LIST OF FIGURES (Continued)

Figure	Page
4.12 Average root means square surface roughness (R_q) of the NiFe substrate, the interlayer (a) 0.5-1.0 nm of Si and SiN_x interlayer without <i>ta</i> -C overcoat. (b) Varying 0.5-1.0 nm of Si and SiN_x interlayer with 1 nm <i>ta</i> -C overcoat.....	92
4.13 AFM images 3D scan size $1 \times 1 \mu\text{m}$ area of cleaned NiFe substrate, 1 nm monolithic <i>ta</i> -C film (C10), 1 nm monolithic Si and SiN_x interlayer (10Si,10SiN _x), and composited layer 10SiC10 and 10SiN _x C10.....	93
4.14 Dependence COF and interlayer thickness of Si and SiN_x with respect to number of cycles as obtained from ball-on-disk tribological tests.....	94
4.15 Raman spectra of DLC films with different interlayer thickness 0.0-1.0 nm of (a) Si and (b) SiN_x amorphous interlayer with 1 nm <i>ta</i> -C overcoat film, with the D and G peak.....	96
4.16 Variation of the I_d/I_g ratio and the G position as a function of the Thickness of the Si and SiN_x interlayer varying from 0 to 1 nm.....	97
4.17 High resolution C1s core level XPS spectra of as-deposited samples (a) C10, (b) 10SiC10, and (c) 10SiN _x C10.....	99
4.18 Relationship of $\text{sp}^3\text{C}/(\text{sp}^3\text{C}+\text{sp}^2\text{C})$ fraction deconvoluted of C1s core level spectra of Si and SiN_x interlayer thickness overcoat with <i>ta</i> -C film.....	100
4.19 Deconvolution of Si2p XPS spectra with Gaussian-Lorentzian of Si and SiN_x interlayer (a) 10SiC10 and (b) 10SiN _x C10 with 1.0 nm <i>ta</i> -C overcoat.....	103

LIST OF ABBREVIATIONS

°C	Degrees Celsius
~	Approximately
µm	Micrometer
Å	Angstrom
a.u.	Arbitrary unit
a-C	Amorphous carbon
a-C: H	Hydrogenated amorphous carbon
a-C: N	Nitrogenated amorphous carbon
AES	Auger Electron Spectroscopy
AFM	Atomic Force Microscopy
AMR	Anisotropic Magneto Resistive
ARXPS	Angle resolved c-ray photo electron spectroscopy
B.E	Binding Energy
BPI	Bit Per Inch
BPM	Bit Patterned Media
BPMR	Bit Patterned Media Recording
C60	Buckminsterfullerene
CAGR	Component Annual Growth Rate
C K-edge	Carbon K-shell electrons
COC	Carbon overcoat
COF	Coefficient of friction
Cr	Chromium
CVD	Chemical vapor deposition
DAQ	Data acquisition card
DC	Direct current
DLC	Diamond Like Carbon
eV	Electron Volt
ECWR	Electron cyclotron wave resonance

LIST OF ABBREVIATIONS (Continued)

EDXRF	Energy Dispersive X-Ray Fluorescence
EELS	Electron energy loss spectroscopy
ESCA	Electron Spectroscopy for Chemical Analysis
FCVA	Filtered Cathodic Vacuum Arc
Fe	Iron
g/cm ³	Grams Per Cubic Centimeter, Density unit
GB	Gigabytes
GMR	Giant magneto resistive
HAMR	Heat-Assisted Magnetic Recording
HCA	Head cleaning agent
HDD	Hard disk drive
HDI	Head disk interface
HiPIMS	High-power impulse magnetron sputtering
HMS	Head Media Spacing
HOPG	Highly Oriented Pyrolytic Graphite
HRTEM	High Resolution Transmission Electron Microscopy
IBD	Ion beam deposition
ICP	Inductively coupled plasma
I _D /I _G	D peak to G peak Intensity Ratio
in	inches
INSIC	Information storage industry consortium
IPA	Isopropyl alcohol
IP	Ionization potential
K	Kelvin of temperature unit.
km	Kilometer
MAMR	Microwave-Assisted Magnetic Recording
ME	Metal evaporated
MEMS	Micro-electro-mechanical systems
mN	Millinewtons

LIST OF ABBREVIATIONS (Continued)

Mo	Molybdenum
MP	Metal particle
MPa	Mega Pascal
MR	Magneto resistive
mTorr	Milli Torr
MSD	Magnetron sputtering deposition
MSIBD	Mass-selected ion beam deposition
NEXAFS	Near Edge X-Ray Absorption Fine Structure
Ni	Nickel
NiFe	Nickel Iron Permalloy
nm	Nanometer
nm/s	Growth Rate Nanometer Per Second
O	Oxygen
PECVD	Plasma enhanced chemical vapor deposition
PFCVA	Pulsed Filtered Cathodic Vacuum Arc
PFPE	Perfluoropolyether
PLD	Pulsed laser deposition
PVD	Physical vapor deposition
RBS	Rutherford backscattering spectrometry
RF	Radio frequency
RH	Relative humidity
Rq	Root-mean-square roughness
sccm	Standard Cubic Centimeters per Minute
SEM	Scanning electron microscopy
Si	Silicon
SiC	Silicon Carbide
Si ₃ N ₄	Silicon Nitride
SiN _x	Amorphous Silicon Nitride
SiN _x C	Amorphous Silicon Nitride Carbide

LIST OF ABBREVIATIONS (Continued)

SNR	Signal to noise ratio
sp	Linear hybridization
sp ²	Trigonal planar hybridization
sp ² C	sp ² -Hybridized Carbon
sp ³	Tetrahedral hybridization
sp ³ C	sp ³ -Hybridized Carbon
SPM	Scanning probe microscopy
ta-C	Tetrahedral Amorphous Carbon
ta-C: H	Tetrahedral hydrogenated amorphous carbon
ta-C: N	Nitrogenated tetrahedral amorphous carbon
Tbit/in ²	Terabit Per Square Inch
TDMR	Two-Dimensional Magnetic Recording
TEM	Transmission Electron Microscopy
TEY	Total Electron Yield
TFY	Total Fluorescence Yield
Ti	Titanium
TPI	Track per inch
TRIM	Transport of ions in matter
VAD	Vacuum arc deposition
VCR	Video cassette recorder
W	Tungsten
WDXRF	Wavelength Dispersive X-Ray Fluorescence
XANES	X-Ray Absorption Near Edge Structure
XPS	X-Ray Photoelectron Spectroscopy
ZB	Zettabytes

CHAPTER I

INTRODUCTION

1.1 Background and motivation

The data-driven world has grown, prompting the formation of a global datasphere, which is expected to rise from 33 Zettabytes (ZB, 1 ZB = trillion gigabytes (GB)) in 2018 to 175 Zettabytes (ZB) by 2025 (Rydning, 2018). Emerging innovation will be required to offer higher area density storage and low-cost information storage technology. Hard disk drives (HDD) will continue to be the dominant data storage devices. Worldwide HDD industry shipments are projected to expand a compound annual growth rate (CAGR) of 18.5% over the 2020 - 2025 forecast period, and the average capacity per drive is forecast to increase at a five-year CAGR of 25.5% ((IDC), 2021). The HDD industry is working towards finding solutions to propose several magnetic recording technologies for future HDDs in their roadmap to increase their area density to greater than 1 Tb/in². Future magnetic recording technologies have introduced heat-assisted magnetic recording (HAMR) (Kief and Victora, 2018; Matlak and Komvopoulos, 2018; Seigler et al., 2013), microwave-assisted magnetic recording (MAMR) (Schabes, 2008), bit patterned media recording (BPMR) (Albrecht et al., 2015; Wood et al., 2009), and two-dimensional magnetic recording (TDMR) (Wood et al., 2009). Between all these potential magnetic recording technology solutions, the industry roadmap focuses on the following prominent and appealing technologies, HAMR and BPM, as well as a combination of the two, which are considered as the next generation high-density hard disk drives. These technologies can reach an areal density of up to 10 Tb/in² as illustrated in Figure 1.1., the introduction to HAMR and BPM technology ((ASTC). 2014).

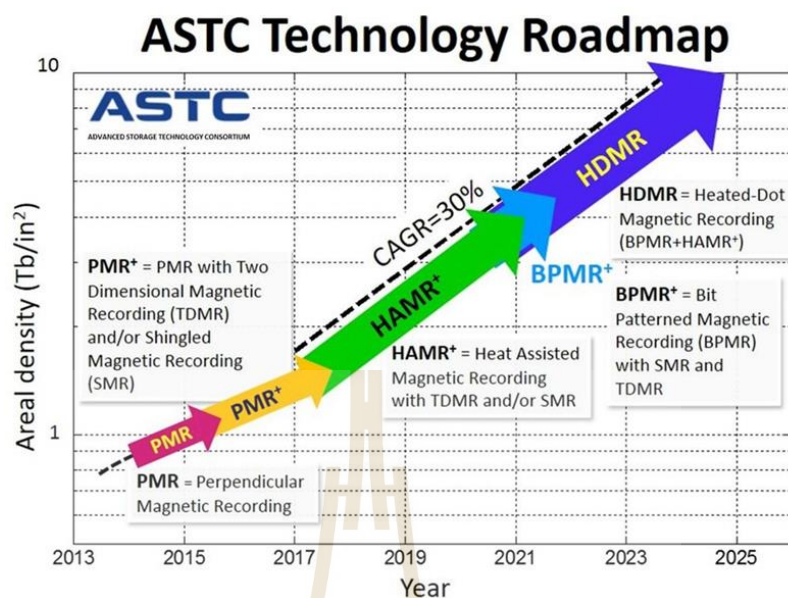


Figure 1.1 Industry Road map for magnetic recording technology development by the Advanced Storage Industry Consortium (ASTC) (ASTC, 2014).

Head-media spacing (HMS) is a vertical distance between the read-write elements of the head and the magnetic disk in magnetic storage. HMS is composed of the flying height of the head, the thickness of the carbon overcoat and lubricant, as well as the surface roughness of the head and media, as shown in Figure 1.2(a). Achieve areal density beyond 1Tb/in² can be attained with HMS reduction of less than 7 nm, as shown in Figure 1.2(b). As a result, the disk carbon overcoat and head carbon overcoat films must be reduced in thickness by 1-3 nm and 1-2 nm, respectively (C. Casiraghi et al., 2004; Marchon et al., 2013). Therefore, the high areal density of the next generation aims to reduce the carbon overcoat film thickness and preserve the mechanical and chemical properties. The various challenges of lowering the head overcoat thickness to ≤ 2 nm for beyond 1 Tb/in² areal densities.

The carbon overcoat, also known as Diamond-like carbon (DLC) film, is critical for preventing damage to the head, transducer, and magnetic recording media disks. DLC possesses many outstanding properties, including high hardness, chemical inertness, smoothness, and low friction coefficient (Casiraghi et al., 2005; Robertson, 2003), suitable for good surface overcoat protection.

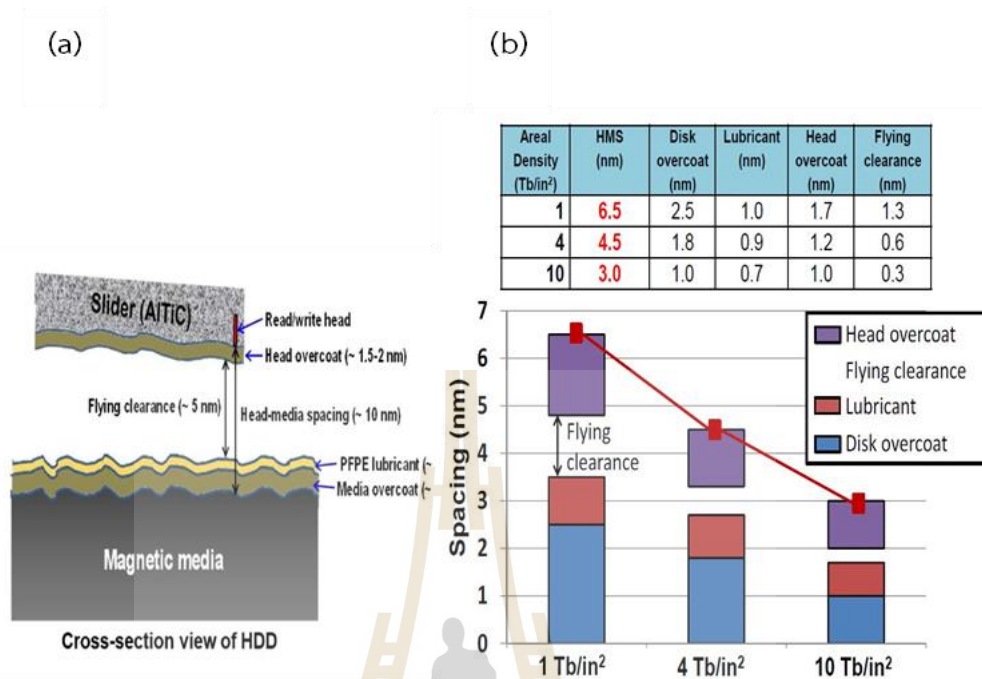


Figure 1.2 (a) Schematic illustrating the cross-section of a hard disk drive's head media spacing (Dwivedi et al., 2021). (b) Based on the projections of the HMS for area densities of 1, 4, and 10 Tb/in². The HMS trend is projected by linearly extrapolating the HMS trend (Yeo, 2015).

Most DLC film deposition techniques, including sputtering and plasma-enhanced chemical vapor deposition (PECVD) methods, are incapable of depositing continuous formation of a film with less than 5.0 nm thickness (Matlak and Komvopoulos, 2018; Robertson, 2001). In this context, the filtered cathodic vacuum arc (FCVA) deposition method is promising for the continuous formation of ultrathin tetrahedral amorphous carbon (*ta*-C) films combined with outstanding mechanical and tribological properties, such as smoothness, high hardness, wear resistance, and high thermal stability, due to the presence of a highly significant tetrahedral sp^3 bonded carbon (Casiraghi et al., 2004; Goohpattader et al., 2015; Yamamoto et al., 2003). Previous studies on the characteristics of *ta*-C films synthesized using the FCVA method found a substantial relationship with the incidence of ion energy in the 50-200 eV region. All other deposition conditions remained constant. The optimal ion energy range of 75-85 eV was determined via electron energy loss spectroscopy (EELS), corresponding to a maximum sp^3 content of 87.5% (Fallon et al., 1993; Xu et al., 1996).

The mechanical integrity of *ta*-C films depends on trigonal (sp^2) and sp^3 carbon bond hybridization fractions. The high C^+ ion energy can penetrate directly beneath the treated surface and cause strain weakening, which significantly increases the density of the carbon film by promoting more increased sp^3 C bonding within the growing *ta*-C film resulting from subplantation (Ferrari et al., 2000; Lifshitz et al., 1989; Robertson, 2001). Additionally, BPMR and HAMR have proposed the next-generation technology that uses laser heating above $\sim 227^\circ\text{C}$ during the writing process, whereas the *ta*-C deposited via the FCVA method has much better thermal stability and prevents rapid structural destabilization (Albrecht et al., 2015; Matlak et al., 2018; Wang and Komvopoulos, 2011). These essential and desired properties of FCVA-deposited carbon have motivated researchers to consider FCVA as a possible method to produce ultrathin carbon overcoats for head and media.

Recently, high areal density requires film thickness reduction to develop continuously. This film structure is that the ratio of sp^3 to sp^2 carbon hybridization states and the relative amount of sp^3 in *ta*-C films affect the tribological properties such as friction durability, wear behavior, and surface morphology, despite being grown under the same conditions (Casiraghi et al., 2004; Liu and Wang, 2009; Polaki et al., 2016). Casiraghi et al (Casiraghi et al., 2005) and Moseler et al. (Moseler et al., 2005) found that the ultra-smooth DLC films can be employed as an ultra-thin protective film for the high areal density of HDD. The effect of the substrate prior to film deposition has been reported by Zhong et al. (Zhong et al., 2008). As a result, the evolution of the surface morphology on an atomic scale depends on the initial surface morphology of the silicon substrate.

Numerous challenges arise in research over whether ultrathin DLC films of 1-2 nm thickness can still provide protection film for next-generation magnetic storage or high-density hard disk drives:

- i. Effect thickness on the structure of ultra-thin diamond-like carbon film.
- ii. Consistent film formation and defects in the carbon overcoat allow moisture and metallic ions from the surface substrate to penetrate through the carbon overcoat,

resulting in enhanced corrosion and oxidation of the write-reader head or media (Novotny and Staud, 1988; Tomcik et al., 2000).

iii. Regarding wearing protection, a thinner DLC layer reduces the bulk volume of the DLC, decreasing the DLC's capability to provide adequate mechanical protection.

iv. Furthermore, as the coverage of the DLC layer is reduced, the roughness of the DLC layer increases.

v. The influence of substrate surface roughness on tribology performance is investigated.

However, no direct investigation analyzes and comprehends the influence of ultrathin *ta*-C films generated on NiFe substrates using FCVA on their structure, surface morphology, and tribological properties.

1.2 The research objective of this thesis

This research primarily aims to characterize the chemical structure and tribological properties of the *ta*-C films fabricated by using PFCVA technique. The secondary goal is to understand the correlation between the microstructure tribological characteristics and thickness of diamond-like carbon coatings, in order to optimize and design new generation DLC overcoats for high-density magnetic recording. The objectives of the present research are itemized as follows:

i. Fabricate the ultrathin DLC films with thicknesses of 0.5-5.0 nm by using FCVA technique.

ii. To characterize and investigated the micro- and chemical structure explore the growth mechanism on various thicknesses, in particular, sp^3 and sp^2 bonds, of the ultrathin DLC films by using advanced and synchrotron radiation-based characterization techniques.

iii. To investigate the correlation between microstructure, tribological characteristics, and thickness of the ultrathin DLC films.

iv. To explore the effect of the Si and SiN_x adhesion layers the ultra-thin DLC film properties.

The understanding of the chemical and tribology characteristics of the ultrathin *ta*-C coatings would, allow the design and optimization of the overcoat layer for HDD applications. This could be accomplished through in-depth analyses of the ultrathin *ta*-C film by using several advanced characterization techniques. The film thickness was accurately determined by a wavelength dispersive X-ray fluorescence (WDXRF) technique. The cross-sectional film structure was examined by high-resolution transmission electron microscopy (HRTEM). The surface morphology was analyzed by atomic force microscopy (AFM). The electronic structure was investigated by near-edge X-ray absorption fine structure (NEXAFS) and X-ray photoelectron spectroscopy (XPS) which are extremely sensitive to the coordination of carbon configuration. The disordered structure was also determined by Raman spectroscopy technique. The tribological properties specifically the coefficient of friction was examined by a reciprocating wear test method.

CHAPTER II

LITERATURE REVIEW

This chapter includes in-depth information of the fundamental properties, fabrication techniques and novel characterization techniques for diamond-like carbon (DLC) films. Previous publications containing information on carbon structure and bonding, DLC film properties, deposition techniques, ultra-thin film characterization approach, and application in hard disk drives, are reviewed. The challenges relevant to the current research being conducted are also addressed in the review. The material presented in this chapter is used as a guideline in the current investigation.

2.1 Carbon material and electronic configuration

Carbon an interesting element that appears in a diverse array of allotropic forms, such as diamond or graphite. Carbon materials exhibit many extraordinary properties and offer tremendous potential for modern science and technology. The electrical structure of an element, particularly its outer electrons, or valence electrons, determines the properties of the element and its compounds. Carbon's angular momentum is conserved in a spherically symmetric potential. Thus, states are defined by the primary quantum number $n=1, 2$ (corresponding to the lowest energy shells) and the angular momentum values s (for $n= 1, 2$), which has two states corresponding to both spin directions, and p (for $n= 2$), which has six states corresponding to the three possible orientations P_x, P_y and P_z each with two spins. The ground state of a carbon atom with two core electrons in the first shell and four valence electrons are $1s^2 2s^2 2p^2$; the super script labels the number of electrons in the corresponding state. Figure 2.1 depicts the two symmetric lobes representing the electron distribution in the s and p states, respectively (Schultrich, 2018).

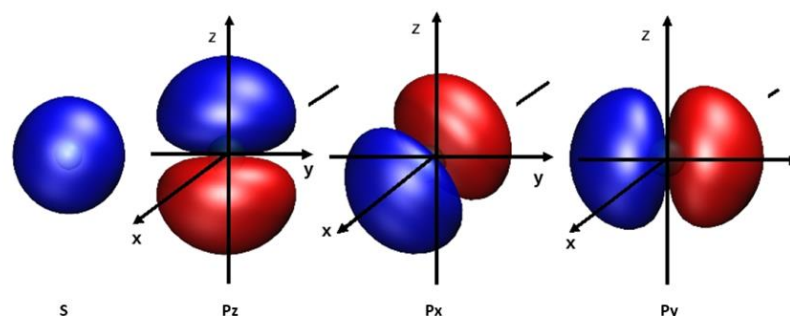


Figure 2.1 Schematic represent electron density of carbon valence electrons in the s and P_x , P_y , and P_z state of free carbon atoms. Modified from (PIERSON, 1993).

The bonding response between atoms is the most efficient, resulting in vital, directed binds (σ bonds). Another weaker influence (π bonds) arises from the overlap of sideways oriented orbitals on each other's orbitals. A considerable amount of energy is gained from the optimized interactions with surrounding atoms. This energy gains more than compensates for the cost of hybridization, resulting in the formation of energetic carbon atom bonds.

As illustrated in Figure 2.2, the combination of orbitals can hybridize, causing the orbital energy to be transferred into hybridized orbitals (Robertson, 2002). The sp^1 bonding is formed by forming two bonds (due to the hybridization of one $2s$ and one $2p$ electron) and two bonds. In comparison, the sp^2 bonding is formed by forming three bonds (due to the hybridization of one $2s$ and two $2p$ electron) and one bond (due to the remaining $2p$ electron). The sp^3 bonding is formed by forming four bonds (due to the hybrid (due to the hybridization of one $2s$ and the three $2p$ electrons). Carbon can form bonds with itself in any of the configurations listed above. This means that carbon can take on many different forms with a variety of distinct structures and characteristics, such as mechanical, optical, chemical, and electrical properties. Carbon are typically found in two crystalline allotropes that are comparable to hexagonal crystalline graphite and diamond, Figures 2.3(a) and 2.3(b), respectively. For diamond, all carbon atoms completely from sp^3 bond (all bonds), in which each carbon atom tightly bonds to four other carbon atoms, forming a tetrahedral crystalline network. Diamond is the hardest materials and one of the best electrical insulators, according

to this theory, because of the high bond density, long-lasting bonding, and the fact that all of their electrons are involved in the bonding process.

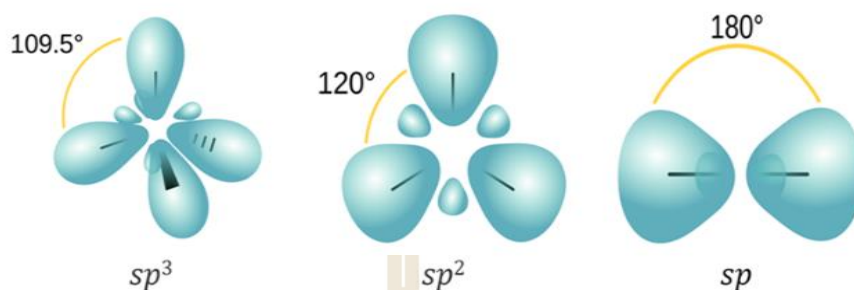


Figure 2.2 The scheme of hybridizations of carbon during bonding. Adapted from (Robertson, 2002).

Graphite has a hexagonal crystalline structure. It is a form of a highly structured network of carbon layers placed on top of each other, as illustrated in Figure 2.3(a). The existence of sp^2 bond in graphite is notable. Each carbon atom within each layer is covalently bonded to three other carbon atoms arranged in hexagonal rings, which is an unusual occurrence. All delocalized bonding takes place above and below the carbon layer, which spans the entire plane. Therefore, electrons can travel freely across graphite sheets. The considerable delocalization of electrons in graphite makes it a superb electrical conductor. The graphite sheets are rather thin, which are attached to one another by weak forces of attraction (known as dispersive van der Waals interactions). It also does not prohibit the sheets from being readily packed one on top of the other. Graphite has a low bulk hardness due to its weak interlayer connections, even though it possesses robust covalent bonding between layers. Fully crystalline fullerenes (0D), carbon nanotubes (1D), and graphene (2D) are three of the most significant low-dimensional forms of carbon materials. They are all distinguished by a mostly sp^2 carbon-bonding network, as illustrated in Figure 2.3(c-e).

2.2 Diamond-like carbon film (DLC)

Diamond-like carbon (DLC) film is a metastable form of amorphous carbon (a-C) film that has a high fraction of sp^3 bonds. It possesses a diverse variety of features,

including excellent mechanical hardness, chemical inertness, optical transparency, and the capability to function as a wide bandgap semiconductor (Casiraghi et al., 2007; Jiang et al., 2003; Kalin et al., 2005; Mercer et al., 2003; Merlo, 2003; Zhong et al., 2009).

The structure of DLC films has a degree of disorder (non-crystallinity), in contrast to the crystalline structure of diamond and graphite, as depicted in Figure 2.4. As can be seen in Figure 2.4. They contain a mixture of sp^2 , sp^3 and sp^1 bonds in their structure (Ferrari, 2004; Robertson, 1992), forming clusters, rings, or chains network configurations. The existence of other components like hydrogen, nitrogen, or metal in the DLC film structure is also possible.

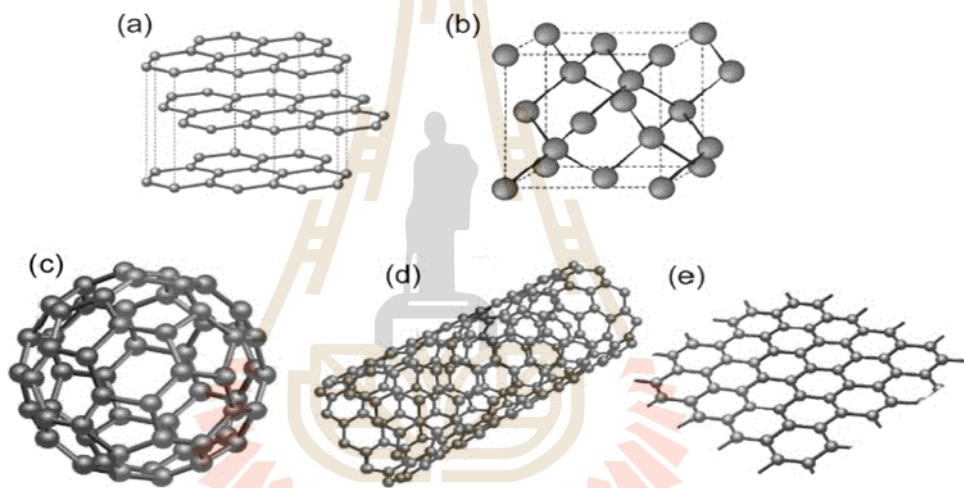


Figure 2.3 Various allotropes of carbon material. (a) Hexagonal crystalline graphite, (b) cubic diamond, (c) C60 fullerene, (d) carbon nanotube, and (e) graphene (Scarselli et al., 2012).

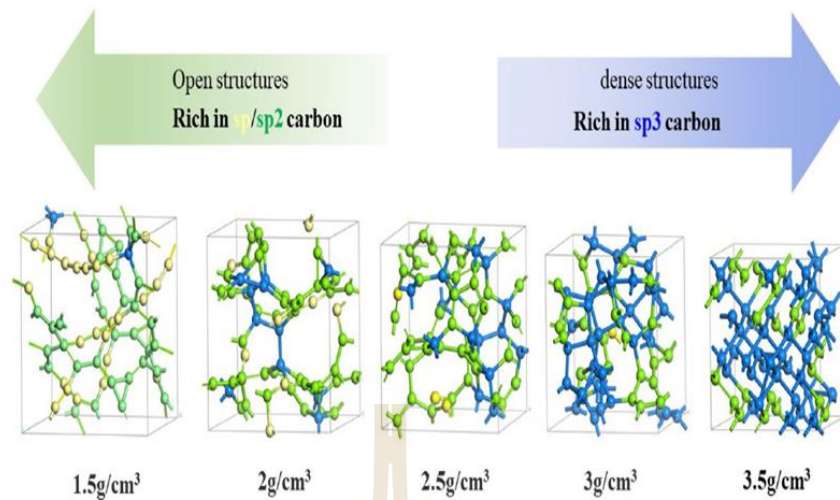


Figure 2.4 Amorphous carbon bonding distributions at 1.5 g/cm³, 2 g/cm³, 2.5 g/cm³, 3 g/cm³, and 3.5 g/cm³ density are depicted in the graphic. The C atom that is sp/sp²/sp³-bonded is represented by the colors yellow, green, and blue, respectively. Reprinted with permission (Liu et al., 2019).

The fraction of sp, sp², and sp³ hybridizations, hydrogen and nitrogen atoms in the film controls the properties of DLC films as shown in Table 2.1 (Robertson, 2002). A higher proportion of sp³ bond results in excellent mechanical and chemical performances, including high hardness, high Young's modulus, low roughening, chemical inertness, and high atomic density. The DLC films can also have low coefficient of friction and wears rate. Due to the absence of grain boundaries, which is a result of their amorphous structure. This allows them to be extremely smooth. The DLC coatings have high electrical resistance and excellent optical transparency. Aside from being non-reactive to chemicals, DLC coatings are also biocompatible and hemocompatible (Jelínek et al., 2010; Roy et al., 2007), making them an excellent choice for medical applications.

Table 2.1 Characteristics of amorphous carbon with diamond, graphite, C₆₀, and polyethylene (Robertson, 2002).

	sp ³ (%)	H (%)	Density (g cm ⁻³)	Gap (eV)	Hardness (GPa)
Diamond	100	0	3.51	55.00	100
Graphite	0	0	2.26	0.00	
C ₆₀	0	0		1.60	
Glassy C	0	0	1.30-1.55	0.01	3
Evaporated C	0	0	1.90	0.40-0.70	3
Sputtered C	5	0	2.20	0.50	
ta-C	80-88	0	3.10	2.50	80
a-C:H hard	40	30-40	1.60-2.20	1.10-1.70	10-20
a-C:H soft	60	40-50	1.20-1.60	1.70-4.00	<10
ta-C :H	70	30	2.40	2.00-2.50	50
Polyethylene	100	67	0.92	6.00	0.01

2.3 Classification of DLC films

DLC films can be categorized into three fundamental groups: hydrogenated amorphous carbon (a-C: H), nitrogenated amorphous carbon (a-C: N or CN_x), and hydrogen-free amorphous carbon (a-C: H). Doped and alloyed DLC films are also available in addition to those listed above.

2.3.1 Hydrogenated amorphous carbon films

In most instances, the elemental composition of nitrogen-free carbon amorphous films is depicted on a ternary phase diagram of hydrogen, sp², and sp³ hybridization, as depicted in Figure 2.5 (Casiraghi et al., 2007).

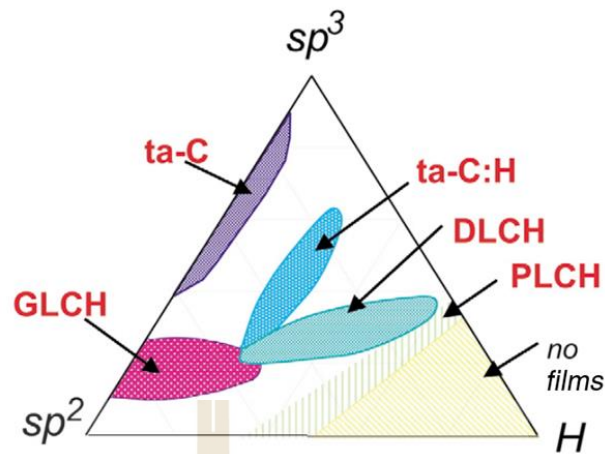


Figure 2.5 Amorphous carbon's ternary phase diagram, the three corners represent diamond, graphite, and hydrocarbons (Casiraghi et al., 2007).

In the ternary phase diagram, amorphous carbons with disordered graphitic structures, such as soot, chars, and glassy carbons, can be found in the lower left-hand corner of the diagram. The bottom right corner of the triangle with a concentration of hydrogen greater than 70% correspond to hydrocarbon molecules or soft polymers films. The top left-hand corner corresponds to a hard solid continuous carbon film which it contains more than 70% sp^3 bond fraction. The majority of these positions are terminated by H-C bonds. When there is an intermediate hydrogen concentration (20-40%), the amorphous carbon is referred to as amorphous hydrogenated carbon (a-C: H). This group is classed as DLC since it has a considerable amount of C-C sp^3 bond in its composition. This group is depicted as being positioned in the center of the ternary diagram. The a-C: H films, can be fabricated by using, the deposition techniques, such as cryogenic deposition of carbon in the presence of hydrogen gas (reactive sputtering) or plasma-enhanced chemical vapor deposition utilized in conjunction with hydrogen gas (Ferrari, 2004b). The C-C sp^3 bond contents can be increased up to 70%, while keeping the hydrogen content in the range of 25 and 30% atomic by using deposition methods utilized a high-density plasma source. These deposited films are referred to as tetrahedral hydrogenated amorphous carbon (ta-C: H) films as they contain hydrogen (H) as well as a covalent network of carbon atoms that are tetrahedrally (sp^3) bonded to one another. The mechanical properties of these films outperform those of a-C: H films.

2.3.2 Hydrogen free diamond-like carbon films

In the absence of hydrogen, simple sputtering of graphite results in the formation of an amorphous carbon (a-C) film with deficient C-C sp^3 bond and no hydrogen content. This type of carbon is soft, but it is dense which can be employed as a corrosion-resistant coating. Tetrahedral amorphous carbon (*ta*-C) film is a type of amorphous carbon film that is devoid of hydrogen and contains a large proportion of C-C sp^3 (tetrahedral) bond. This film can be formed using deposition methods that are utilized highly ionized plasma with nearly identical ion energy, such as filtered cathodic vacuum arc (FCVA), mass-selected ion beam (MSIB), and pulsed laser deposition (PLD) (Casiraghi et al., 2007; Robertson, 2002; Schultrich, 2018). The chemical structures and properties of *ta*-C films varies with the energy of C^+ ion during the deposition. Numerous research groups have demonstrated that the maximum sp^3 fraction can be achievable at the ion energy of ~ 100 eV (Chhowalla et al., 1997; Fallon et al., 1993; Ferrari et al., 2000). The high sp^3 bond fraction up to 85% can be determined by using characterization techniques, such as, electron energy loss spectroscopy (EELS), XPS, or Raman spectroscopy. This results in superior mechanical and chemical properties when compared to those of sputtered or other types of amorphous carbon films. The carbon films with sp^3 bond content of 15-30% can be produced through the sputtering technique. The mass density, hardness, elastic modulus, and internal compressive stress of the films are also proportional to the high sp^3 bond content. The nanoindentation studies have shown that the *ta*-C films produced at ~ 100 eV exhibit the maximum hardness of ~ 80 GPa, compared to that of ~ 20 GPa for the films prepared by sputtering technique (Pharr et al., 1996). The surface roughness of the *ta*-C films produced at 100 eV is very small (~ 0.1 nm) (Casiraghi et al., 2003), and the mass density of the *ta*-C films measured by Rutherford backscattering spectroscopy (RBS) or EELS is at the maximum of 3 g/cm^3 , which is close to that of the diamond (3.52 g/cm^3) (Casiraghi et al., 2007).

The FCVA films adherence to the substrate can be affected by extreme stress. As an underlayer, elements like Si, Cr, Ti, W, or Mo can be employed to improve the carbon film's adherence to the substrate. A multilayer film with hard and soft carbon and other materials layers, or carbon layers with varied sp^3/sp^2 percentages,

can also reduce stress levels in the film. This makes it easier to create thicker, more durable films (Anders et al., 1997). In most applications, the temperature stability of films is also crucial. At higher temperatures, carbon films can graphitize, causing the film's characteristics to deteriorate (Erdemir et al., 2006; Robertson, 2002). It has been reported that hydrogenated carbon films become softer at temperatures of 350-400°C (Dischler et al., 1983). The *ta*-C films can retain their hardness and sp^3 bond concentration at temperatures as high as 600°C (Fallon et al., 1993; A. Ferrari et al., 1999; McKenzie, 1996).

The excellent mechanical properties of *ta*-C film allow them to act as a coating layer or barrier against corrosion and wears in many fields with very low dimensional tolerances such as microelectromechanical systems (MEMS) and hard disk drives (Marchon el al., 2009; Pathem et al., 2013; Robertson, 2008).

2.3.3 Nitrogenated amorphous carbon films

The incorporation of nitrogen into amorphous carbon films has significant effects on the films physical and chemical properties because graphite planes are tightly crosslinked together (Silva et al., 1997). Despite the fact that the sp^2 bond content remains high, the mechanical characteristics of the film (elastic recovery and hardness) is improved due to the increased disorder in the material. Amorphous carbon films with nitrogenated tetrahedral structures (*ta*-C:N_x) can be formed under very low-pressure N₂ atmosphere by using deposition processes that generate highly charged plasma, such as mass selected ion beam deposition (MSIB), and pulse laser deposition (PLD). The high sp^3 bond content as high as 80% can achieved. The nitrogen amorphous carbon films could be used as protective layers on the surfaces of magnetic hard disks to prevent corrosion and wear from occurring (Yamamoto et al., 2000).

2.3.4 Alloyed amorphous carbon films

In previous research, it has been demonstrated that compressive internal stress plays an essential role in the development of sp^3 bond and mechanical properties of DLC films (hardness and elastic modulus) (Koskinen et al., 1998). In particular, the thick DLC films are extremely prone to delamination due to the internal

stress. This results in the failure of the coating when subjected to strong loads and impacts. Excellent adhesion between the film and the substrate is therefore required for the formation of DLC films with high compressive stress. Otherwise, the film will delaminate or peel off the surface by increasing the film thickness (internal stress increases with the thickness of the film) or applying external loads. Alloying carbon films with certain metals or non-metallic materials may be able to overcome some of these constraints and improve the mechanical properties of the carbon films themselves. For example, alloying DLC films with silicon can enhance the formation of sp^3 bond when there is no strong compressive stress (Jiang and Arnell, 2000; Varanasi et al., 1997). The addition of Si not only improves the thermal stability when exposed to high temperatures, but also improves the frictional behavior when exposed to increased relative humidity. A similar approach is used to increase the hardness and toughness of carbon sheets by alloying them with metals such as copper, nickel, or aluminum (Koskinen et al., 1998).

2.4 Ultrathin DLC overcoats

Recently, protective carbon overcoat (COC) films have been highly demanded for high density recording technology in the magnetic hard disk drive industry. Carbon-based films are widely used as wear and corrosion protecting coatings in hard disk systems. One essential requirement is to make the protective carbon overcoat (COC) films as thin as possible (Marchon et al., 2013), as described in Chapter I. The main challenge, particularly, is to produce the COC with the thickness of less than 20\AA (Goohpattader et al., 2015). Liu et al. investigated the thickness dependency of the structure of ultrathin (Range: 0.8-10 nm) ta -C films deposited by FCVA with visible and UV Raman spectroscopy (Liu and Wang, 2009) and found that the thickness was dependent on the structure of the films. The results revealed that when the film thickness was less than 20\AA , the film was not continuous, and contained less sp^3 bond content than expected. It has been observed that for films with thicknesses between 20\AA and 50\AA , the sp^3 site moves abruptly to a higher value in 2.0 nm and then remains nearly steady above 5.0 nm. Li et al. used molecular dynamic modeling to

explore the effect of thickness on the characteristics and structure of ultrathin *ta*-C films. The thickness of ultrathin DLC films varies between 23.19 Å and 57.97 Å when deposited at 10 eV/atom and 70 eV/atom, while the growth rate is variable. In the simulations, it was discovered that increasing the thickness of ultrathin *ta*-C films decreased both the density and the residual compressive stress of the films. The incident kinetic energy of the deposited atoms was found to be a significant factor in the gradient of characteristics with thickness. Soin et al. investigated the microstructural properties of ultrathin (10-100 nm) films as a function of thickness by Near Edge X-Ray Absorption Fine Structure (NEXAFS) spectroscopy. It revealed the presence of surface defects (C-H bonds) that rapidly diminish as the film thickness increases. The change in π^* C-C peak as film thickness increases suggests that the sp^3 contents is being promoted by the film thickness. The investigation also indicated that the film surface roughness, as measured by AFM (Soin et al., 2012), remained constant during the course of the experiment. When it comes to such films, the transition layer between the substrate and the top layer is a critical component of the overall film structure. As a result, the averaged structural characteristics and film properties will be dependent on the thickness of the layer of film. The mechanism of development of sp^3 bond growing is also disclosed to their deposition process involving energetic carbon ions (Beghi et al., 2002; Davis et al., 1998; Li et al., 2013; Zhu et al., 2008). Despite significant progress in the DLC film fabrication methods, the ability to generate ultrathin (2.0 nm) coatings while maintaining the integrity of magnetic properties in the head and media, improved tribological behavior, and wear resistance has remained virtually unexplored. In this work, we present a comprehensive study focusing on the thickness dependence, deposition time (count pulse), film interlayer interface with substrate, and film interlayer interface with substrate on the structural and tribological characteristics of an ultrathin *ta*-C overcoat for magnetic layers.

2.5 Deposition Mechanism of sp^3 bond formation of DLC

The sp^3 bond, as is widely known, is critical in achieving excellent properties of DLC such as high density, high mechanical hardness, and high

chemical inertness. It has been demonstrated that DLC films with a high sp^3 content fraction exhibit great thermal stability and a minimal level of graphitization when thermally annealed at high temperatures up to 1270 K. In general, it is recognized that the amount of sp^3 bond content in DLC films is highly reliant on the energy efficiency of the DLC film deposition technology used. When using a deposition process such as thermal evaporation, which is a common method of physical vapor deposition (PVD), carbon species (ions and atoms) generated under a vacuum have low kinetic energies in the order of kT magnitude, approximately 0.025 eV at ambient temperature. The deposited carbon films with very high sp^2 and very low sp^3 bond content (~1-12% for sp^3 bond content) (McKenzie, 1996; Robertson, 2002). The insufficient kinetic energy required to advocate the electron transfer from the 2s to the 2p orbital in carbon atoms and form carbon films with a high content of sp^3 hybridization can be attributed to this reflection (Sánchez-López et al., 2008). The deposition techniques, such as sputter deposition, ion-assisted deposition, ion beam deposition, and cathodic arc deposition utilize kinetic energies of carbon species ranging from 2.5 to 25 eV.

The "subplantation model," developed by Lifshitz et al. (Lifshitz et al., 1990), describes the growth mechanism of carbon films by carbon hyperthermal species (with energies ranging from 1 to 1000 eV) that are involved in a shallow subsurface implantation process. This model can be used to justify the variation of sp^3 and sp^2 hybridization with energy of carbon species in the growth process. In this model, the carbon species (ions and atoms) that enter the expanding carbon film interact with it in a high-energy manner and can infiltrate the film's subsurface illustrated in Figure 2.6. This results in either direct penetration trapping of entering carbon species into films or preferred displacement (knock-on) of the existing sp^2 bound carbon, depending on the nature of the incoming carbon species. Therefore, the density of the subsurface of the expanding carbon film increases, resulting in the transformation from sp^2 to sp^3 hybridization (Robertson, 1993; Robertson, 2005).

Following the subsurface penetration, some carbon atoms relax towards the surface, generating a sp^2 -rich layer on the surface. The fraction of energetic ions capable of reaching the surface via the subplantation process ($f\phi$) and the fraction of trapped interstitials relaxing towards the surface ($n\beta$) are schematically shown in Figure 2.7. n

= $f\phi - n\beta$ is the fraction of ions that remain in interstitial locations and contribute to densification.

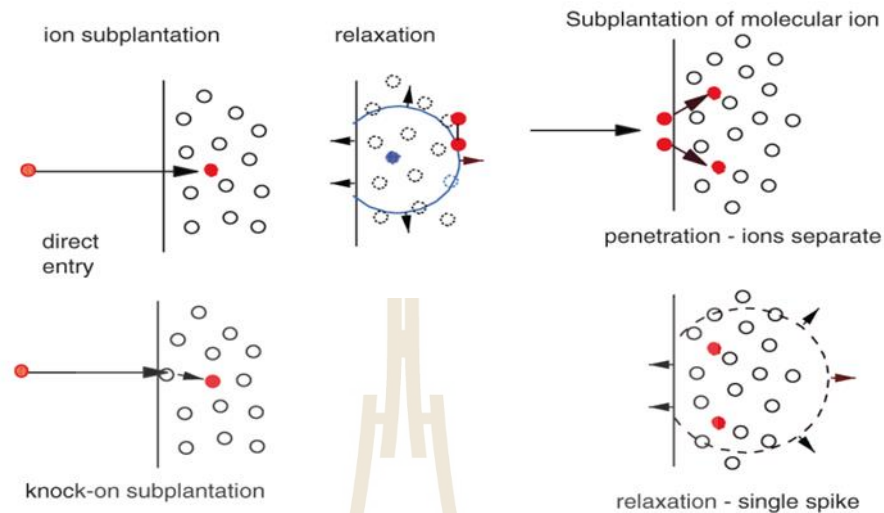


Figure 2.6 The subplantation model developed by Lifshitz et al. (Lifshitz et al., 1990): energetic carbon species penetrate the developing carbon film's surface, and preferentially displace sp^2 -bonded carbon atoms, resulting to. to the increase of film's density and sp^3 bond content. Reprinted (Robertson, 2002; Sánchez-López et al., 2008).

The subplantation mechanism is dependent on the arrival of carbon species reaching a particular energy threshold before it can be activated. Consequently, at low energies (less than 10 eV), carbon species do not have enough momentum to penetrate the developing carbon film, and the incidence of subplantation is insignificant in such instances. Furthermore, in the early stages of film formation, extremely limited displacement or mobility of carbon species may be readily detected, and the entering carbon species are trapped as interstitials inside the growing film, resulting in the formation of a disordered network of carbon species. Graphitic films with a high degree of sp^2 bond are formed as a result of this process. With moderate energies (between ~ 30 and 500 eV), the preferential displacement mechanism is influenced, which favors the formation of sp^3 bond and reduces the number of graphitic sp^2 sites, allowing the formation of a large sp^3 large fraction of bond. However, if the energies are too high (between ~ 500 and 1000 eV), the growing carbon film can be readily destroyed and amorphized, resulting in the formation of amorphous carbon. As a result, for each deposition method and tool, there is an optimal deposition energy range in the medium energy regime for obtaining DLC films with the maximum sp^3 bond

concentration. This optimal deposition energy range is found in the medium energy regime (Yeo, 2017).

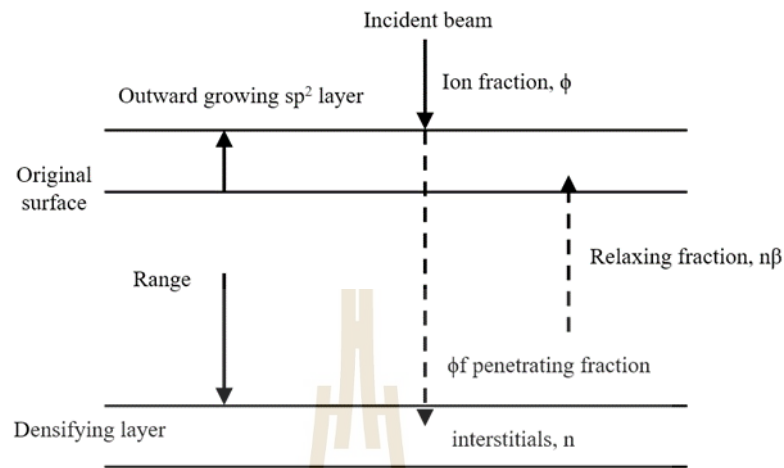


Figure 2.7 Flow diagram illustrating the fraction of incoming ions that contribute to film densification, interstitial trapping, and surface relaxation Reprinted (Robertson, 2002).

Numerous researchers have successfully fabricated the DLC films using the techniques that utilize carbon species with inherent energy in this range, including ion beam deposition (IBD), ion-assisted deposition, laser ablation, cathodic layer deposition, and sputtering (Lifshitz, 1999; Schultrich, 2018). However, to create highly sp^3 hybridized DLC films such as ta -C, C^+ ions are frequently used as the species for film formation due to the possibility of moderating the energy of incoming ions to the substrate via a proper substrate bias. Aisenberg and Chobot, grew the first DLC films using an ion beam deposition process in 1971 with a ~ 40 V substrate bias. Using ion energies ranging from 20 to 300 eV, ta -C with sp^3 bond content of 70-90% has been achieved (Aisenberg et al., 1971; LIBASSI). Recently, it has been demonstrated that the optimal energy range for creating a high sp^3 bond content is between ~ 80 and 120 eV (Chhowalla et al., 1997; Fallon et al., 1993; Polo, Andujar et al., 2000; Zhu et al., 2008).

2.6 DLC fabrication techniques

DLC films can be fabricated using a variety of physical or chemical deposition processes, including ion beam deposition (IBD), mass-selected ion beam deposition (MSIBD), sputtering, pulse laser deposition (PLD), and vacuum arc deposition (VAD)

(Robertson, 2002). Each technique has its own set of advantages and disadvantages. The deposition techniques and parameters also have a direct effect on the characteristics and properties of the films. Currently, the IBD, PECVD, and FCVA are the most frequently used techniques for depositing ultrathin carbon overcoats in the HDD industry. PECVD is currently employed to deposit an a-C: H based carbon overcoat on the magnetic disk medium, while FCVA is widely used to deposit the carbon overcoat on the slider and reader/writer head. This section discusses these three fabrication techniques that are employed in the industry.

2.6.1 Ion beam deposition

The first DLC film fabricated by IBD was first reported by Aisenberg and Chabot in 1971 (Aisenberg et al., 1971). Since then, the IBD technique has become the most widely used technology and have been modified and developed for more specific coatings in a range of different uses. A schematic diagram of the generation of carbon ions by plasma between an electrode and a grid in the IBD technique is shown in Figure 2.8. This technique employs a focused beam of Ar or Kr ions to generate carbon ions on a graphite cathode through plasma sputtering (target). A magnetic field is used to confine the plasma and increases the amount of ionization. Electron sputtering deposition (MSD) is accomplished by positioning magnets behind the graphite target, causing electrons to spiral and extend their trajectories, so boosting the ionization rate of the plasma. When hydrocarbon gas is directly injected into the plasma, this method is made even more effective. The grid electrode acts as a propulsion device for carbon ions in a high vacuum environment, propelling them towards the substrate. The effect of these ions on the target causes the formation of sp^3 bond

2.6.2 Plasma enhanced chemical vapor deposition

Plasma enhanced chemical vapor deposition (PECVD) is a type of chemical vapor deposition (CVD) process in which the use of a plasma helps to improve the reaction between the precursor gases and the substrate, allowing film deposition to take place at room temperature. It is schematically shown in Figure 2.9. In this technique, precursor hydrocarbon gases, such as methane and acetylene are fed into a pair of electrodes which are placed in an enclosure.

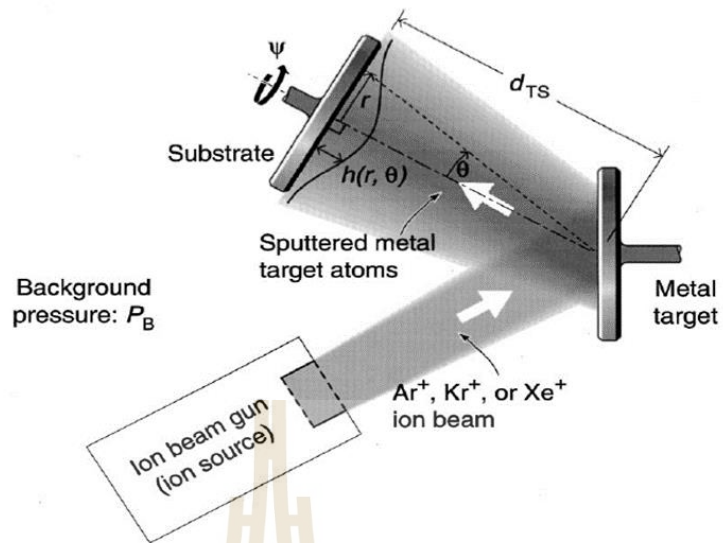


Figure 2.8 Schematic diagram of an IBD system (Zhou and Wadley, 2000).

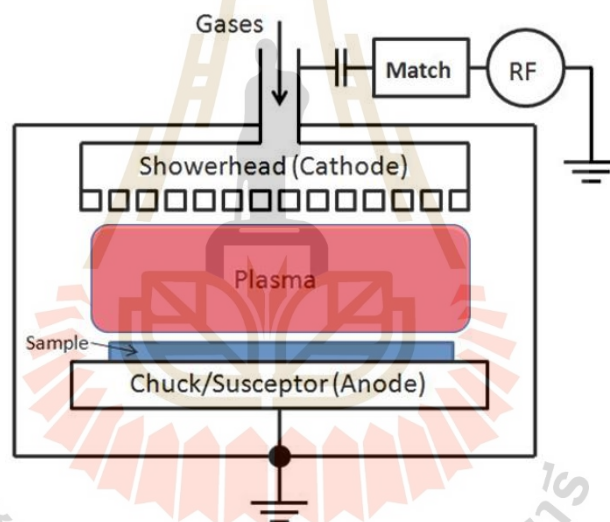


Figure 2.9 Schematic diagram of plasma-enhanced chemical vapor deposition system, reprint(WIKI).

The substrates are installed on the powered electrode that is much smaller in size than the opposing electrode (usually the whole chamber body itself connected to the ground). This configuration maximizes the amount of energy transferred to the powered electrode. However, a conventional PECVD process has low ionization rates and generates a large number of neutrals and radicals. Therefore, numerous versions of the PECVD method have been developed to produce plasmas with higher densities and higher ionization levels. Some of these PECVD-based methods include plasma beam source (PBS) deposition (Casiraghi et al., 2007) and

electron cyclotron wave resonance (ECWR) deposition (Merlo, 2003), which confine the plasma using a magnetic field and then extract it as a high-energy plasma beam. This allows for the formation of highly sp^3 bond a-C: H films. Currently, these modified PECVD methods are currently used for deposition of media overcoats in HDD industry (Robertson, 2008; Zhang et al., 2015).

2.6.3 Filtered Cathodic Vacuum Arc

Cathodic vacuum arc deposition is a type of physical vapor deposition that is widely utilized in industry and research due to its ability to adjust the deposition energy of ionized carbon species during the deposition process. The cathodic arc deposition is driven by an arc under a high vacuum environment. A sufficient current is introduced between the anode and the cathode (target) to generate an arc, which generates a highly ionized plasma with an unusually high ions-to-neutrals ratio. This results in the ejection of neutrals (target particles) as well as charged species (ions and electrons) at high velocities towards the target. It is possible to manipulate the energy of ions by introducing a bias to the substrate, which in turn allows for the manipulation of the microstructure of the film. For the carbon film deposition, a graphite rod is typically used as a target. During the deposition process, carbon ions (mostly singly charged C^+) and carbon macroparticles are ejected from the target. The diameters of these macroparticles range from a few hundred nanometers to several tens of microns. This may cause defects in the carbon film, a decrease in the sp^3 bond content, and an increase in surface roughness, which are undesirable. This problem can be reduced by installing a curved magnetic filter coil, such as an S-bend coil, as shown in Figure 2.10. When applying the current, this magnetic coil generates a magnetic field is created in the center of the filter, allowing the ionized plasma of electrons and C^+ ions to follow the curved magnetic field through the bend and exit the other side. Microparticles with a neutral charge, on the other hand, do not follow the magnetic field and are filtered out of the plasma (Martin and Bendavid, 2001; Vetter, 2014). This modified technique is widely known as FCVA deposition technique. The C^+ ions that are ejected from the cathode during the FCVA deposition of carbon have an average intrinsic energy of approximately 20-30 eV (Ean et al., 2017; Sheeja et al., 2000). A negative bias can be

applied to the substrate in order to tune the energy of the C^+ ions that arrive at the substrate in particular.

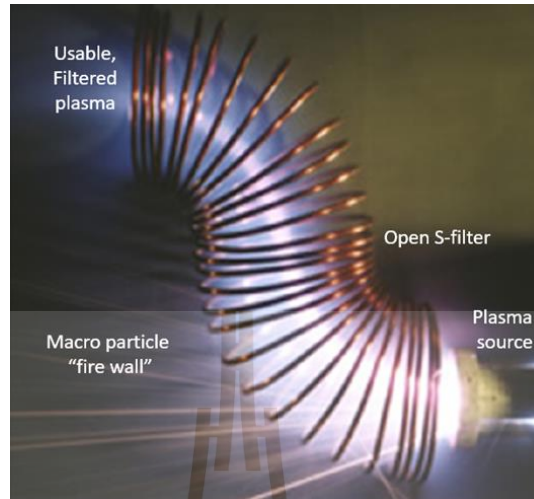


Figure 2.10 Photograph of FCVA deposition system with an S-bend macroparticle filter with two 90° bends. Bright streaks are macroparticles that are being filtered out of the plasma (Anders et al., 2001).

In this way, carbon films with particular characteristics and properties can be deposited by tailoring the C^+ ion energy to a specific value. While including a filter in FCVA helps significantly reduce the number of macroparticles that reach the substrate, it is still difficult to entirely eliminate them from the system. This is crucial for hard disk media overcoats fabrication since the presence of macroparticles has a severe effect on the HDI's overall reliability and performance. Several research projects are currently underway to address this issue, including developing a real-time electrical filter (Herrera-Gomez et al., 2007; Inaba et al., 2003). It is also possible to use alternative techniques, such as high-power pulsed impulse magnetron sputtering (HiPIMS), to generate C^+ with regulated energy in an Ar atmosphere without generating macroparticles (García et al., 2020). In this thesis, the FCVA method is used to fabricate the ultrathin DLC overcoats.

2.7 Influence of deposition conditions on a *ta*-C film structure.

A number of publications have discussed the influence of deposition conditions on the structure and properties of the produced amorphous carbon films. Even though

the outcomes of different groups tend to follow similar patterns, there might be some significant differences in the quantitative values and even in the qualitative characteristics. Many factors contribute to these variances, including:

2.7.1 Incident carbon ion energy

The incident carbon ion energy is a critical parameter for the formation of *ta*-C films. The dependence of the film microstructure and growth evolution on deposition energy has been explored to optimize the deposition condition (Cuomo et al., 1992; P. J. Fallon et al., 1993; Li et al., 2013). Li et al. used molecular dynamics simulation to study the density, residual stress, and sp^3 fraction dependencies. The morphologies for DLC films with incident energies of 1 eV/atom, 70 eV/atom, and 150 eV/atom are shown in Figure 2.11, where colors reflect different coordination numbers. A film with considerable roughness is produced when the incident energy is 1 eV/atom, as ascribed in Figure 2.11(a). The incident atoms have small effect on the arrangement of substrate atoms, resulting in an evident interface between the film and the substrate. When the incident energy is 70 eV/atom, which is much higher than the cohesive energy of diamond (7.6-7.7 eV/atom), the incident atoms can implant into the diamond lattice, resulting in the intermixing layer at the interface. This may induce high stress due to impairing the recombination process as shown in Figure 2.11(b). When the incident energy is 150 eV/atom, the structure becomes looser with more flaws, reflecting a change in mechanical characteristics (Li et al., 2013).

As shown in Figure 2.12, the density, residual stress, and sp^3 bond fraction are dependent on the incident energy. The density, residual compressive stress, and sp^3 bond fraction grow rapidly with the incident energy, and then progressively decline. The density reach the maximum of 3.0 g/cm^3 with a compressive stress of 15.5 GPa and sp^3 bond percentage of 33% when the incident energy is 70 eV/atom. In addition, the residual stress shifts from a tensile to a compressive condition as a function of incident energy. The reduction of sp^3 bond fraction at higher incidence energy indicates that the created sp^3 bond structure is broken by high-energy deposited atoms.

Figure 2.13 describes the relation between surface roughness determined by AFM and the sp^2 bond fraction of 100 nm carbon films on silicon substrates using C^+ energies ranging from 5 eV to 20 keV at room temperature. It should be noted that the suppression of the sp^3 bond content is accompanied by a massive rise in the surface roughness at both low and high energy.

At low ion incident energies < 20 eV, the film growth is a pure surface, where the film grows by clustering atoms condensed on the surface. The films are amorphous and nearly completely sp^2 bonded. A low sp^3 bond fraction of approximately 10% results from the distorted network due to the film growth by the formation and coalescence of separated islands.

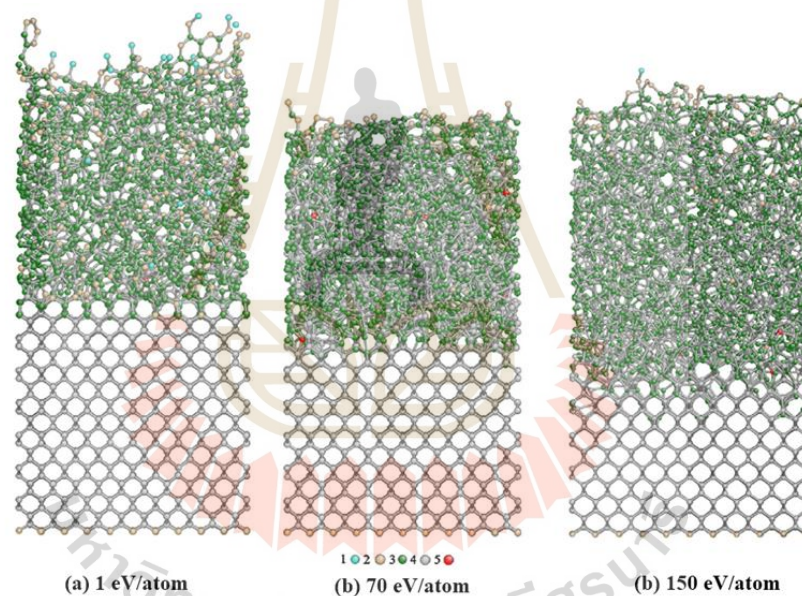
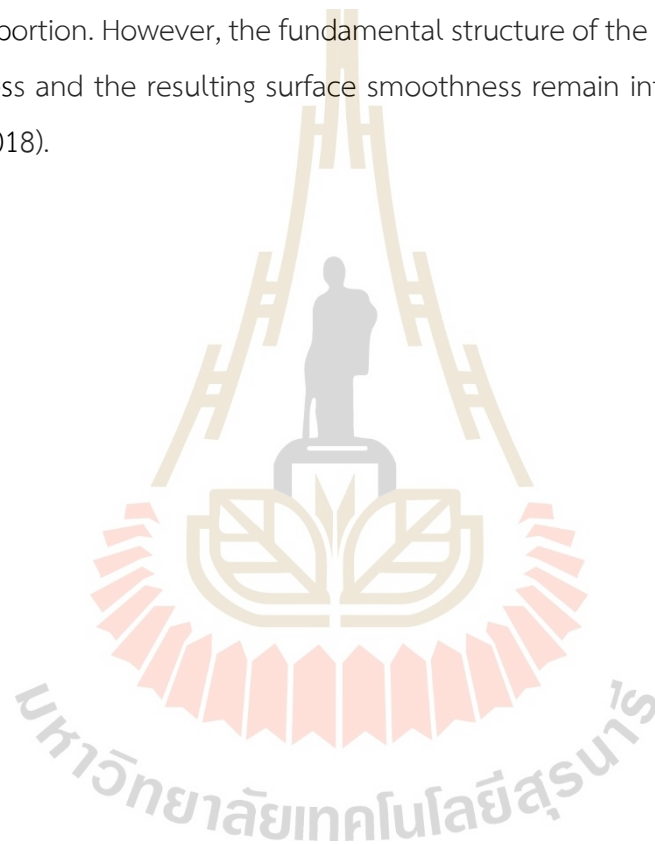


Figure 2.11 Coordination configurations of films under different incident energies, where colors represent the different coordination numbers (Li et al., 2013).

Between 20 and 30 eV, the ion energy exceeds the penetration threshold. The carbon atoms immediately beneath the surface are displaced. The film grows from the inside without significantly altering the surface topography, which is highly smooth. Significant compressive stresses are generated because extra atoms are incorporated into the existing structure (at least briefly). They facilitate the creation of sp^3 bonds, allowing for more densely packed structures. The sp^3 bond fraction exceeds

50% for ion energies greater than roughly 25 eV, which is comparable to the characteristics of *ta*-C films.

The structure become virtually independent of the ion energy between 70 and 300 eV. The sp^3 bond percentages is around 80%. A steady drop above 300 eV follows the modest maximum at around 100 eV. With increased energy, the ion impact's destructive effect becomes more apparent. The relaxation through migration towards the surface is favored by radiation accelerated diffusion, resulting in a decrease in the sp^3 bond proportion. However, the fundamental structure of the internal subplantation growth process and the resulting surface smoothness remain intact (Robertson, 2002; Schultrich, 2018).



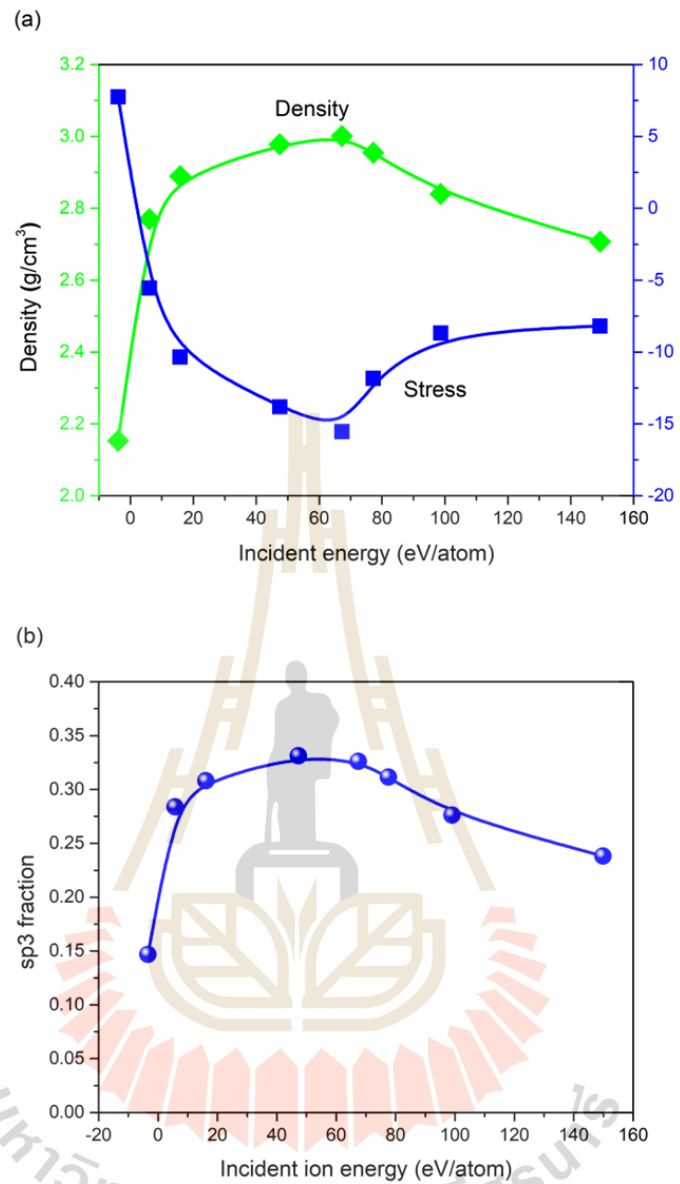


Figure 2.12 Dependence of (a) density, stress, and (b) sp^3 bond fraction on incident energies (Li et al., 2013).

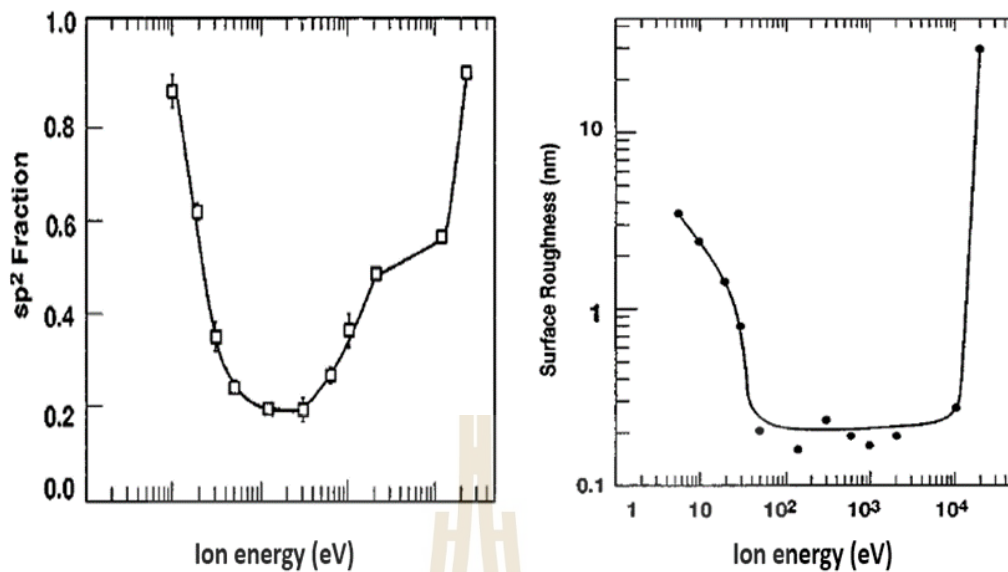


Figure 2.13 The interdependency of the sp^2 fraction and the surface roughness on ion energy up to 20 keV. Reprinted (Grossman et al., 1996).

2.7.2 Incident energetic carbon ion angle

The effects of the incidence angle of energetic carbon ions have been investigated on thickness, topography (roughness), and structure of ultrathin ta-C film synthesized by filtered cathodic vacuum arc (FCVA) (Cuomo et al., 1992; Liu et al., 2003; Wang and Komvopoulos, 2012). The researcher reported that the ta-C film thickness decreases with the increase of the incidence angle as shown in Figure 2.14. The T-DYN simulation result showed that the total carbon and intermixing layer thickness strongly correlated with the incidence angle and ion fluence. The thickness of graphite-like surface layers can greatly affect the sp^3 bond content measured by XPS. The electronic structure of sp^3 bond content depends on the deposition angle. When the deposition angle is varied from 30° to 77° , the sp^3 bond content rapidly increases, then decrease at a slow rate as the deposition angle is over 77° . Liu et al reported the ta-C films deposited by FCVA method at oblique angles (Liu et al., 2007). The angle of the substrate was changed from 0° to 60° . It was observed that the films have less sp^3 bond content and more sp^2 clustering as the angle of the substrate changes from 0 to 60° for both thicker films of 70 nm and thinner films of 2 nm. The Raman spectroscopy study also showed that tilting the substrate strongly influenced the internal stress, while it had small effect on the hardness. This is because the hardness is directly

related to sp^3 bond content, but the internal stress is related to the order of sp^2 cluster.

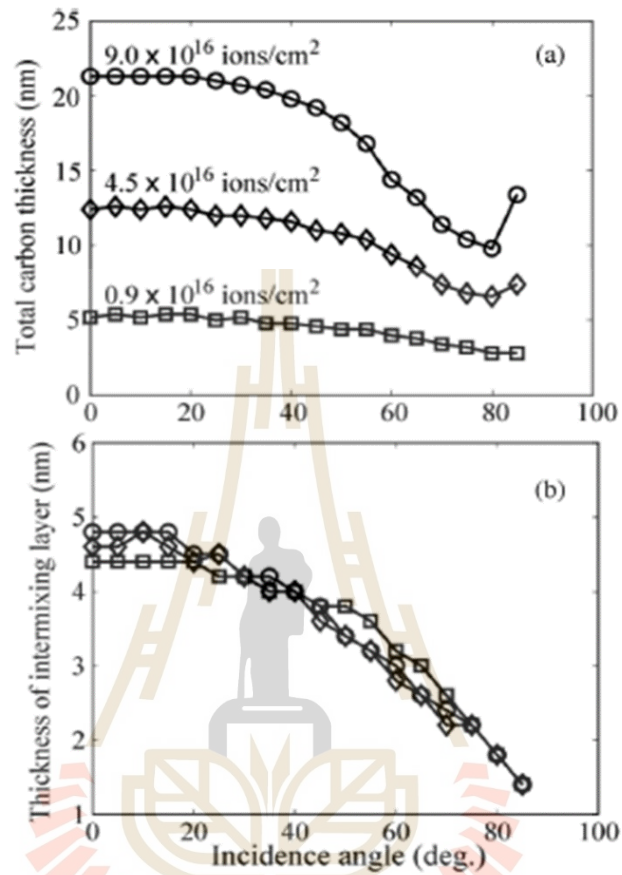


Figure 2.14 Dependence of (a) total thickness of *ta*-C films and (b) thickness of intermixing layer obtained from T-DYN simulations. C^+ ion influence is in the range of $(0.9-9.0) \times 10^{16}$ ions/cm² (Wang and Komvopoulos, 2012).

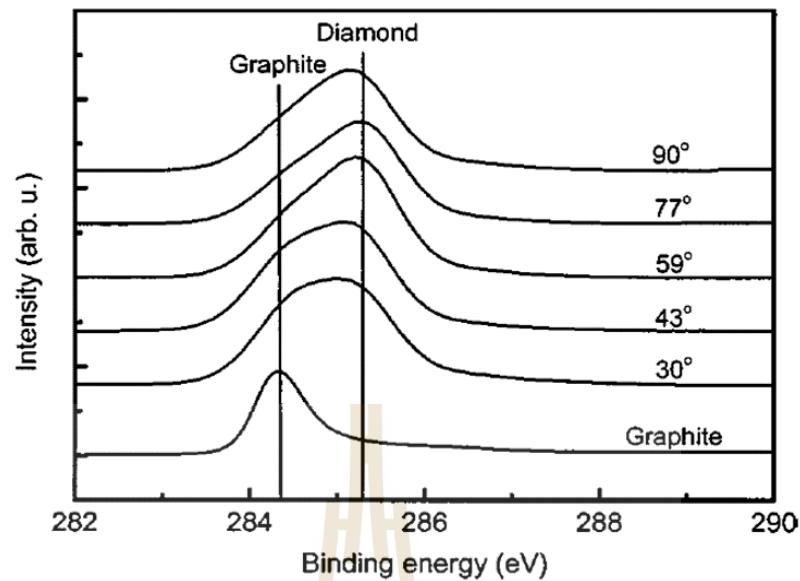


Figure 2.15 XPS C1s peak of a graphite sample and the DLC films obtained at various deposition angles.

2.7.3 Substrate temperature and deposition rate.

For the *ta*-C films deposited with carbon ion energy range between some ten and some hundred eV, the substrate temperature does not significantly influence the structure and properties of films, if it doesn't exceed a certain temperature T_c . Above the temperature T_c , the roughness and density sharply jump as shown in Figure 2.16 (Kulik et al., 1995; Lifshitz et al., 1995; Lifshitz et al., 1993). This jump relates to the transition from an amorphous structure with dominating sp^3 bond to particularly sp^2 bond films with strongly distorted graphitic structure (Schultrich, 2018).

Lau et al. studied the deposition of carbon sheets using IBD method at ion energies ranging from 15 to 500 eV and temperatures ranging from 25 to 800°C (Lau et al., 1991). At elevated temperatures, the Raman spectroscopy result showed that the almost symmetric peak of about 1540 cm^{-1} , which is the characteristic of *ta*-C films, split into two distinct graphitic D and G peaks at 1350 and 1600 cm^{-1} , as shown in Figure 2.17.

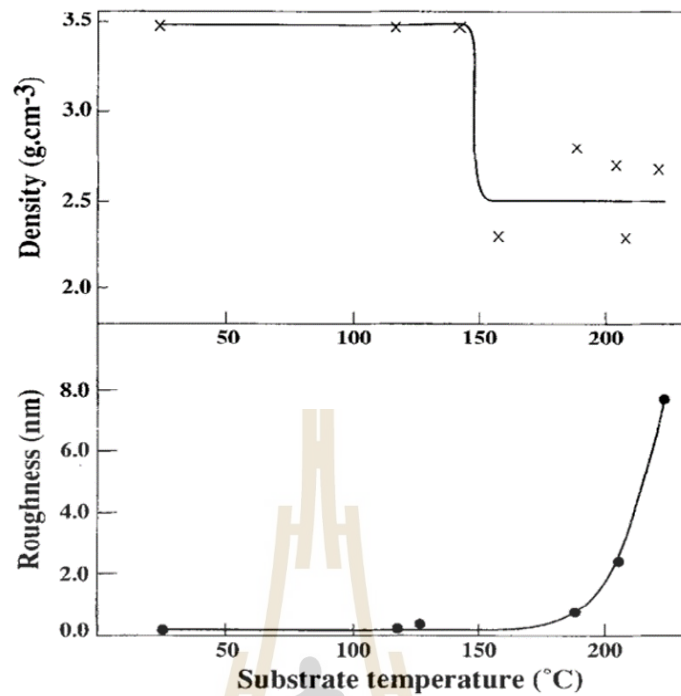


Figure 2.16 The relationships between the surface roughness and density of 1000 Å carbon films deposited using MSIBD with 120 eV ions and deposition temperature (Lifshitz et al., 1995).

The influence of increasing temperatures on films deposited by vacuum arc discharge or pulsed laser deposition is similar to that observed in the MSIBD films. The sp^3 bond concentration decrease above a threshold temperature, which shifts to higher values for higher ion energies. However, the deposition rates must be considered when they significantly decrease (Tay et al., 1999; Tay et al., 1999). When the deposition rates are high, transition temperatures can rise to 200°C, and even higher instantaneous deposition rates of up to 1000 nanometers per second can be achieved without significant heating by using intense pulsed deposition with low repetition frequencies, which can raise T_c to 400 degrees Celsius (Gago et al., 2005; Koskinen et al., 1998), as illustrated in Figure 2.18.

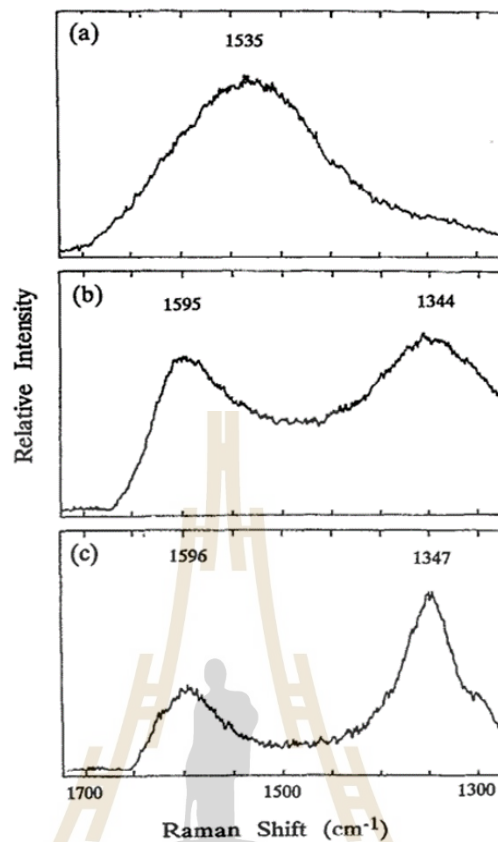


Figure 2.17 The evolution of Raman spectra of the carbon film deposited at (a) room temperature, (b) 400°C and (c) 800°C.

This leads the energy transfer from the impinging energetic ions can result in higher temperatures at the surface as compared to the temperature recorded within it. The critical temperature can then reduce with increased ion energy, in contrast to ion beam deposition or pulsed deposition, which both produce less heating and result in high critical temperatures. As illustrated in Figure 2.19, the critical temperature for DC vacuum arc deposition with a relatively fast growth rate of 2 nm/s decreases from 200°C for 90 eV ions to 140°C for 130 eV ions (Chhowalla et al., 1997). when using high-energy ions. The heating effect is certainly shown by the reduction in the sp^3 fraction that occurs with subsequent film development. When using the 90 eV/300°C deposition method, the initial sp^3 contents of approximately 65% has already been reduced to approximately 10% after 60 nm (Davis et al., 1998). The increase in surface temperature of around 80 K was attributed to the effect by the authors. By increasing the growth rate from 0.2 to 2 nm/s, the optimum ion energy for maximum

sp^3 content changes downward from 106 to 90 eV, and the maximum sp^3 content reduces from 88 to 80% (Chhowalla et al., 1997; Tay et al., 1997).

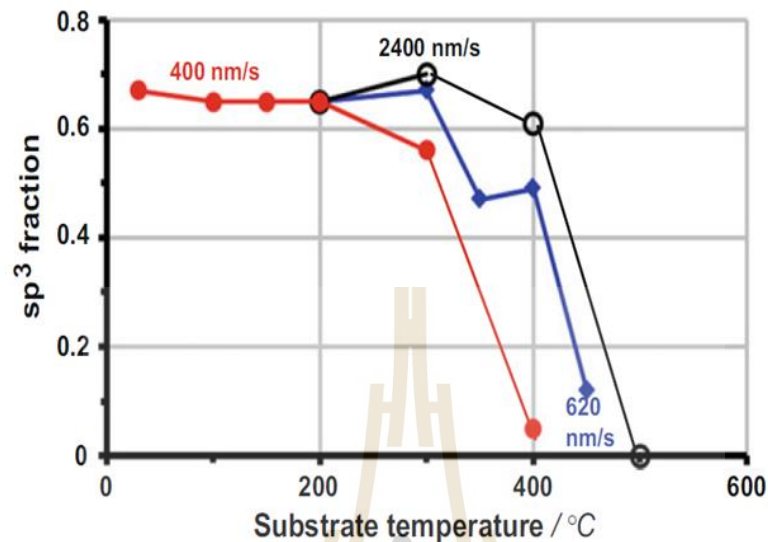


Figure 2.18 The relationship between the sp^3 bond content of DLC films and deposition temperature for deposition by high current pulsed vacuum arc discharges (ion energy ≈ 50 eV) with high instantaneous growth rates during the pulse (Gago et al., 2005; Koskinen et al., 1998; Schultrich, 2018).

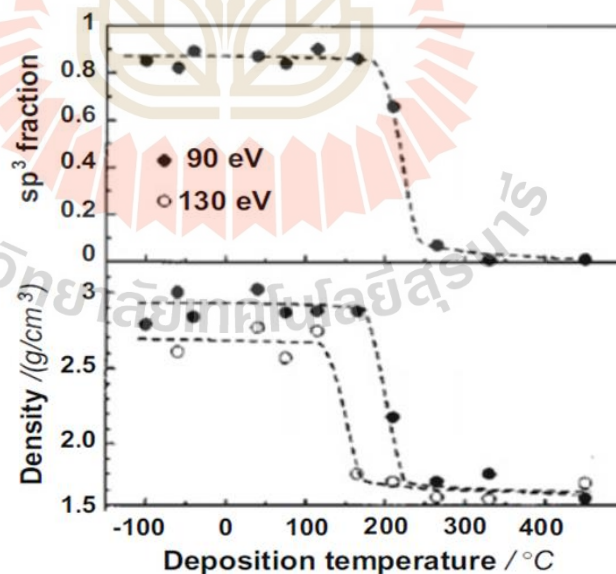


Figure 2.19 Dependence of sp^3 fraction and density on the substrate temperature for DLC films deposited by DC vacuum arc discharge with MSIB at the growth rate of 2 nm/s (Chhowalla et al., 1997).

2.7.4 Substrate morphology

The influence of substrate morphology on the growth of DLC films has been previously investigated. Zhong et al. (Zhong et al., 2008) and Ma et al. (Ma et al., 2007) has shown the experimental results that the evolution surface roughness with thickness is dependent on the surface morphology of the silicon substrate at the beginning of the DLC growth. For a smooth substrate, the DLC film surface becomes smoother as the thickness increases due to the preferential growth of the valley on a smooth substrate. For a rather rough substrate, on the other hand, the surface roughness of the film decreases at the beginning, then increases with thickness up reaching the maximum value before decreases. The concept of island growth and a growth model was proposed to explain the observation. The favored growth at the valley was thought to be responsible for the initial island nucleation.

The initial smoothing approach is depicted in Figures 2.20(a) and 2.20(b). In the schematic representation, incident ions prefer to stay in the valley, which leads to a decrease in surface roughness. When the surface becomes smooth, valley growth does not dominate film growth because the peak-to-valley distance is not large enough to produce an adequate energy barrier. Simultaneously, the island nucleus is created as a result of the early smoothness stage aggregation of mobile carbon atoms in the valley. C-C bonds are favored over C-Si bonds because the bonding energy of C-C (610.2 kJ/mol) is greater than that of C-Si (451.5 kJ/mol). As a result, the nucleus grows larger, and the film exhibits island growth. As a result, the DLC film grows in an island mode on the substrate, as illustrated in Figures 2.20(b) and 2.20(c). Therefore, when the island grows larger and the peak-to-valley distance increases, the growth enters the next roughening stage. The islands gradually consolidate because of their expansion. In the final smoothing stage of the growth, as illustrated in Figure 2.20(d), the surface roughness diminishes, and the surface becomes smoother.

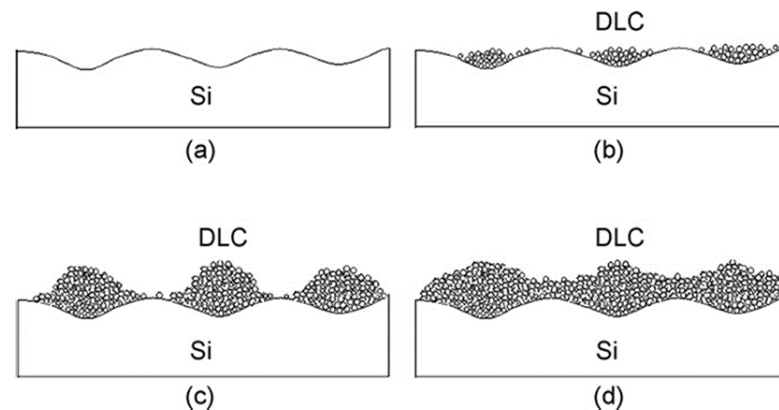


Figure 2.20 Proposed growth mechanism for a DLC film on a rough silicon substrate (a) Si substrate, (b) initial smoothing stage: island nucleation generated by the favored growth of valley, (c) roughening stage: island expansion, and (d) ultimate smoothing stage: island coalescence. Reprint (Zhong et al., 2008).

2.8 Tribology of DLC films

In Greek, tribology means "to rub." Some define it as an intriguing surface in motion, while others define it as all actions related to it. It is the study of the processes of friction, lubrication, and wear of contacting surfaces in relative motion. Reduction of friction and wear extends the lifetime of numerous technical applications such as automobiles, airplanes, and biomedical devices (Bewilogua et al., 2014; Johnston et al., 2005). DLC films and coatings have been widely applied as protective layers against friction and wear and their tribological properties have been extensively studied (Jeon et al., 2007; Liu, Erdemir et al., 1996a, 1996b; Liu et al., 1997). The tribological properties of DLC films are highly influenced by the deposition process and tribotesting conditions such as substrate, contact pressure, speed, temperature and environments.

2.8.1 Applications of interlayer or adhesive layers

It has been previously shown that addition of an interlayer between a DLC film and substrate can lower internal stress (Wei and Yen, 2007), improve adhesion (Bootkul et al., 2014; Cemin et al., 2015), regulate crystal growth (Huang et al., 2007), and enhance the atomic diffusion energy barrier during the deposition process (Li et al., 2010). Typically, the inter layer is placed between the substrate surface and DLC

film. The interaction of atoms and molecules at the interface of two surfaces provides the adhesion between the substrate and DLC film. The interfacial bonding strength significantly affects the adhesion. The ideal interlayer material also provides an outstanding diffusion barrier between carbon and the substrate and promote diamond nucleation and interfacial bonding (Li et al., 2010). A variety of interlayer materials, including ceramics and metals (Ti, Zr, W, Nb, Si, Cr, or WC) (Huang et al., 2007; Jeon et al., 2007; Liu et al., 2013; Rismani et al., 2012), have been investigated as an interlayer. Endler et al. (Endler et al., 1996) investigated the stress and adhesion of amorphous ceramic interlayers, including a-SiC, a-Si₃N₄, and a-SiC_xN_y. It has been established that the amorphous ceramics are suitable interlayer materials for CVD diamond films on cemented carbide substrates. Chen and Lin (Chen and Lin, 2009) applied the nitrogen layers to the steel substrate before depositing the DLC films. It was observed that if the DLC film is sufficiently thick on the substrate, the adhesion of the DLC film to the substrate is greatly improved, and the wear resistance of the DLC film is increased. Liu et al. (Liu et al., 2013) investigated the effect of Si interlayer thickness on the ultrathin *ta*-C film's structure. The Si film had a thickness of between 0.5 and 3.0 nm, whereas the *ta*-C layer had a thickness of approximately 2 nm. They discovered that a portion of the Si bonding was converted to SiC bonding, which improved the adhesion of *ta*-C to metal. In order to better understand how adhesion affects the structure of DLC films, Liu et al. (Liu et al., 2013) investigated the effect of Si film thickness on the ultrathin *ta*-C films structure. The Si film has a thickness of between 0.5 and 3.0 nm, whereas the *ta*-C layer has a thickness of about 2 nm. They discovered that a portion of the Si bonding is converted to SiC bonding, which improves the adhesion of *ta*-C to metal.

It was discovered by Chen et al. (Chen et al., 2019) that the interlayer thickness has an effect on the tribology of DLC films. Figure 2.22 shows that the friction coefficient of DLC films varies with the thickness of SiN_x interlayer. The tribological properties of the DLC films with interlayer thicknesses of 8 nm and 20 nm were found to be the best, while those of DLC films with interlayer thicknesses of 12 nm and 16 nm were found to be the worst. The DLC film without the SiN_x interlayer showed a

significant reduction in performance, corresponding to the critical load applied to the sample during testing.

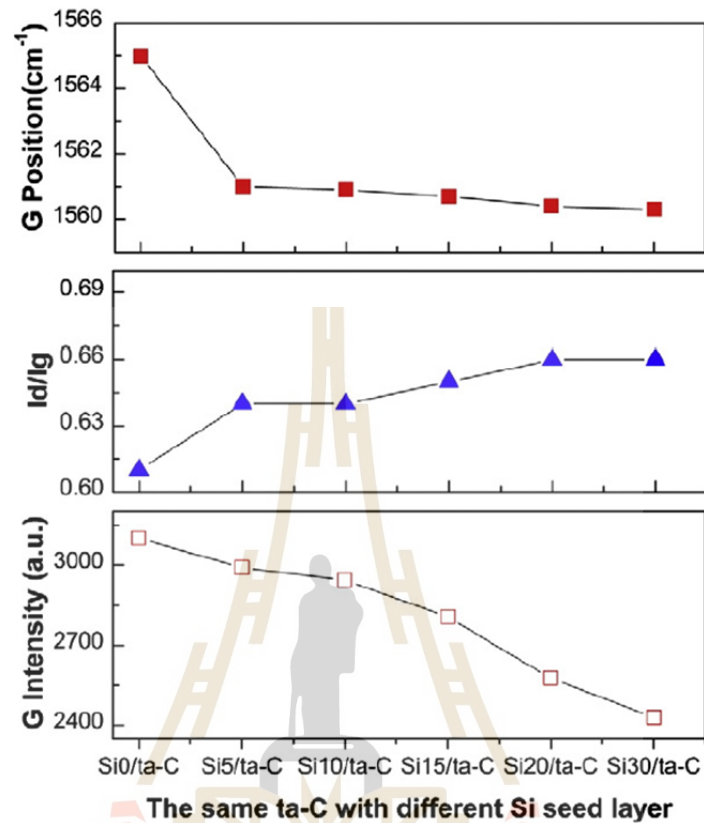


Figure 2.21 Variation of G position, I_D/I_G , and G intensity with the Si seed layer thickness varying from 0 to 30 Å. Reprinted (Liu et al., 2013).

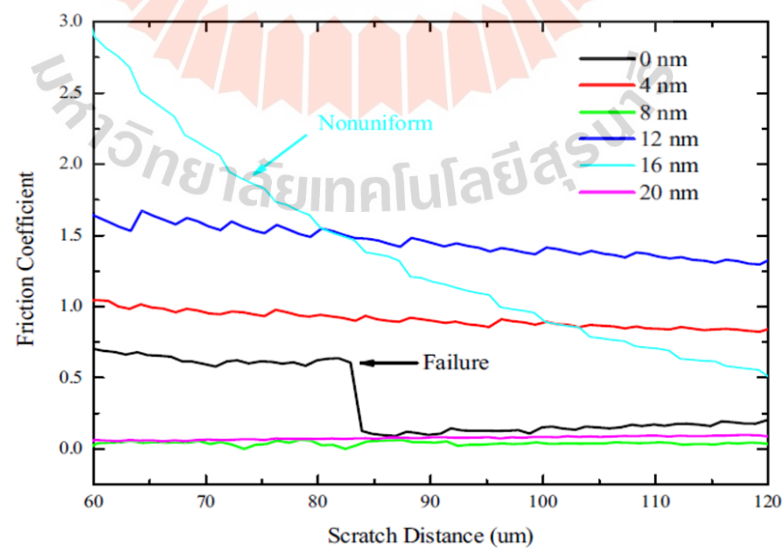


Figure 2.22 The friction coefficient of the DLC films with various SiN_x interlayer thicknesses. In the measurement, the tip was translated with a consistent load to allow the penetration into the film.

2.8.2 Influence of the Environment on DLC Film Tribology

The tribological performances of DLC films are greatly influenced by environment, such as gas atmosphere, humidity, and temperature. Figure 2.23 shows the influence of relative humidity on the coefficient of friction of hydrogen-free, hydrogenated, and DLC films with varied hydrogen concentrations. In dry and inert environments, the hydrogenated DLC films exhibit a low friction performance due to weak van der Waals forces acting between surfaces in the test, while hydrogen-free DLC films have high friction and wear. However, in humid oxygen-containing environments, water vapor molecules influence the process, creating a tenfold increase in friction.

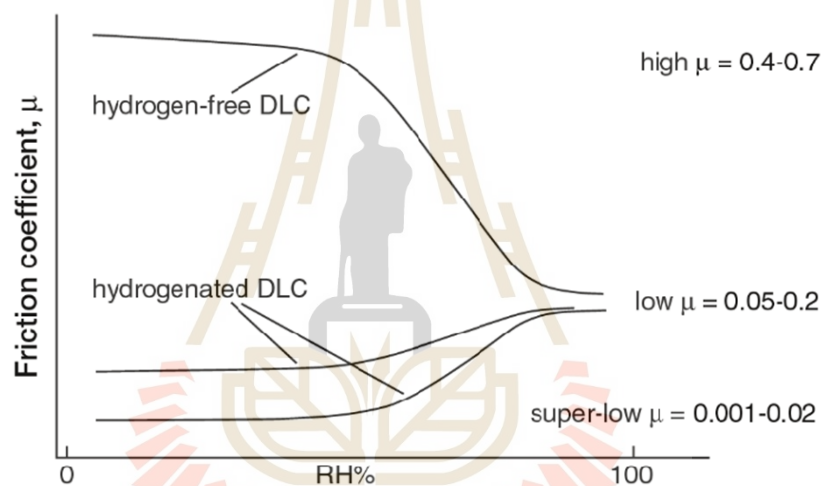


Figure 2.23 The influence of relative humidity on the coefficient of friction of hydrogen-free, hydrogenated, and DLC films with varied hydrogen concentrations. Reprinted (Ronkainen and Holmberg, 2008).

The friction of hydrogen-free films reduces (<0.15). The friction of hydrogenated films, on the other hand, rises with increasing humidity (Gangopadhyay and Tamor, 1993). Grill et al. (Erdemir et al., 2000) discovered that the wear resistance of DLC films strongly depends on the deposition technique. The friction coefficients can be extremely low (as low as 0.01 or less) or extremely high (>0.5) in inert conditions, such as dry nitrogen and vacuum (Erdemir et al., 2000). It has been demonstrated that the hydrogen content of the films can influence the binary friction behavior during tribological experiments conducted in ultra-high vacuum (UHV). High friction is caused by hydrogen concentrations of less than 34%. In contrast, ultralow friction is attained with sheets containing at least 40% of H. While DLC film wear rates

are typically in the 10^{-6} to 10^{-10} $\text{mm}^3 (\text{Nm})^{-1}$ range, and wear resistance varies depending on the structural properties of the DLC films. The environment can influence wear behavior because of a correlation between friction and wear. In general, high friction is associated with high wear, as seen for hydrogen-free films in an inert gas or under vacuum in Table 2.7 (Donnet and Erdemir, 2007), because wear rates drop as the friction coefficient decreases.



Table 2.2 The Coefficient of friction values and the wear rate of the hydrogen-free DLC coating testing different environment (Donnet and Erdemir, 2007)

DLC Film		Tribological testing					
Film (substrate)	Deposition technique	Counter material	Load(N)/(Gpa)	Speed (ms ⁻¹)	Environment	Friction	Wear rate (x10 ⁻⁶ mm ³ (Nm) ⁻¹)
<i>ta</i> -C (WC-Co)	Ion beam deposition	Steel Si ₃ N ₄	0.95 GPa 1.23GPa	0.13	Ambient air	0.13 0.06	-
<i>ta</i> -C (Tool steel)	Vacuum arc discharge	AISI52100	0.86 GPa	0.1	Ambient air (40% RH)	0.12-0.22	0.07
<i>ta</i> -C (Steel)	Vacuum arc discharge	<i>ta</i> -C (Steel)	10-80N	6.0	Ambient air (10 ⁵ Pa) Vacuum (10 ⁻⁵ Pa)	0.04-0.13 0.6	-
<i>ta</i> -C (Si)	Pulsed arc discharge	Si ₃ N ₄	1.54N	0.1	Ambient air (72% RH)	0.07	0.15
<i>ta</i> -C (Si)	Pulsed arc discharge	AISI52100 M50 Al ₂ O ₃	5-20N 10N,5N	0.1	Ambient air (50% RH)	0.26-0.17 0.22 0.21	<0.01 <0.01 0.06

Table 2.2 (Continued) The Coefficient of friction values and the wear rate of the hydrogen-free DLC coating testing different environment (Donnet and Erdemir, 2007)

DLC Film		Tribological testing					
Film (substrate)	Deposition technique	Counter material	Load(N)/(Gpa)	Speed (ms ⁻¹)	Environment	Friction	Wear rate (x10 ⁻⁶ mm ³ (Nm) ⁻¹)
<i>ta</i> -C (Si)	Pulsed arc discharge	AISI52100 Al ₂ O ₃	10N	0.100	Amb. Air (10%RH)	0.260	0.007
			5N		Amb. Air (20%RH)	0.400	0.008
					Amb. Air (50%RH)	0.170/0.190	0.007/0.040
					Amb. Air (70%RH)	0.200	0.010/0.090
<i>ta</i> -C (AISI 440B)	Pulsed arc discharge	AISI 52100	5-35N	0.100-3.000	Ambient air (50% RH)	0.140-0.190	0.030-0.160

2.8.3 Physical and mechanical interactions

On rough surfaces, friction and wear are severe problems. When the sliding surfaces are rough, asperities that are mechanically linked together cause significant friction losses (especially during the run-in or initial stages of sliding tests). The surface roughness increases friction and wear losses. The DLC coatings have significantly higher friction coefficients when applied to a rough or lapped surface, as described in Figure 2.24 (Erdemir and Donnet, 2006). When DLC films are smoother, they are less susceptible to abrasion (provided that other test parameters are kept the same). The surface roughness of the DLC films is strongly influenced by that of the substrate. Typically, the surface of DLC films nearly match the substrate due to the amorphous nature. When DLC films are applied to highly polished surfaces (such as silicon wafers), they are exceptionally smooth, but when coated on rough ground surfaces, they are quite rough. The surface also depends on the deposition process. PLD or arc PVD techniques can result in the expulsion of large numbers of nano/microparticles and/or droplets from solid carbon sources. This increased in friction and wear caused by microparticles on sliding surfaces.

Jiang et al. studied the effect of substrate surface roughness of DLC films deposited on M42 tool steel substrate with composite interlayers. The study was performed on a ball-on-disk wear rig in dry air. After deposition, the coating's surface roughness was around half that of the substrate. While the frictional behavior was unaffected, the coating wear rate rose dramatically with substrate surface roughness. The wear rate rose fast when R_a 0.93 μm was reached. From adhesion to chip/flake production and coating fragmentation as the substrate roughness increased. Coatings started chipping/flaking at the tops of asperities in the surface roughness. For coatings on rough substrate surfaces, the Archard specific wear rate rose with total load, but was practically invariant for coatings on smoother substrate surfaces, nominally following Archard's wear law. The elastic foundation model of contact mechanics was used to examine contact pressure distributions between the ball and rough coating surfaces. The contact forces grow dramatically with coating surface roughness. Coatings placed on uneven substrate surfaces exceeding R_a 0.93 μm are prone to plastic yielding. The apparent effect of surface roughness on DLC coating wear and wear

mechanism transitions can be explained by the contact mechanics study results (Jiang and Arnell, 2000).

Varanasi et al. investigated the friction and wear behavior of DLC overcoated head magnetic recording as a function of DLC overcoat thickness using contact-start-stop and constant speed drag tests. The Raman spectra obtained from various locations on the air-bearing surface were studied before and after wearing tests to reveal the relationship between the D and G band regions and the DLC film thickness. The Raman spectra of DLC coated sliders before and after wear testing was utilized to investigate non-uniformity in DLC film wear rates over the air bearing surface. In comparison to uncoated slider-disk interfaces, the DLC coated slider-disk interfaces have shown significant increases in frictional performance.

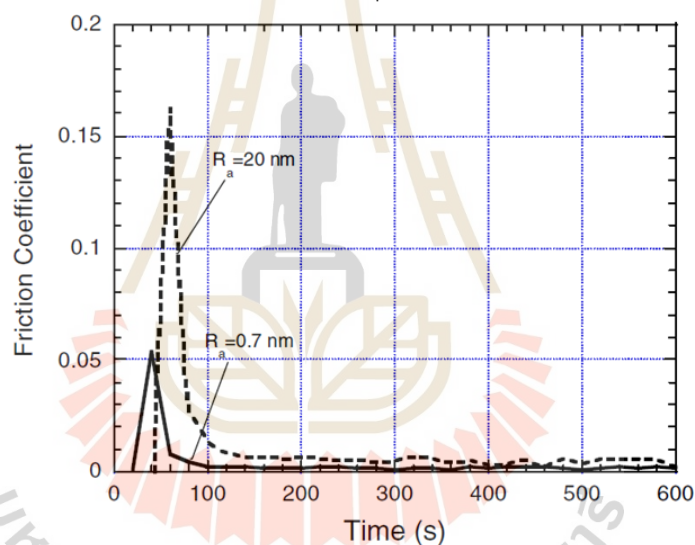


Figure 2.24 Surface roughness influences initial and steady-state DLC film friction coefficients. Reprinted from (Erdemir and Donnet, 2006).

2.9 Application of DLC

2.9.1 Magnetic recording industry

In hard disk industry, the surface of the magnetic medium (Co-Cr-Pt alloy) and the slider read-write elements are usually deposited with a thin protective layer with a thickness as low as sub-nanometers. This overcoat layer can protect the magnetic surface from corrosion, and we are (Robertson, 2003; Yeo, 2017). This application requires the protective layer which can completely cover the surface

without any defects or pinholes. The overcoat material should be lubricant friendly and provide good adhesion sites for lubricant molecules. It should be as smooth as possible and exceedingly hard, durable, and has a low coefficient of friction to preserve the surface from wear. For decades, DLC films have fulfilled the requirements as a protective coating for the magnetic layers in hard disk drives due to their unique characteristics. The slider's read-write elements (magnetic sensor and poles) are constructed of mechanically soft magnetic materials that wear more quickly than the surrounding hard Al_2O_3 dielectric insulator. Pole tip recession (PTR) is a type of magnetic pole recession that causes the gap between the active parts of the head and the media to increase. By coating the head with an ultrathin hard DLC film, PTR can be rectified. Head overcoats are important not only to protect the head elements from wear and corrosion, but also to act as a barrier against lubricant deterioration. Uncoated $\text{Al}_2\text{O}_3/\text{TiC}$ sliders could cause PFPE molecules to break down quickly. PFPE breakdown and fluorine emission can occur due to frictional forces. This reaction is possible because fluorine can interact with a-C: H films and produce HF and CF_2O (Baker Jr and Kasprzak, 1993; Kasai, 1992). The Lewis acid AlF_3 is formed when HF and CF_2O react with aluminum oxide in the slider (able to accept electron pair from other atoms or molecules). FPE lubricant molecules can be rapidly decomposed by Lewis's acid catalytic reactions on AlF_3 surface. Sliders that are coated with DLC films could be used to prevent lubricant molecules from interfering with Al_2O_3 phase of AlTiC or dielectric of head from reacting. DLC coating also significantly reduces the lubricant's breakdown rate due of its low friction (Bhatia et al., 1999; Chen et al., 2000).

This application also relies on scratch resistance at the nanoscale scale, which is another crucial attribute of the films. Using a different deposition approach, the interaction between Raman G-peak dispersion and the relative scratch resistance of magnetron sputtered and FCVA a-C: N films (Vetter, 2014) is seen in Figure 2.25.

In order to determine scratch resistance, a diamond tip was used in conjunction with an AFM, which is a common technology in the hard disk industry because it can provide resolution as low as 0.1 nm. When a-C: N films are deposited by FCVA, the scratch resistance is approximately 5 times more than when magnetron sputtered coatings are applied. However, because of the exceedingly thin coating

thickness, it is difficult to understand how the film functions as a wear reduction film against the abrasive impacts of the slider of the head during operation. The FCVA approach deposits an ultra-thin hydrogen-free film with a thickness of less than 5 nm, which is yet continuous, dense, and hard enough to be employed as a potential option for the tribology of the next generation of hard disks, among the many various types of DLC films (Matlak and Komvopoulos, 2018; Zhang and Komvopoulos, 2009a).

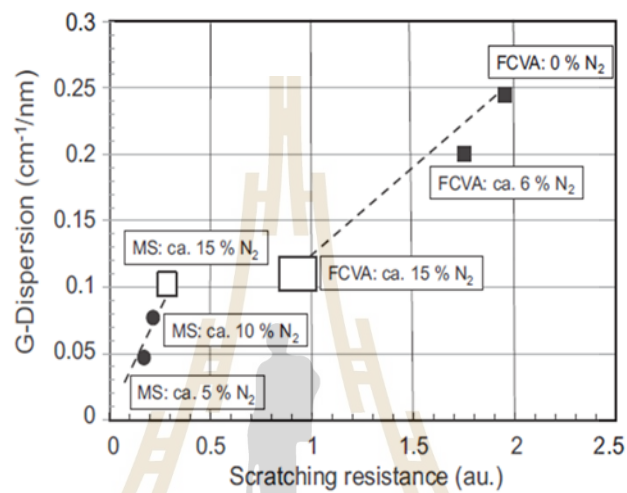


Figure 2.25 The relationship between the dispersion of the G peak and the scratch resistance of an a-C: N film is grown using magnetron sputtering and FCVA (Vetter, 2014).

2.9.2 Automotive parts

Since the 1990s, high-end racing engines have started employing DLC with various types of coatings. The increased wear resistance and reduced friction losses were achieved on the basis of DLC coating's superior tribological capabilities. When sliding begins in a mixed friction situation, DLC possesses the capability the tribo-system by preventing adhesive and abrasive wear. Since the end of the 1990s, a-C:H: Me has been applied to a number of automobile parts utilizing a hybrid PACVD-sputtering method. In the beginning, Volkswagen's diesel injection system was the first item on the market. DLC films are now applied on high-pressure pumps, piston pins, piston rings, tappets, piston skirts, finger followers, valve shafts (Kano, 2006; Kennedy et al., 2014; Treutler, 2005; Vetter, 2014). Figure 2.26 illustrates a few examples of these samples (Vetter, 2014). Reduced CO₂ emissions became a growing concern in engine engineering at the beginning of the 2000s and are currently a major driving force for

the mass manufacturing of DL. Additionally, it's important to look at the friction behavior (Erdemir and Donnet, 2006; Sánchez-López et al., 2008).

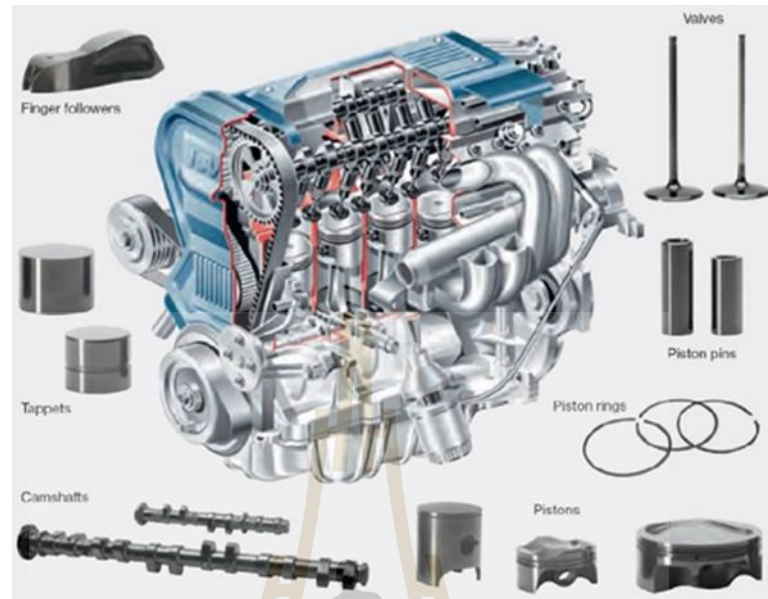


Figure 2.26 Selected engine parts coated by diamond-like carbon (DLC) (Vetter, 2014).

CHAPTER III

EXPERIMENTAL PROCEDURE

This chapter covers the experimental approaches for fabrications and characterization of the ultrathin DLC films in this research. Materials used in the film depositions and preparation are also detailed.

3.1 Sample preparation and procedure experiments

In this thesis, the *ta*-C films with adhesive layer have been successfully fabricated using a PFCVA system. The experiments set-up, materials used, and two experiment procedures are described in detail below.

3.1.1 Materials

- i. Silicon nitride (SiN_x) target with 99.999% purity.
- ii. Silicon (Si) target with 99.999% purity.
- iii. Graphite (Carbon) target with 99.999% purity.
- iv. 2-inch Nickle Ferrite (Ni:80 at%, Fe:20 at%) substrates.
- v. Argon (Ar) gas with 99.999% purity used as etching and sputtering.

3.1.2 Experiment Procedures

This thesis studies two main interesting topics on the application of ultrathin *ta*-C films for HDD:

- i. Dependence of structure on thickness of ultra-thin *ta*-C film.
- ii. Influence of interlayer materials and their thickness on the structure of ultra-thin *ta*-C films.

3.1.2.1 Dependence of structure on thickness of ultra-thin *ta*-C film

The *ta*-C films deposition overcoat encompassing two sets of experiments with a 0.5 nm Si-interlayer as an interlayer layer, and various 0.5-5.0 nm carbon thickness was proposed as a novel protective overcoat layer, electronic structure, and tribological properties. The experiment procedure schematic for sample preparation is illustrated in Figure 3.1.

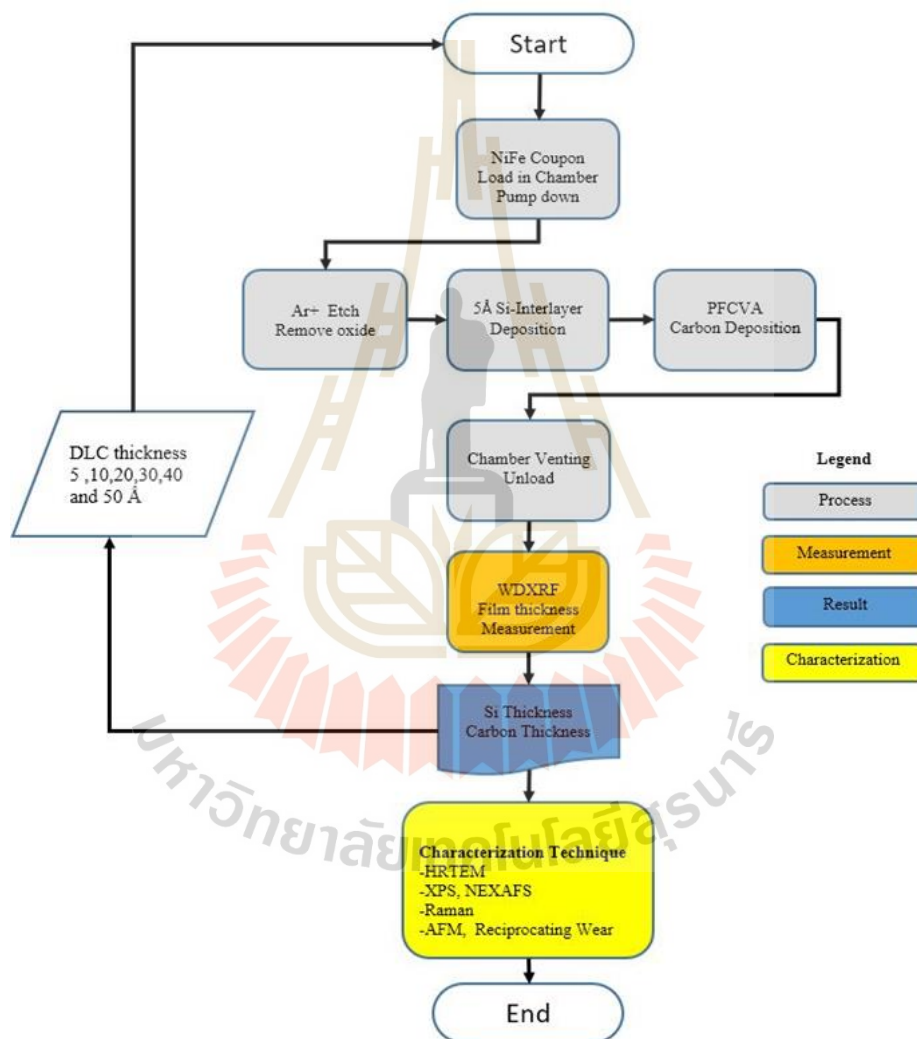


Figure 3.1 DLC film deposition and characterization experiment methodology flow chart.

3.1.2.2 Influence of interlayer materials and thicknesses on the structure of ultra-thin *ta*-C films

The varied interlayer thicknesses of Si and SiN_x used in the carbon overcoat consist of a bi-layer with an interlayer thickness of 0.0-1.0 nm and a protective overcoat layer of 1.0 nm thick *ta*-C constant. The deposited state is consistent across all samples. Figure 3.2 illustrates the experiment method design for sample preparation.

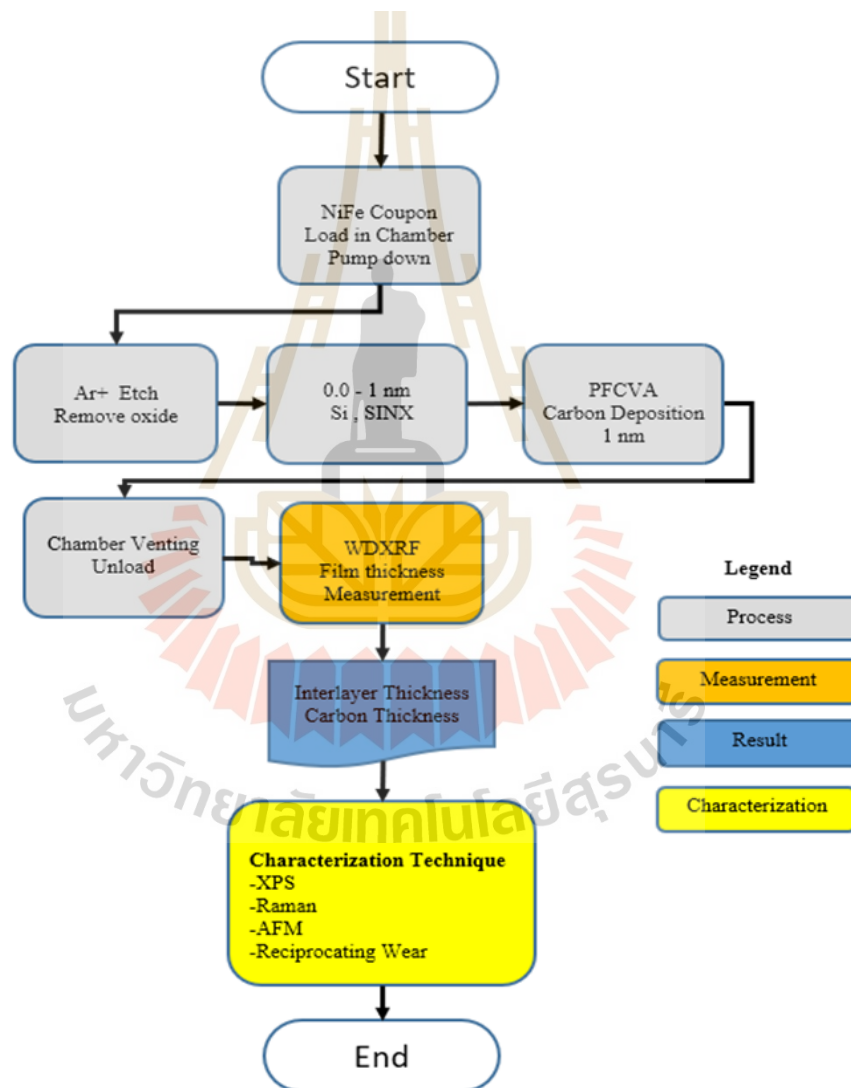


Figure 3.2 DLC film deposition and characterization experiment methodology flow chart.

All of the samples were subjected to a series of tests, which included HRTEM, WDXRF, AFM, and a reciprocating slide wear tester, in order to ascertain the thickness of the ultra-thin *ta*-C and interlayer overcoats, as well as the surface roughness and tribological properties of each of the individual samples. In addition, the author utilized Raman spectroscopy, XPS, and NEXAFS in order to conduct an investigation into the microstructure and bonding environment of carbon-based overcoats that was more in-depth than what had been described previously.

3.2 Fabrications of ultrathin *ta*-C films

The majority of film deposition techniques, including various physical vapor deposition and sputtering techniques, are incapable of fabricating continuous overcoat films with thicknesses of less than 5 nm (Matlak and Komvopoulos, 2018; Robertson, 2001). However, FCVA is the only low-temperature technique that can produce continuous and ultrathin *ta*-C films with remarkable nanomechanical and tribological properties, such as high hardness and wear resistance (C. Casiraghi et al., 2004; Zhang and Komvopoulos, 2009a).

3.2.1 Deposition setup

In this thesis, the deposition of ultrathin *ta*-C films was accomplished using a commercially available, custom-designed, and assembled NEXUS DLC-X system from Veeco company Inc. The system includes an RF ion source, ion beam deposition, and pulsed filtered cathodic arcs (pFCVA) (Veeco Instruments Inc, 2012).

As depicted in Figure 3.3 The system consists of two load lock chambers, A and B, transfer module chamber, pre-clean chamber, and chamber for pFCVA. An isolation gate valve connects all chambers. Each chamber is equipped with a molecular turbopump used to pump the chamber independently. The pressure of all five chambers was monitored using the Pirani and ionization gauges. All chambers have a low base pressure of 5×10^{-7} torr. The transfer module chamber was equipped with an automated robot arm system used to transport the substrate from the load lock chamber to the pre-clean and pFCVA chambers during the deposition process.

The load lock chamber was used to manually load substrates into the machine (during the load lock chamber was under atmospheric pressure). A mechanical and a molecular turbopump were then used to evacuate the load lock chamber. Following a pressure drop in the load lock chamber to a low pressure of 5.0×10^{-5} torr, the isolation gate valve that separates the transfer chamber from the load lock chamber is opened. Next, the substrate will be picked up and transferred to the substrate fixture in the pre-clean chamber using the robot arm.

The pre-clean chamber is fitted with a 16.5-inch-diameter RF ion source. The RF ion source is utilized to clean the substrate's top surface, removing any ambient oxidation. The robot arm subsequently transports the clean substrate to the substrate fixture in the pFCVA chamber without disrupting the vacuum. The PFCVA chamber has an 8.3-inch diameter ion beam source for adhesion layer deposition and a pFCVA for DLC film deposition. The substrate fixture in the pre-clean and PFCVA chambers can tilt and rotate during the operation. As a result, the adhesion layer and DLC film may be deposited onto the substrate at any incidence angle required, while fixture rotation is used to improve uniformity.

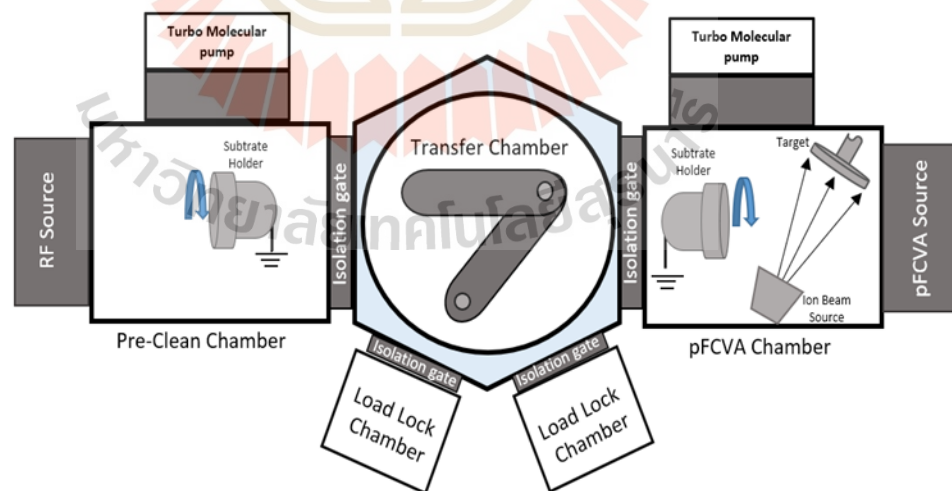


Figure 3.3 Illustrates the Pulse filtered cathodic vacuum arc (PFCVA) deposition system (Veeco Instruments Inc, 2012).

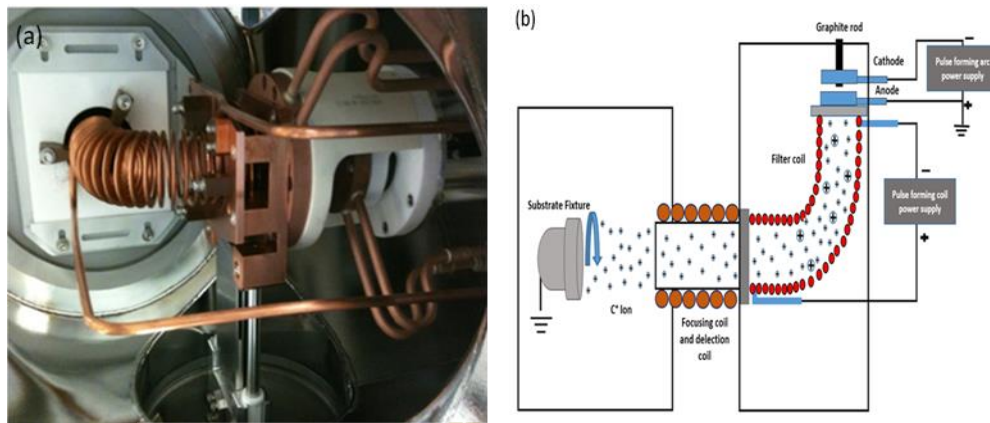


Figure 3.4 PFCVA chamber and cathodic arc source, (a) Assembly cathodic arc source, (b) schematic diagram of PFCVA chamber and cathodic arc source.

Figures 3.4(a) and 3.4(b) illustrates the cathodic arc source, which comprises a high purity graphite cathode with a diameter of 0.25 inches and a length of 8 inches. The arc power supply is operated in pulsed mode to reduce power consumption. It is connected to anode and ground in order to provide a positive potential for the power supply. Using a pulse frequency of 1-5 Hz and a voltage between anode and cathode, the arc voltage, which is the voltage between anode and cathode, may be changed between 0-1000 V. The anode-to-graphite cathode distance is around 2 mm, which is sufficient to induce a current discharge between the two electrodes. At the cathode, graphite is vaporized, and the process is repeated. All charged particles are directed in a 90° curve upon entering the filter coil. The electrons are spiraled along a magnetic field created by a filter coil, while the ions are steered due to their charge. A focus coil, which acts as a magnetic lens to focus or defocus the plasma beam, is used to increase the homogeneity of the film thickness distribution. A deflection coil is used to raster the beam prior to it contacting the substrate, and this is shown in Figure 3.4(b). The macroparticles follow an unusual route and exit the filter through gaps between the coil's turns or adhere to the turns. As a result, undesired macroparticles and neutral atoms are filtered out, leaving only pure carbon plasma to cover the substrate.

3.2.2 Deposition process

The deposition of *ta*-C DLC films consists of three steps as schematically shown in Figure 3.5.

i. The NiFe substrate was pre-treated with low-energy Ar^+ ions etch to remove ambient oxidation from the surface. Argon is the standard gas used in this process.

ii. The adhesion or intermediate layer deposition process was performed using an ion-beam sputtering system. As an adhesion material target, an ion beam is aimed at either silicon nitride (SiN_x) or silicon (Si) using an ion beam. With the assistance of the Ar^+ beam, the material was sputtered off the target and deposited on the exposed sample substrates, producing them to glow. The deposition adhesion layer was responsible for forming the chemical bond between the surface substrate and the deposition adhesion layer.

iii. The ultrathin *ta*-C DLC layer was synthesized using a pFCVA technique, which uses a high voltage to form an arc at the graphite source. The arc is well-known for its ability to produce large amounts of energetic carbon-positive ions. Afterward, the carbon ion passed through a series of magnetic coils that acts as a particle filter, removing any undesired macroparticles. Finally, carbon ions plasma was applied directly to the sample for DLC coating.

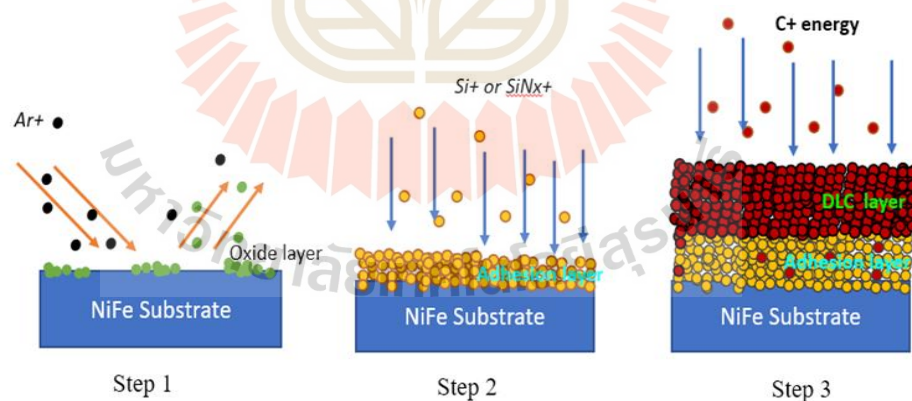


Figure 3.5 Schematic diagram of the pFCVA deposition of ultrathin DLC films with an adhesion layer on the NiFe.

3.3 Characterization techniques

3.3.1 High-Resolution Transmission Electron Microscopy (HRTEM)

One of the most important preliminary characterization methods is the thickness determination of the fabricated ultrathin overcoats. Cross-sectional images obtained from high-resolution transmission electron microscopy (HRTEM) can be used for imaging thin overcoats for the purpose of thickness measurement in this work (≤ 5 nm). In a HRTEM, electrons are generated from a field emission source, and are accelerated toward the sample at a high acceleration voltage (typically a few hundred kilovolts). The electron beam passes via an electromagnetic condenser and a set of objective lenses, which focus and direct the beam to the desired point on the sample. Upon interacting with the sample, the beam is projected onto a charge-coupled device (CCD) camera, which captures and records the resulting image. When an electron interacts with a sample, it is possible to extract several forms of information about the sample, such as its relative atomic composition, crystallographic orientation, lattice defects, and so on. In this study, the HRTEM equipment is used in the bright field mode to determine the cross-sectional thickness of the carbon-based overcoats, rather than in the dark field mode. The sample's higher atomic mass areas scatter electrons further away from the electron beam's normal incidence axis, and fewer of these scattered electrons pass through the sample's aperture.

As a result, these areas have a darker contrast in the image. Therefore, a capping layer of Iridium (Ir), Tungsten (W), or Platinum (Pt), which has a larger atomic mass than carbon, is typically placed to enhance image contrast between the topcoat and other layers.

This research assessed the film thickness using high-resolution transmission electron microscopy (HRTEM, JOEL JEM-ARM200F) at the Vidyasirimedhi Institute of Science and Technology (VISTEC).

3.3.2 X-Ray Fluorescence spectrometry (XRF)

X-ray fluorescence (XRF) spectrometry is a powerful analytical technique that offers both qualitative and quantitative information on the chemical composition. It can be used to determine the chemical composition of a wide variety of materials elements, ranging from beryllium (Be) to uranium (U), in concentration

ranges ranging from 100 weight percent to sub-ppm levels. In addition, XRF can be used to determine the thickness and composition of layers and coatings. This technique is simplicity, non-contact, non-destructive nature, and fast sample preparation. XRF analysis has a wide range of applications in industries (Brouwer, 2006). The XRF spectrometry method makes use of the photon that interacts with the sample under investigation. In the presence of sufficient photon energy in the form of an X-ray, it causes expelled electrons in the element to be displaced, and high orbiting electrons with more incredible energy move to fill the gap produced in the lower orbit (with lower energy), resulting in the emission of photon energy.

Qualitative analysis determines the elements analyte in the sample by measuring the intensity of the sample's emitted radiation and identifying their peak positions. This is referred to as X-ray fluorescence (XRF). Each element has a distinct wavelength determined by the difference in energy between the shell that contains the initial hole and the energy of the electron that fills the hole in the shell. For example, the difference in energy between the K and the L shells is significant. So the elements present in the sample will emit fluorescence X-ray radiation with discrete energy characteristics of these elements as a result of the radiation being emitted. As a result, the height intensity of the peaks was determined from the emitted energies of the sample, which may be used to determine the concentration (count rate) of each element contained in the sample, and vice versa. The intensity of each signal is directly proportional to the thickness of the layer that is being signalized. This process is referred to as quantitative analysis in the industry (Brouwer, 2006; Takahara, 2017; Upmanyu et al., 2021; Van Grieken and Markowicz, 2001).

In XRF spectrometry, the three essential components are a radiation source, a sample, and instrument for measuring the results. One of the most commonly used spectrometers is the energy dispersive (EDXRF) spectrometer, and the other is the wavelength dispersive (WDXRF). This is shown in Figure 3.6, and it is this type of detection that distinguishes the two systems (Brouwer, 2006). Figure 3.6(a) depicts an X-ray tube functioning as an emitter that directly irradiates a sample. Fluorescence radiation emitted by the sample is detected using a dispersive detector that can detect the different energies of fluorescence radiation emitted directly by the sample. Figure 3.6(b) illustrates the energy dispersive X-ray fluorescence (EDXRF)

spectrometer system. The X-ray tube acting as the source directly irradiates the specimen being studied. In this sample, the X-ray fluorescence produced by the sample is monitored using a wavelength dispersive detection device. With the use of analyzing crystals that divide X-rays according to their wavelength or, conversely, their energies, it is possible to identify the unique radiation emitted by individual elements. In order to perform such an analysis, it is either necessary to measure the X-ray intensity at distinct wavelengths one after the other (sequential) or essential to use fixed places and measure the X-ray intensities at different wavelengths all at the same time (simultaneous) (Brouwer, 2006; Van Grieken and Markowicz, 2001).

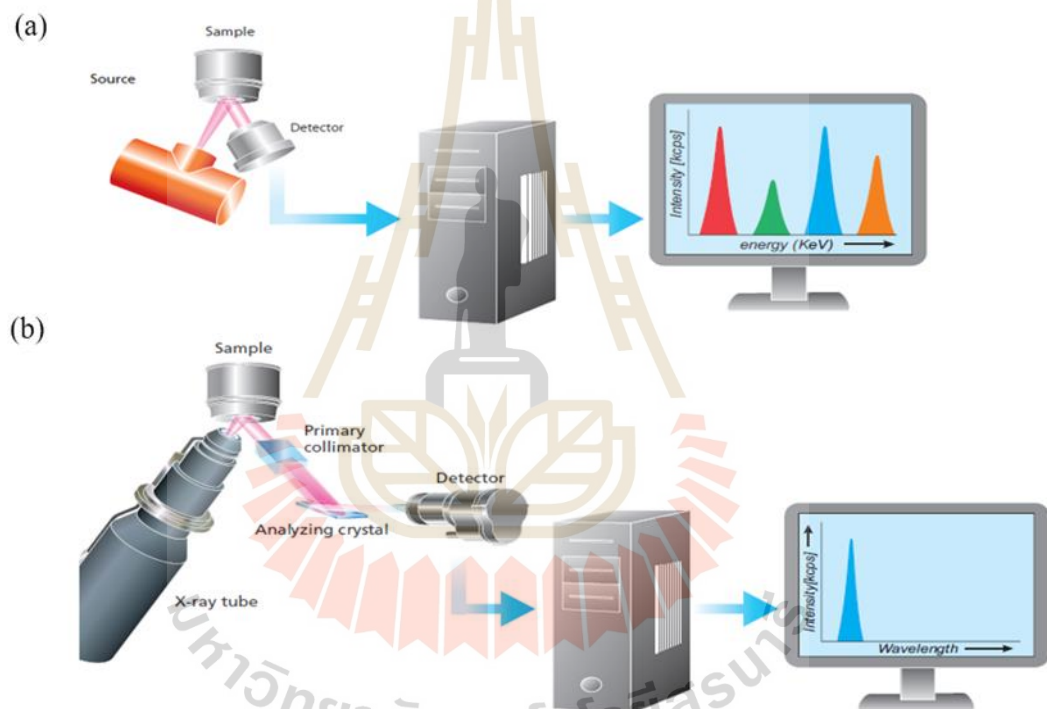


Figure 3.6 Schematic illustration of XRF spectrometry system: Comparison between (a). Energy Dispersive type (EDXRF) and (b) Wavelength Dispersive Type (WDXRF) analysis of the standard synthetic system elements. Reprinted (Brouwer, 2006).

In this work, the DLC film thickness was measured on the 2830ZT (Malvern Panalytical) Wavelength Dispersive X-ray Fluorescence (WDXRF), measurement spot size 10 mm, and SST MAX X-ray source output of 4 kW. The carbon was analyzed and automatically calculated with Fundamental Parameter (FP) modeling, which is fully integrated into the super Q thin-film platform of the 2830ZT.

3.3.3 X-ray Photoelectron Spectroscopy (XPS)

X-ray Photoelectron Spectroscopy (XPS), also known as Electron Spectroscopy for Chemical Examination (ESCA), is the most extensively utilized method for surface characterization due to its ease of use and interpretation. This technique irradiating the sample surface by an X-ray photon with known energy, which causes the photoemission. The generated photoelectrons are ejected from the atom's core and/or valence states. The photoelectron contains a characteristic binding energy (B.E) obtained from the element that emitted it. Chemical states of the surface can be therefore identified via XPS spectra, which are based on the distinct binding energies of the different elements on the surface. The divergence of a peak from a known elemental or core level binding energy is used to distinguish between chemical states that are distinct from one another (chemical shifts), as the diagram in Figure 3.7.

The photoelectric effect is at the foundation of the XPS technique. When an atom absorbs an incident X-ray photon with energy $h\nu$, a photoelectron with a specific KE is released, which is observed using a kinetic energies analyzer and detector positioned at an angle to the surface, known as the take-off angle. The KE depends on the incident photo energy following the relationship:

$$KE = h\nu - BE - \phi \quad 1$$

Where BE is the electron's binding energy ϕ refers to the work function of the spectrometer, which is typically calibrated and known in advance (Hüfner, 2013).

The XPS spectrum is produced by analyzing the intensity and energy of the photoelectron emission. This spectrum shows how the sample is made up of different elements. Additionally, relative amounts of certain elements' binding/oxidation states can be determined (core level spectra) by peak analysis of high-resolution elemental spectra. The vital parts of an XPS spectrometer are a monochromatic X-ray source (Mg $K\alpha$ or Al $K\alpha$), UHV system coupled to the sample chamber, and electron analyzer (most frequently a spherical sector analyzer) equipped with an electron detector. The surface chemical composition of the carbon-based films can be interpreted based on the XPS spectra, and the majority of the mechanical properties of the carbon-based films are directly related to the amount of sp^3 oriented C-C bonds inside the structure of the film (Ferrari et al., 1999; Mabuchi et al., 2013; Pharr et al., 1996; Robertson, 2005).

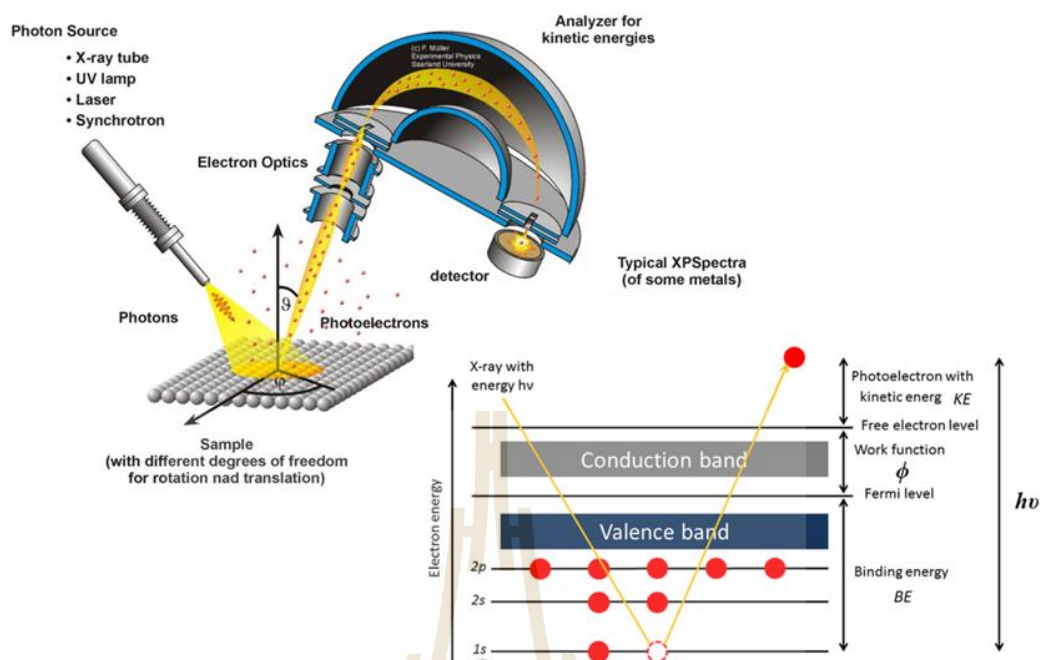


Figure 3.7 Schematic illustration of the basic principle of the XPS technique

In this work, the XPS system (PHI5000 Versa probe, ULVAC-PHI, Japan) employs a monochromatic Al $K\alpha$ X-ray source as an excitation source (1486.6 eV) at the beamline 5.3: SUT-NANOTEC-SLRI XPS, SLRI, Thailand. To prevent beam damage to ultrathin *ta*-C films, therefore, no Ar⁺ ion beam sputter-cleaned was performed on XPS system. The samples were placed in an analysis chamber was evacuated to an ultra-high vacuum (UHV) $\sim 10^{-7}$ Pa. The photoelectrons emitted from the sample were recorded with a spot size of 10 μm , pass energy of 46.95 eV and step increment of 0.05 eV. The quantitative level spectra were carried out using MultiPak Spectrum: ESCA software. The processing of deconvoluted spectra included background subtraction with a "Shirley-Type" integral profile and curve fitting with a mixed Gaussian-Lorentzian function.

3.3.4 Near Edge X-ray Absorption Fine Structure (NEXAFS) spectroscopy

NEXAFS spectroscopy is a type of X-ray absorption spectroscopy (XAS) that can be used to determine the coordination chemistry, local structure, and ligand symmetry around the absorbing atom. It is sensitive to changes in valence state. The most important advantage application of NEXAFS spectroscopy is that it provides unique information on low-Z elements (low atomic number, i.e., carbon, oxygen, nitrogen, and fluorine) (Dienwiebel and Bouchet, 2018; Stöhr, 2013) obtained from the

strong directionality and short length of the covalent bonds between carbon atoms together with the strong dependence of the bond length on its hybridization and the large backscattering intensity of low-energy electrons from carbon atoms. The absorption features in NEXAFS spectra are structure-dependent, and the intensity depends on the orientation of the final state orbital concerning the electric field vector of the impinging X-rays (Dienwiebel and Bouchet, 2018; Mangolini et al., 2021; Mangolini et al., 2016).

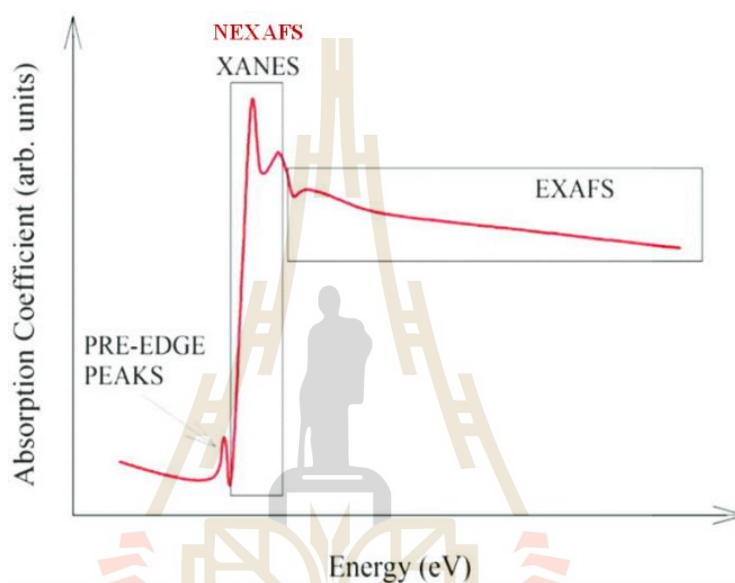


Figure 3.8 Schematic diagram of an X-ray absorption spectrum for the NEXAFS (XANES) and the EXAFS regions (Oguz Er, 2012; Stöhr, 2013)

The schematic diagram of an X-ray absorption spectrum, shown in Figure 3.8, is distinguished into two regions:

- i. the near-edge region: the region within $\sim 30\text{--}50$ eV of the absorption edge is considered the near-edge region, which also contains the pre-edge. The pre-edge area contributes information regarding the investigated system's oxidation state and bonding features, where electrons are excited, but no photons are released. The X-ray absorption near-edge (XANES), often referred to as NEXAFS, is studied in the area where multiple scattering dominates, and inelastic losses are relatively minimal. This X-ray absorption region gives information on the local site symmetry, bond length, bond angles, Fermi charge state, orbital occupancy, and a method to investigate the unoccupied electronic state's angular momentum (Oguz Er et al., 2012; Stöhr, 2013).

ii. the fine structure region: the extended X-ray absorption fine structure region stretched from the near edge region to approximately one thousand eV above the absorption edge. It was dominated by single scattering contributions (EXAFS). The EXAFS can be used to determine the local geometric structure surrounding a specific atomic species. In other words, it is sensitive to the distribution of electron density and, as a result, can be utilized for quantitative investigation of bond length and coordination number (Gurman, 1995; Koningsberger et al., 2000; Koningsberger and Prins, 1988; Stöhr, 2013). Consequently, NEXAFS is a very analytical method that may be utilized to investigate a film's atomic-scale bonding state and electronic structure. Because of its C K-edge, it has the potential to be a sensitive surface that can differentiate between sp^2 hybridization and sp^3 hybridization in amorphous carbon thin films.

The X-ray absorption spectra can be readily obtained in three measurement modes:

(i) transmitted X-ray flux (transmission mode); this method requires thin samples since the penetration depth of X-ray is only a few microns (depending on their energy). This technique is insufficient for evaluating the structural, chemical, and electrical properties of the near-surface areas of materials.

(ii) fluorescence yield (FLY); the fluorescence photons emitted from a bulk sample are measured, and their number is proportional to X-ray photons of the relaxation of the excited atom. The FLY is not discussed in detail here due to its limited surface sensitivity.

(iii) electron yield; this mode refers to as the total electron yield (TEY), Auger yield (AEY), and partial electron yield (PEY). The TEY and PEY modes can be used for amorphous carbon thin films sample as shown in Figure 3.9.

To investigate the bonding configurations, chemical state, and electronic structure of amorphous carbon thin films using the NEXAFS technique, a particular understanding of X-ray absorption cross-section phenomena is important. Figure 3.10 shows a schematic diagram of the origin of NEXAFS features which is a result of incident X-ray photons exciting the core electron to an unoccupied molecular orbital.

Empty molecular orbitals can be labeled according to their symmetry, i.e., π^* or σ^* orbitals, which most are found above the vacuum level. In the case of π -bonded diatomic subunits, the lowest unoccupied molecular orbital (LUMO) is usually a π^* orbital, while σ^* orbitals are generally detected at higher photon energies. The $1s \rightarrow \pi^*$ resonance occurs with the π -bonding both in the form of double and triple bonds, whereas single bonds disregard.

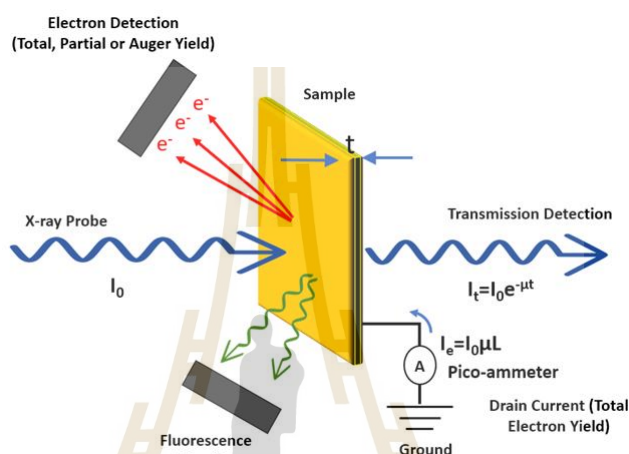


Figure 3.9 Schematic diagram of NEXAFS measurement in electrons yield (total, partial, and Auger) modes and transmission modes modified from Stöhr (1992); Hähner (2006); Watt. et.al.

In comparison, π^* resonances are observed below the ionization threshold because of electron-hole Coulomb interactions (Soin et al., 2012; Stöhr, 2013). The σ^* resonances are asymmetric line-shape at higher photon energies due to the lifetime broadening and molecular vibration along the bond direction, while σ^* spectral features are most often found above the vacuum level for the neutral molecule. In addition, the Rydberg orbitals are detected between the π^* resonance and the ionization potential which can be described as a mixing of the Rydberg orbitals with hydrogen-derived antibonding orbitals, particularly in the C-H bonds.

The transitions only occur when the energy of the incoming X-ray photon matches the energy difference between the core level and the unoccupied molecular level. They are superposed on a step-like absorption edge. The edge energy is related to the oxidation state of the absorbing atom, and the edge position can be recognized on the valence state of the photo absorber (Cramer et al., 1976). The shape

of the edge can also give the information about the chemical environment and ligand geometry, thus providing molecular species fingerprinting (Dienwiebel and Bouchet, 2018; Stöhr, 2013).

In this work, NEXAFS spectroscopy measurements were performed at BL3.2Ub: PEEM (Photoelectron Emission Microscopy), Synchrotron Light Research Institute (Public Organization), Nakhon Ratchasima, Thailand. The synchrotron radiation (SR) acquired from the storage ring has a beam energy of 1.2 GeV. The photon energy of the beamline established a range from 40 to 1040 eV with an energy resolving power $\Delta E/E=10^{-5}$ at 1×10^{10} ph/s and a total energy resolution of approximately 0.5 eV of full width at half maximum (FWHM). The synchrotron radiation was linearly polarized in the sample surface plane at any incident light angle. The undulator was extracted using a varied-line-spacing plane grating of 1200 lines/mm, and samples were irradiated with monochromatic X-rays at an angle of 17° on during the NEXAFS experiment. All NEXAFS spectra measurements of carbon K-edge signal were recorded simultaneously in Auger electron yield (AEY) and total electron yield (TEY) mode. However, only the total electron yield mode (TEY) is presented using via the sample drain current in the photon energy range of 280-320 eV, with a scanning step of 0.1 eV at room temperature and under ultra-high vacuum (UHV) $< 10^{-9}$ mbar.

The absorption signals were first normalized by the ratio emitted electron intensity from *ta*-C sample to that from a freshly cleaned Si wafer that was acquired under the same experimental conditions on the same range photon energy, scanning step, X-rays angle, and same periods time, and then normalized to spectra intensity in the pre-edge region (intensity between photon energy 270 and 280 eV). After pre-edge normalization, the spectra were normalized based on the absorption intensity in the post edge (continuum) region at 330 eV. In this method, variations in spectra intensity only arise from chemical change and are independent of the number density of absorption atoms.

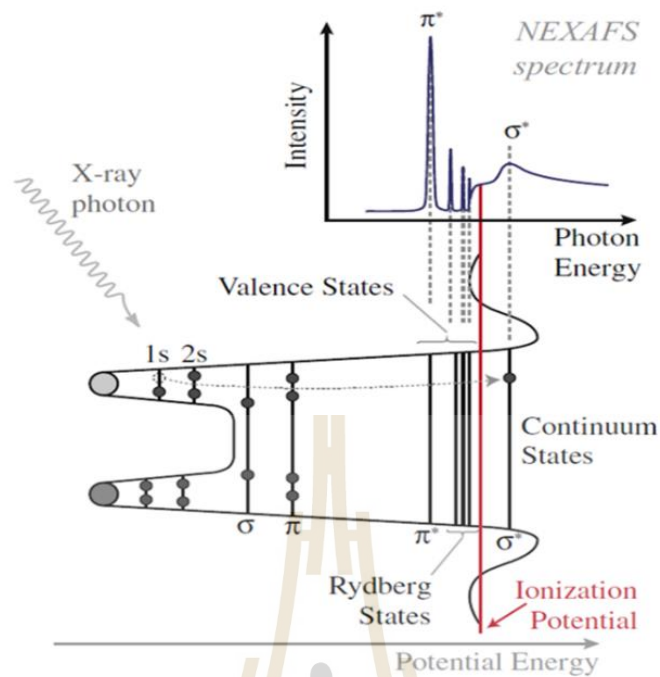


Figure 3.10 The schematic illustrates the absorption of an X-ray photon with the excitation of a core electron to an unoccupied molecular orbital. Reprinted (Dienwiebel et al., 2018).

To evaluate the carbon hybridization state quantitatively from C1s NEXAFS measurement, the relative intensity of the C1s $\rightarrow \pi^*$ and the C1s $\rightarrow \sigma^*$ absorption feature in NEXAFS spectra of the ultrathin *ta*-C carbon material were considered using a NEXAFS spectrum acquired from highly oriented pyrolytic graphite (HOPG) as a reference material (Latham et al., 2017; Mangolini et al., 2016; Stöhr, 2013; Watts, Thomsen et al., 2006). The HOPG has well displayed the electronic structure and almost 100% sp^2 contents and consequently, the sp^2 fraction ratio was estimated using the equation (Dienwiebel et al., 2018; Mangolini et al., 2014; McCann et al., 2005; Roy et al., 2006).

$$sp^2 \text{ fraction} = \frac{I_{sam}^{\pi^*}/I_{sam}(\Delta E)}{I_{ref}^{\pi^*}/I_{ref}(\Delta E)} \quad 2$$

where $I_{sam}^{\pi^*}$ and $I_{ref}^{\pi^*}$ are, respectively, the areas of the C1s $\rightarrow \pi^*$ peaks for the sample and the reference, where $I_{sam}(\Delta E)$ and $I_{ref}(\Delta E)$ are the areas under NEXAFS spectrum between 290.0 eV and 320.0 eV for the sample and the reference, respectively. As a reference for HOPG on 100% sp^2 -bonded carbon, the spectra of the freshly split sample were taken at an incident X-ray beam angle of 170° to the surface of the sample. To calculate and quantify sp^2 content, deconvolute the C K-edge spectra were

using the Igor Pro 6.3 software. All of the NEXAFS results that have been provided in this work are the mean values that have been computed from at least four separate measurements, and the standard deviation that corresponds to each result has also been reported.

3.3.5 Raman spectroscopy

Raman spectroscopy is a nondestructive technique which is widely used to identify the microstructure and study the structural properties of carbon-based materials (Chen et al., 2000; Ferrari, 2002; Ferrari and Robertson, 2000; Ferrari and Robertson, 2001). The basic principle of Raman spectroscopy is derived from the inelastic scattering or Raman scattering of monochromatic light when light interacts with a material. The energy of the incident absorbed photon is different from the energy of the photon released during scattering. In other words, the light's interactions with the atoms or molecules in the materials lead to the shift of the photon energy ($h\nu$), which provides the local structural information about the rotational or vibrational modes of the materials. Figure 3.11(a) illustrates types of light scattering: Rayleigh scattering, Stokes scattering, and anti-Stokes scattering, which are presented in the Raman spectroscopy, were light incident to molecule or atoms. Figure 3.11(b) shows the Jablonski diagram energy transition for Rayleigh and Raman scattering. The Rayleigh scattering initially takes place when the light photon is absorbed, and then elastically, the scattering goes back to the same frequency and level of initial excitation light. The incident photon energy is greater than the scattered photon energy due to the absorption of energy by the material to bring the atoms to an excited vibrational state. This is known as Stokes Raman scattering.

Anti-Stokes Raman scattering typically has a lower incident photon energy than the scattered photon energy, owing to the atoms' net energy release during the transition from the excited to the ground state. Anti-stokes Raman scattering requires an excited state of the atom prior to photon interactions, as illustrated in Figure 3.11(b). This occurrence is far less likely to occur than an atom being in the ground state at the start. As a result, the majority of Raman scattering seen occurs as a result of Stokes Raman scattering. Raman spectroscopy makes use of this effect in conjunction with the material's characteristic resonant vibration modes and frequencies to determine the microstructure. With respect to amorphous carbon, the

excitation energies of sp^1 , sp^2 , and sp^3 bonding are between 0 and 5.5 eV, which corresponds to the energy range of visible to ultraviolet photons.

Typically, the Raman spectra of DLC exhibit conventional characteristics in the wavenumber range of 800-2000 cm^{-1} , with the G and D peaks appearing at 1360–1560 cm^{-1} and the T peak appearing at approximately 1060 cm^{-1} (Gradowski et al., 2003). The G and D peaks in the spectra are two of the most prominent peaks which are created by resonance vibrations of the sp^2 sites of the carbon bonds. As shown in Figure 3.12, the G peak is caused by the bond stretching modes of sp^2 carbon in the ring and chain configurations, whereas the D peak is caused by the breathing modes of sp^2 carbon in the ring configurations (Ferrari and Robertson, 2000; Seigler et al., 2013). T peak can only be clearly observed during higher-energy UV illumination, but the G and D peaks are apparent when using visible wavelength excitation (at a wavelength of around 244 nm).

A phenomenological three-stage model was developed by Ferrari and Robertson (Ferrari, 2004a; Ferrari et al., 2000) to interpret the Raman spectra of amorphous carbon measured for any excitation energy. The Raman spectra fundamentally depend on the following parameter: (a) clustering of the sp^2 phase, (b) bond disorder, (c) presence of sp^2 ring or chain, and the sp^2/sp^3 ratio. The parameters such as the G and D bands positions, the intensity ratio of the D and G bands (I_D/I_G ratio), the full width at half maximum of the G band (FWHM(G)), and cluster size of the sp^2 sites (L_a) can be obtained from the deconvolution of Raman spectrum with Gaussian curves on linear background subtraction. The three-stage model developed by Ferrari and Robertson, generally used to reconcile the above data to the quantity of disorder (amorphization) in the material, the degree of sp^3 clustering, and establishing an estimate for sp^2/sp^3 bonding inside the carbon film.

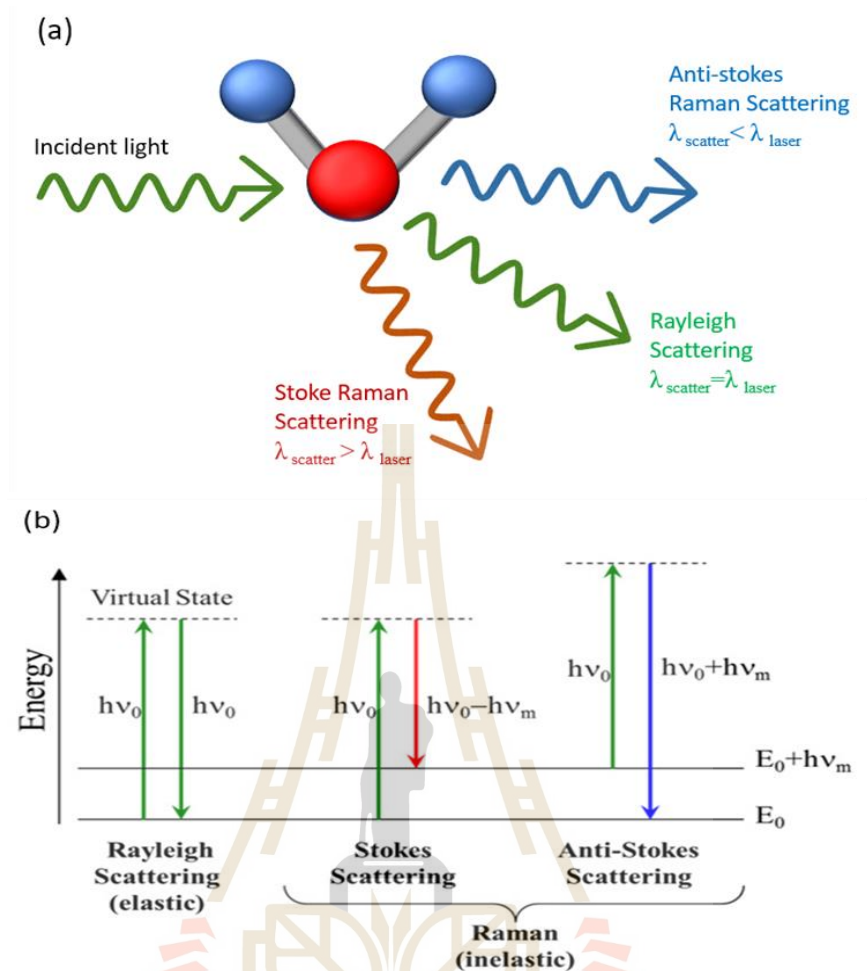


Figure 3.11 (a) Incident light interacts with a vibrating molecule. (b) Jablonski Diagram representing Quantum Energy transitions for Rayleigh and Raman scattering. Reprinted (Chu and Li, 2006; Ferrari and Robertson, 2000; Ismail and Ismail, 2015).

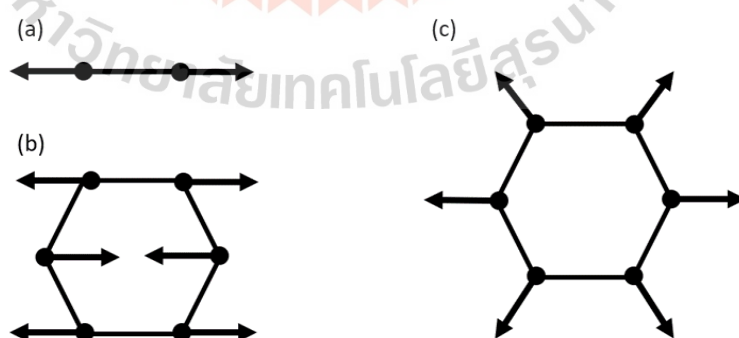


Figure 3.12 Vibration modes in graphitic carbon illustrated the stretching mode for (a) chain configuration, (b) ring configuration and the breathing mode for (c) a ring configuration. Result in (a) and (b) leads to the G peak, and (c) leads to the D peak in the Raman spectrum (Ferrari et al., 2000; Ong et al., 2007).

Raman spectroscopy is used extensively in this research to characterize the microstructure of DLC films. Raman spectra were acquired using visible Raman spectroscopy (Renishaw InVia Reflex Raman spectrometer) at laser wavelengths of 532 nm, 50 mW defocused laser beam output, 100X objective magnification, and spot size $\sim 2 \mu\text{m}$.

3.3.6 Atomic force microscopy (AFM)

AFM is a type of scanning probe microscopy (SPM) with extremely high resolution (Binnig et al., 1986; Giessibl, 2003), in the order of fractions of a nanometer. This technique is based on the intermolecular contact between the sample surface and a sharp tip (AFM tip), which enables to measure the topography and surface forces of conducting and insulating coverings with nanoscale resolution (Carpick and Salmeron, 1997; Garcia and Perez, 2002). Figure 3.13 depicts a schematic representation of the operating principle of AFM (Garcia and Perez, 2002). The AFM tip is attached to a cantilever spring, which deflects in response to the force applied. Depending on the measurement technique, the forces that can be measured with an AFM include Van der Waals forces and capillary forces (in bulk liquids), mechanical contact forces such as lateral forces (LFM) and magnetic forces (MFM), electrostatic forces (EMF), etc. In most cases, silicon or silicon nitride is used as the cantilever material, with a radius of curvature at the tip on the order of nanometers.

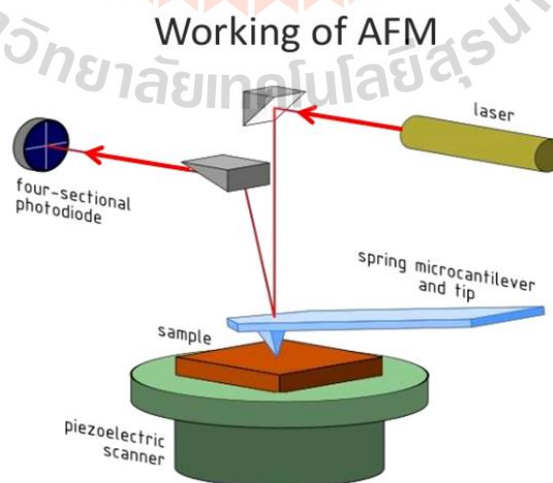


Figure 3.13 Schematic illustration of the principle of AFM. Reprinted (Garcia et al., 2002).

When the tip is in close proximity to the surface of a sample, the force between the tip and the sample causes the cantilever to deflect in accordance with Hook's law. Typically, the deflection is measured using a laser beam that is reflected from the back of the cantilever and detected by a four-quadrant photodetector array. Three different modes of operation are available for AFM, which are: contact mode, non-contact mode, and intermittent contact (tapping) mode. It is possible to reduce tip-sample forces while maintaining good surface topography sensitivity when using non-contact and tapping AFM modes rather than contact modes, which reduces wear and damage between the tip and sample surface. This is an advantage of using non-contact and tapping modes of AFM over contact mode.

In this work, Bruker Innova scanning probe microscope (Bruker, USA) was used to evaluate the surface topography and surface roughness of the samples. The scanning area over which the measurements were made was $1 \times 1 \mu\text{m}^2$ and the contact mode AFM was used. The tip radius of the silicon probe was 8 nm. For each sample, at least four measurements were taken in order to obtain results that were reasonably consistent within the error bars.

3.3.7 Tribological Properties characterization

Typically, tribological properties greatly rely upon the tribo-testing conditions and the film nature. The tested results therefore vary from one place to another. Generally, four main factors that control the tribological properties of DLC are: i) actual working conditions, such as the load, speed, and contacting methods; ii) contacting friction pair, including the film, substrate, and counterpart; iii) contacting microstructure; iv) coating-to-film hardness, film thickness and surface roughness. The factors on the frictional properties depend upon the coating materials and the substrates (Yu et al., 2004)

This work studied the tribological durability properties of the DLC films by using a ball-on-plate universal mechanical tester (UMT, Bruker-UMT Tribo Lab). Figure 3.14 shows a schematic diagram and photographs of the universal mechanical tester (UMT) (Vieira et al., 2020).

The test performs by putting a ball-shaped over the flat sample. The tests were carried out in reciprocating sliding with constant load. The stress is exerted vertically through the ball against the lower flat disc sample, with the ball acting as the spring. The samples slide relative to each other in a linear, back and forth sliding motion under applied load of 50 mN, stroke length of 6mm, sliding frequency of 3.33 Hz, and ambient room temperature.

Test parameters, such as load, oscillation frequency, and test time are controlled using the UMT software. Approximately 10000 cycles are completed in each test, and four tracks are gathered each sample to guarantee repeatability. Each test is run until failure. Continuous friction, normal, and time data collecting were made possible by the software. The coefficient of friction (COF) was determined automatically by the software utilizing data from the normal force and friction force measurements.

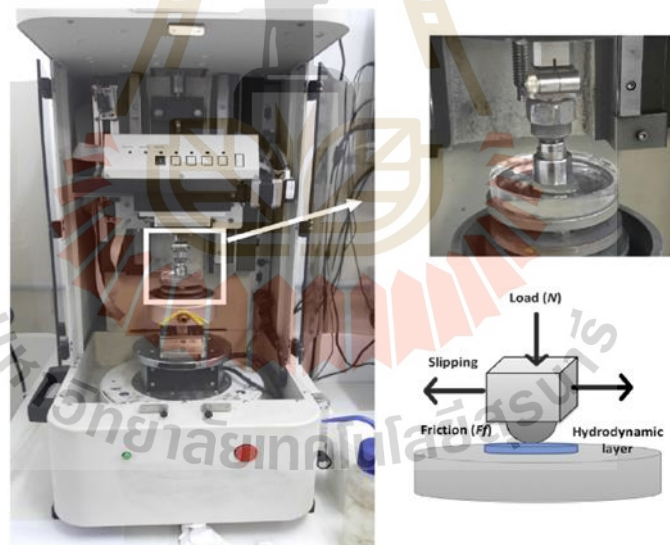


Figure 3.14 Tribometer (UMT-2 Bruker) graphic. Normal load (N) is applied while the surface of the steel ball slides on the DLC film (Vieira et al., 2020).

CHAPTER IV

RESULTS AND DISCUSSION

PART I –Structural dependence on thickness of ultra-thin *ta*-C overcoats

This part presents the study on the structural dependence on thickness of ultra-thin *ta*-C overcoats. The ultrathin *ta*-C overcoats with thicknesses of between 0.5 and 5 nm were deposited on NiFe substrates using pFCVA technique. The NiFe substrates is a commonly used material for a slider pole in the HDD industry. A Si interlayer with a thickness of 0.5 nm was also introduced as an intermediate layer to reduce the internal stress and enhance the adhesive between an overcoat layer and substrate. The thicknesses of the fabricated overcoat were accurately evaluated by using WDXRF and HRTEM. The surface morphology and chemical bonding structure were systematically examined using AFM techniques, XPS, NEXAFS, and Raman spectroscopy techniques. The tribological properties, especially COF, were also analyzed using the reciprocating wear test.

4.1 Overcoat thickness and surface morphology

Figure 4.1 shows the cross-sectional HRTEM images of the ultrathin *ta*-C overcoats with different thicknesses on NiFe substrates. The images demonstrate that the overcoat films were uniform and dense. A transitional zone between the NiFe substrate, capping layers, and deposited layers are clearly distinguishable. However, a region between the Si interlayer and deposited ultrathin *ta*-C films are discernable due to the fact that both Si interlayer and the ultrathin *ta*-C film layers are amorphous, showing the same contrast (Zhong et al., 2009). The WDXRF technique was therefore employed in this study to estimate the thickness of both the Si interlayer and *ta*-C film. The measured thicknesses of deposited Si and ultrathin *ta*-C overcoat by the WDXRF method are presented in comparison with those obtained from the cross-sectional HRTEM images in Table 4.1. It is seen that the total coating thicknesses

determined from both techniques are consistent. The deposited Si interlayer is expected to be approximately 0.5 nm. This validates the accuracy of thickness measurement in this work by the WDXRF technique.

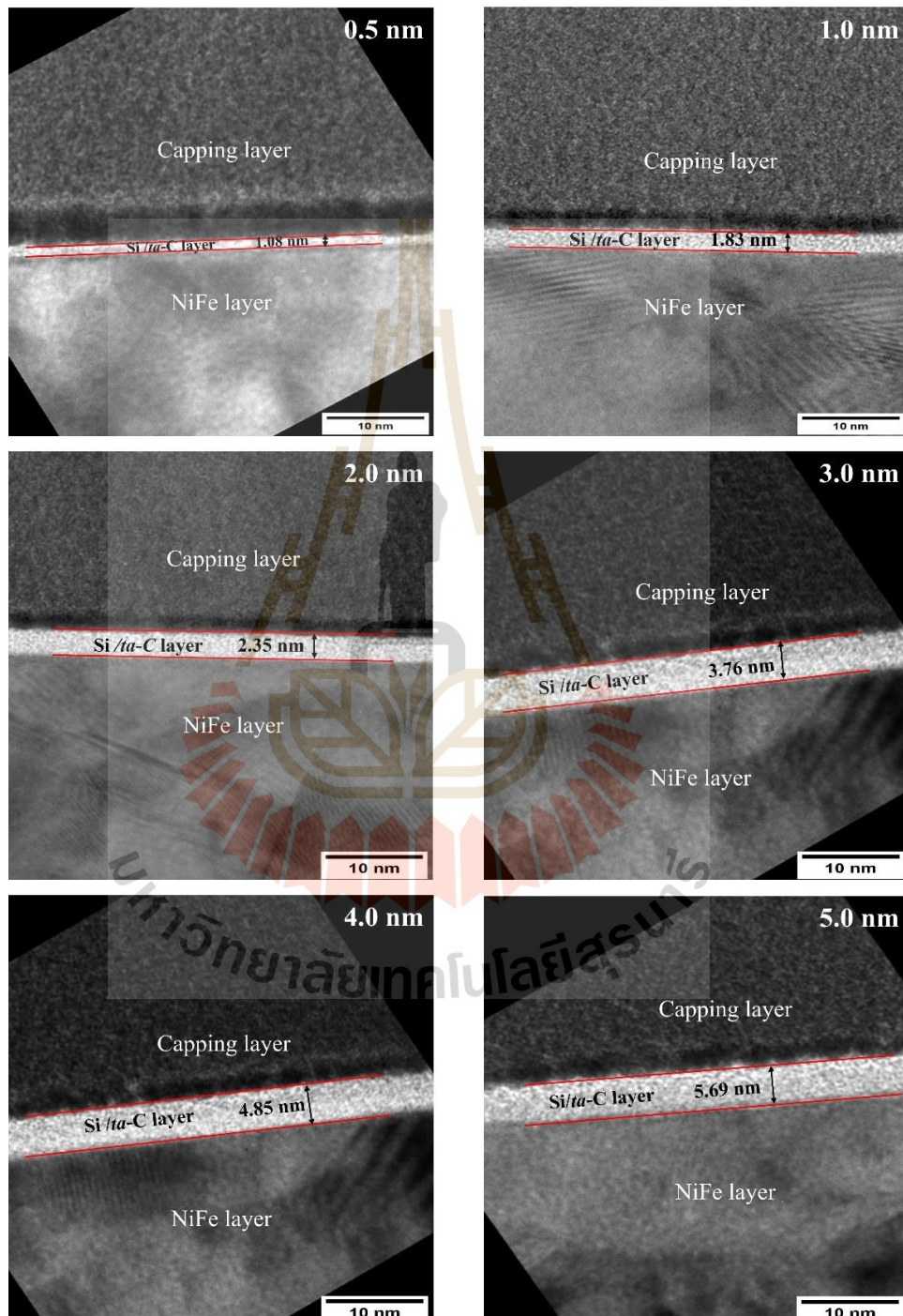


Figure 4.1 Cross-section HRTEM images of the fabricated *ta*-C films with Si interlayers on NiFe substrates. The *ta*-C film thickness was varied between 0.5-5.0 nm.

Table 4.1 Thicknesses of the fabricated *ta*-C overcoats derived from WDXRF spectra and cross-sectional HRTEM images.

Overcoat	Deposition condition Pulse count	Measure thickness (nm)		
		WDXRF		HRTEM
		Si	<i>ta</i> -C	Si/ <i>ta</i> -C
0.5 nm	100	0.51	0.52	1.08
1.0 nm	200	0.51	1.06	1.83
2.0 nm	400	0.49	2.15	2.35
3.0 nm	600	0.47	3.35	3.76
4.0 nm	800	0.54	4.16	4.85
5.0 nm	1000	0.50	5.05	5.69

Figure 4.2 presents the AFM images showing the surface morphologies of NiFe substrate, deposited Si interlayer, and fabricated ultrathin *ta*-C overcoats. The AFM performed in a contact mode over an area of $1 \times 1 \text{ } \mu\text{m}^2$. The results revealed that the surface of fabricated overcoats is smooth and uniform over a large area. The root mean square surface roughness (R_q) was estimated to be in a range of between 0.13 and 0.23 nm.

The measured R_q of the deposited overcoats was plotted as a function of thickness in Figure 4.3. The surface of cleaned NiFe substrate was relatively smooth with R_q of 0.323 nm at the beginning. After the deposition of Si interlayer, the R_q decreased to 0.262 nm. When deposited the *ta*-C films with a thickness of 0.5 nm, the surface become even smoother with R_q of 0.195 nm. The R_q increased to 0.227 nm for the thickness of 1 nm, then gradually decreased and become constant at approximately 0.126 nm for the thickness greater than 2.0 nm.

The results suggest that the evolution of the surface roughness of the ultrathin *ta*-C film was significantly affected by the initial surface topography of the NiFe substrate before deposition. The surface of the ultrathin *ta*-C film becomes smoother

during film growth and can achieve atomic-level smoothness. This is in good agreement with the previous experimental study (Zhong et al., 2008) and molecular dynamics simulations (Ma et al., 2007). In the early stage, the incident C ions imping on the surface and engage in the of thin-film growth, and islanded nucleation at the valley's bottom, as observed by Ma et al. (Ma et al., 2007). The ions tend to settle near the valley's bottom, resulting in merging peaks and following the surface smoothness, as shown in Figure 4.2(c). The *ta*-C film grows in an island manner on the Si interlayer. As the island grows more significant and the peak-to-valley distance increases, the growth enters the roughening stage, as described in Figure 4.2(d). The steady evolution of the islands causes them to consolidate over time. Therefore, the surface roughness is uniform, and the surface smooths again, as shown in Figure 4.2(c-f). In addition, Shi et al. analyzed the morphological properties of *ta*-C films deposited by the FCVA technique over C⁺ ion energies 15 to 200 eV. They found that R_q roughness correlates with sp³ fraction. The highest sp³ fraction has the slightest roughness (0.12 nm) (Shi et al., 1999).

4.2 Chemical composition and structure

In this work, XPS was used to investigate the chemical composition and microstructure of ultrathin *ta*-C films. The high-resolution core level C1s spectra of the fabricated overcoats are shown in Figure 4.2(a). It is seen that C1s peak gradually shift from ~284 eV to ~285 eV when the thickness of the *ta*-C overcoat increases from 0.5 to 5.0 nm. To investigate the chemical compositions and bonding states, the C1s peaks were fitted with Gaussian-Lorentzian function after Shirley's background subtraction. The C1s peaks of all the *ta*-C overcoats comprises five visible bonds, including C-Si bonding at 283.20 ± 0.2 eV, sp²-C bonding at 284.30 ± 0.2 eV, sp³-C bonding at 284.90 ± 0.2 eV, C-O bonding at 286.20 ± 0.1 eV, and C=O bonding at 288.0 ± 0.2 eV (Dwivedi et al., 2014; Rismani et al., 2012; Soin et al., 2012; Yeo et al., 2015; Yeo et al., 2014). The relative atomic percentages of each carbon bond were estimated from the peak intensities, and the results are reported in Table 4.2. The sp³ bonds were found to be dominant in the structure, which is the characteristic of DLC films. Their relative atomic

percentages are in the range of 36.64-64.90%, which corresponds to the sp^3 bonds fraction ($sp^3/(sp^3 + sp^2)$) of 55.36-76.29%. It was also observed that the sp^3 bonds fraction decreased, whereas the sp^2 , C-O, and C=O bonds fractions increased as the overcoat thickness decreased. The presence of oxygen on the surface of the *ta*-C film is possibly due to physical or chemical adsorption, as well as contamination from the surrounding environment. The increase on the *ta*-C overcoat thickness and sp^3 bond fraction results in a denser carbon network (Ferrari et al., 2000). This can inhibit atmospheric oxygen migration through the *ta*-C overcoat as well as Si layer diffusion toward the surface, resulting in a reduction in carbon-oxygen (C-O and C=O) intensities. The observation of C-Si bonds suggests the formation of chemical bonds between the carbon and silicon at the Si/DLC interface.

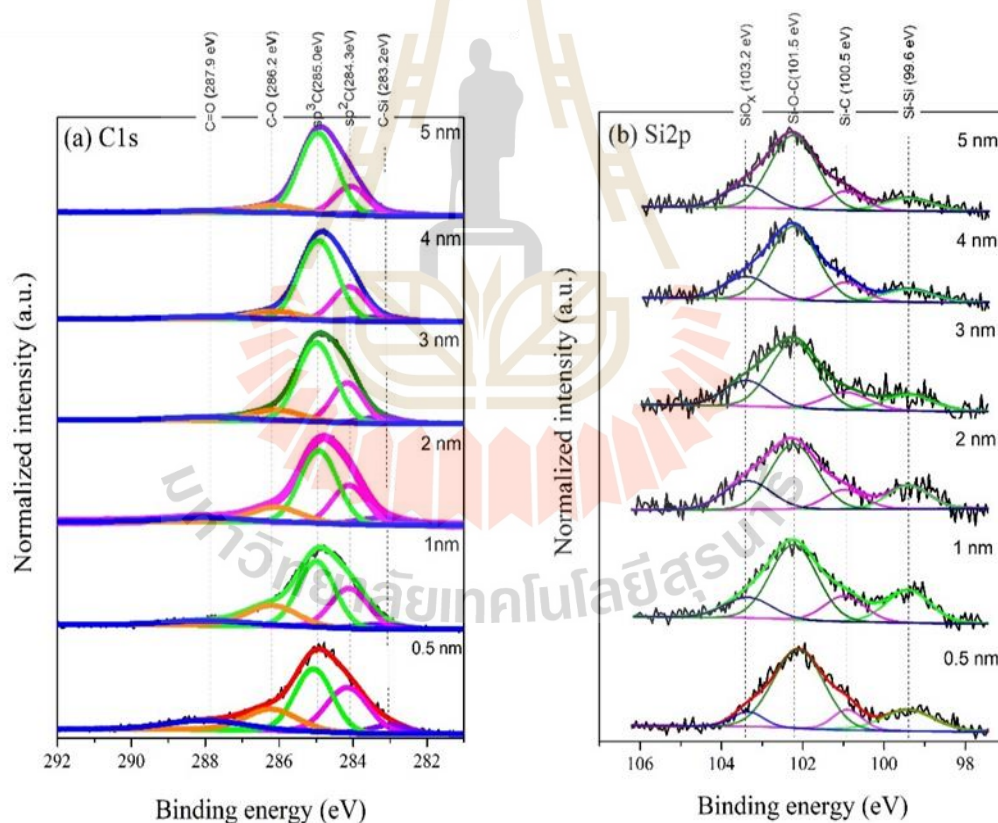


Figure 4.2 High resolution XPS spectra of (a) C1s and (b) Si2p peaks of the fabricated *ta*-C films with thicknesses of 0.5-5.0 nm.

The XPS Si2p spectra were obtained for all samples, as shown in Figure 4.2(b). The chemical state of the Si interlayer was deconvoluted with four Gaussian-Lorentzian distributions corresponding to the binding energies located at 99.40 eV, 100.97 eV,

102.22 eV, and 103.35 eV assigned to the Si element (Si-Si), silicon-carbide (Si-C) (Gallis et al., 2005; Wang et al., 2004), silicon-oxycarbide (Si-O-C) (Choi, et al., 1998; Dwivedi et al., 2014; Önnneby et al., 1997; Wang et al., 2004), and Si-O (Choi et al., 1998; Liu et al., 2013) bonds, respectively. Thus, the indicated Si atoms have reacted with the carbon ions to form Si-C bonds during the growing *ta*-C film in PFCVA. The existence of SiO_x bonds in the Si interlayer regions is due to the presence of residual silicon oxide. When carbon ions are supplanted into the Si interlayer, carbon radicals may create Si-O-C bonds with these residuals, forming Si-O-C bonds.

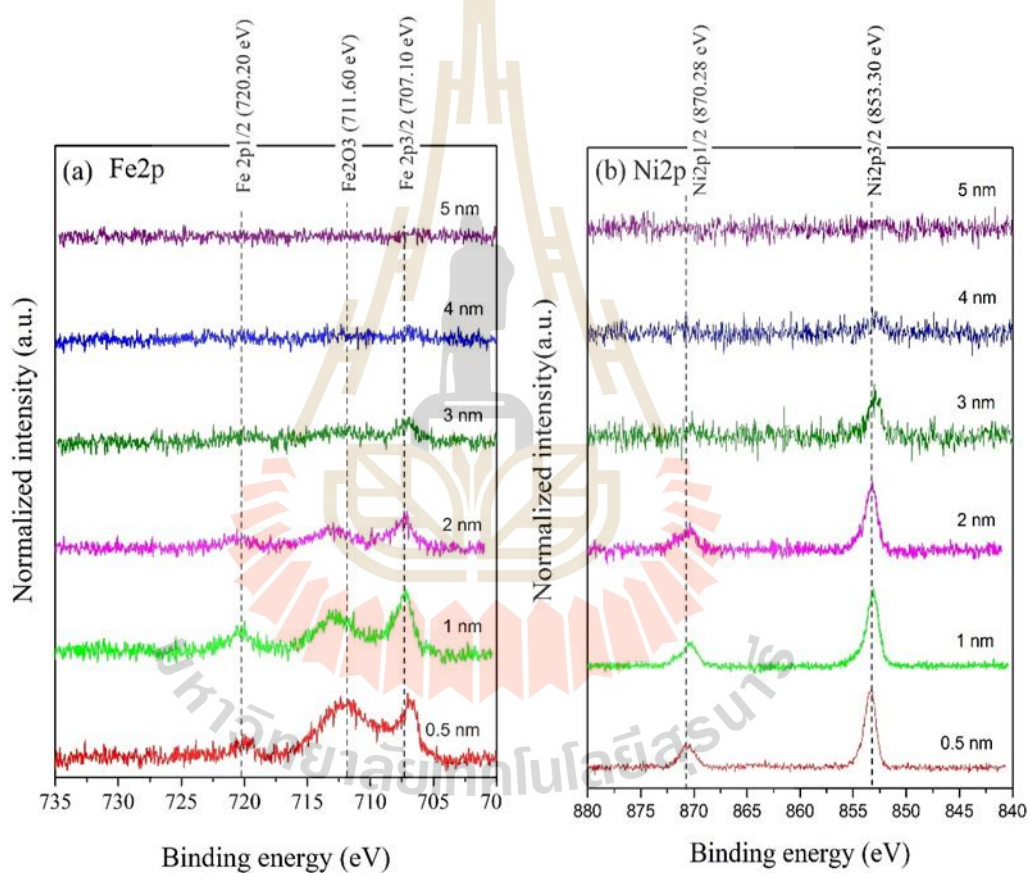


Figure 4.3 High resolution XPS spectra of (a) Fe2p and (b) Ni2p peaks of the fabricated *ta*-C films with thicknesses of 0.5-5.0 nm.

The high resolution XPS spectra of Si2p of the fabricated *ta*-C overcoats are shown in Figure 4.2(b). The Si2p peak was deconvoluted into four Gaussian-Lorentzian peaks at the binding energies of 99.40 eV, 100.97 eV, 102.22 eV, and 103.35 eV, corresponding to the Si element (Si-Si), silicon-carbide (Si-C) (Gallis et al., 2005; Wang et al., 2004), silicon-oxycarbide (Si-O-C) (Choi et al., 1998; Dwivedi et al., 2014; Önnneby

and Pantano, 1997; Wang et al., 2004), and Si-O (Choi et al., 1998; Liu et al., 2013) bonds, respectively. This result suggests that the Si atoms react with the carbon ions and form chemical bonds during the growth. The presence of SiO_x bonds is possibly due to residual silicon oxides in the Si interlayer structure. These residuals could also react with the energetic carbon ions and form Si-O-C bonds. The formation of Si-C and Si-O-C bonds between the DLC overcoat and Si-interlayer can enhance the adhesion between the carbon film and substrate. The high resolution XPS spectra of Fe2p and Ni2p peaks are shown in Figure 4.3. As the overcoat thickness is less than 3 nm, the signals of Fe2p^{3/2} and Fe2p^{1/2} were observed at the binding energies of approximately 707.10 eV and 720.20 eV, respectively, and the signals of Ni2p^{3/2} and Ni2p^{1/2} peaks appear at the binding energies of 853.30 and 870.28 eV, respectively. The observations of Fe and Ni signals are originated from the NiFe substrate, since the analysis depth of XPS technique is typically between 5-10 nm. This observation is consistent with the measured thicknesses of the fabricated overcoats.

The carbon hybridization state and bonding orientations were also investigated using NEXAFS. The C K-edge NEXAFS spectra of the fabricated overcoats are shown in comparison with HOPG in Figure 4.4. The HOPG spectrum has a similar visual shape to graphite spectra described elsewhere (Birrell et al., 2003; Watts et al., 2006), whereas all the C K-edge spectra of *ta*-C overcoats exhibit two distinct characteristics. The sharp pre-edge peak at ~285.5 eV and the broad photon energy peak between 290 and 320 eV are assigned to the unoccupied π^* and σ^* bands. The pre-edge resonance at ~285.5 eV is due to the transition from C1s orbital to unoccupied π^* orbitals. The broad peak covering photon energy between 290 and 320 eV resulted from the overlapping of C1s $\rightarrow \sigma^*$ transitions at sp² or/and sp³ sites. Since the π^* resonance is well separated in energy from the rest of the resonance in the C K-edge spectra. This the peak intensity of resonance can be considered a presentative of sp² contents (Abbas et al., 2005; Sooin et al., 2012). Figure 4.5(a) illustrates the intensity of the π^* peak at ~285.5 eV of C1s NEXAFS spectra of ultrathin *ta*-C overcoat increases with decreasing thickness for the overcoat thickness less than 1.0 nm. It decreases gradually until overcoat thickness rises to 5.0 nm as the study range, which is proportional to

the sp^2 hybridization carbon atom. This behavior of the $\pi^*C=C$ intensity indicates an initial rise and subsequent fall of the sp^2 bonding configuration (Mangolini et al., 2021).

Table 4.2 Relative atomic percentage of carbon bonds estimated from C1s peak.

Overcoat	Relative atomic percentage					
	C-Si	sp^2C	sp^3C	C-O	C=O	$sp^3/(sp^3+sp^2)$
0.5 nm	5.16%	29.55%	36.64%	18.16%	10.49%	55.36%
1.0 nm	4.04%	27.11%	42.90%	18.83%	6.12%	61.28%
2.0 nm	6.19%	24.15%	49.24%	14.54%	5.88%	67.09%
3.0 nm	4.69%	23.66%	55.92%	10.80%	4.93%	70.27%
4.0 nm	4.46%	23.24%	60.96%	8.17%	3.17%	72.27%
5.0 nm	4.83%	20.17%	64.90%	8.45%	1.65%	76.29%

The carbon hybridization state and bonding orientations were also investigated using NEXAFS. The C K-edge NEXAFS spectra of the fabricated overcoats are shown in comparison with HOPG in Figure 4.4. The HOPG spectrum has a similar visual shape to graphite spectra described elsewhere (Birrell et al., 2003; Watts et al., 2006), whereas all the C K-edge spectra of *ta*-C overcoats exhibit two distinct characteristics. The sharp pre-edge peak at ~ 285.5 eV and the broad photon energy peak between 290 and 320 eV are assigned to the unoccupied π^* and σ^* bands. The pre-edge resonance at ~ 285.5 eV is due to the transition from C1s orbital to unoccupied π^* orbitals. The broad peak covering photon energy between 290 and 320 eV resulted from the overlapping of C1s $\rightarrow \sigma^*$ transitions at sp^2 or/and sp^3 sites. Since the π^* resonance is well separated in energy from the rest of the resonance in the C K-edge spectra. This the peak intensity of resonance can be considered a presentative of sp^2 contents (Abbas et al., 2005; Soin et al., 2005; Soin et al., 2012). Figure 4.5(a) illustrates the intensity of the π^* peak at ~ 285.5 eV of C1s NEXAFS spectra of ultrathin *ta*-C overcoats increases with decreasing thickness for the overcoats thickness less than 1.0 nm. It decreases gradually until overcoats thickness rises to 5.0 nm as the study range, which is proportional to the sp^2 hybridization carbon atom. This behavior of the $\pi^*C=C$ intensity indicates an initial rise and subsequent fall of the sp^2 bonding configuration (Mangolini et al., 2021).

The normalized C K-edge NEXAFS spectra were fitted into multiple Gaussian resonance peaks using the ionization step function and the approach previously described. The deconvoluted peaks and their origins are summarized as follows. The peak at $\sim 285.5 \pm 0.1$ eV is originated from the $C1s \rightarrow \pi^*$ transition for disordered carbon-carbon bonds and related to the fraction sp^2C bonding in the near-surface region (Fedoseeva et al., 2016; Hemraj-Benny et al., 2006; Latham et al., 2017; Mangolini et al., 2018; Mangolini et al., 2021). The peak at 287.5 ± 0.2 eV is from the $C1s \rightarrow \sigma^*$ transition for $\sigma^*(C-H)$ bonds (Koshigan et al., 2015; Latham et al., 2017; Stöhr, 2013; Sumant et al., 2007). As illustrated in Figure 4.5(b), the C-H content showed approximately 1.16% that independence from film thickness. It is important to note that this bonding between the carbon and hydrogen atoms in the films, the peak can be attributed to the surface contamination and hydrocarbon absorption to the surface dangling bonds acting as defect sites, mainly at the surface. The shape peak at 288.8 ± 0.2 eV corresponds to the $C1s \rightarrow \sigma^*$ of C-Si and C-O (Fedoseeva et al., 2016; Mangolini et al., 2018; Mangolini et al., 2014; Wada et al., 2011). The XPS also confirms the detection of the C-Si bonds, shown in Figure 4.2(a). The presence of C=O is due to prolonged exposure of samples to the environment (Roy et al., 2005; Sainio et al., 2020; Soin et al., 2012). It is also observed from the XPS measurements. The sp^2 fraction can be calculated from the peak areas taken from the C K-edge spectrum of *ta*-C films and HOPG spectra.

The sp^2 fraction in the ultrathin *ta*-C overcoats with different thicknesses is shown in Figure 4.5(b). The thinnest *ta*-C overcoat exhibits the highest sp^2 fraction. In order to gain a deeper insight of how sp^2 clustering in the microstructure of ultrathin *ta*-C overcoats, visible Raman spectroscopy was employed. This technique is sensitive to highly symmetric covalent bonds, as visible photons are sufficient to excite the π states than σ states. However, the visible Raman spectrum represents the ordering of sp^2 sites and, thereby, indirectly on the fraction of sp^3 sites. Raman spectra excited by a laser of wavelength 532 nm of the ultrathin *ta*-C overcoats with thicknesses ranging from 0.5 to 5.0 nm are shown in Figure 4.6. The visible Raman spectra of the fabricated *ta*-C overcoats show a broad peak in the region of $1100-1800\text{ cm}^{-1}$, which can be deconvoluted into two distinctive peaks using a Gaussian distribution and linear

background subtraction. The first peak, graphitic (G) peak, at the wavenumber of 1530-1560 cm^{-1} is formed by the in-plane bond stretching motion of all aromatics (rings) and olefinic sp^2C pairs (chains). This peak is essential for distinguishing amorphous carbon from graphitic and nano-crystalline graphitic films. The observation of this peak is consistent with the previous reports. Ferrari and Robertson (Ferrari and Robertson, 2001) discovered that crystalline graphite has a G peak at 1580 cm^{-1} and nano-crystalline graphite (nc-graphite) has a G peak of about 1580-1600 cm^{-1} . Praver et al. (Praver et al., 1996) and Anders et al. (Anders et al., 1997) demonstrated that the minimum position for the G peak is never less than 1500 cm^{-1} .

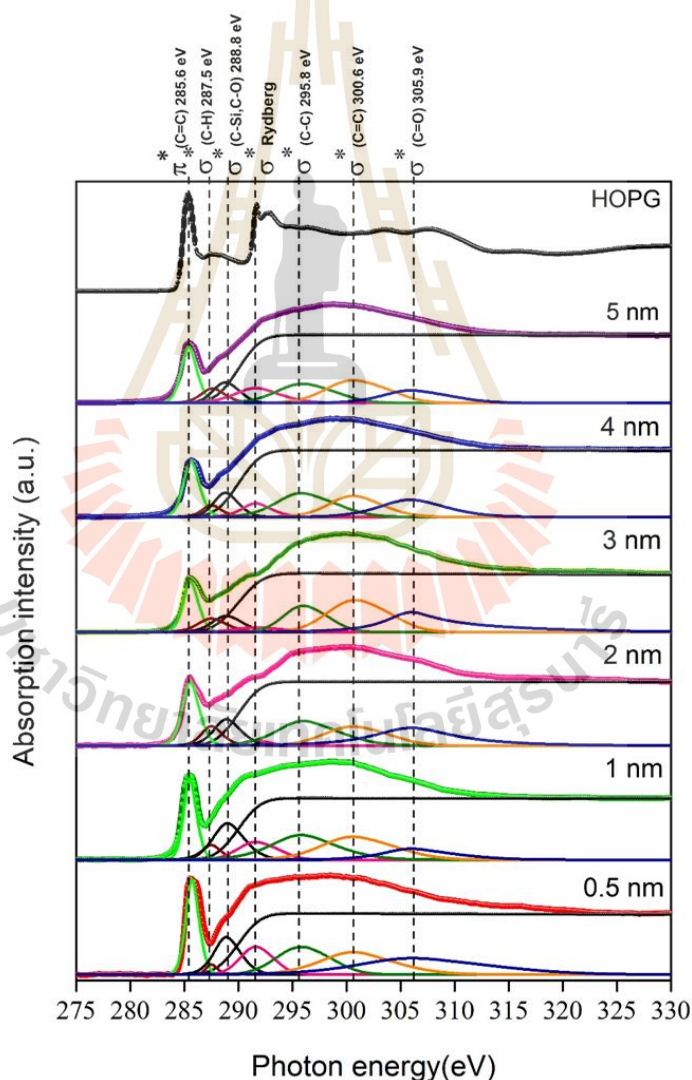


Figure 4.4 Carbon (C) K-edge NEXAFS spectra of HOPG and ultrathin *ta*-C overcoats deposited by PFCVA technique presenting the evolution of the $\text{C}1s \rightarrow \pi^*$ and $\text{C}1s \rightarrow \sigma^*$ transitions with *ta*-C overcoat thickness.

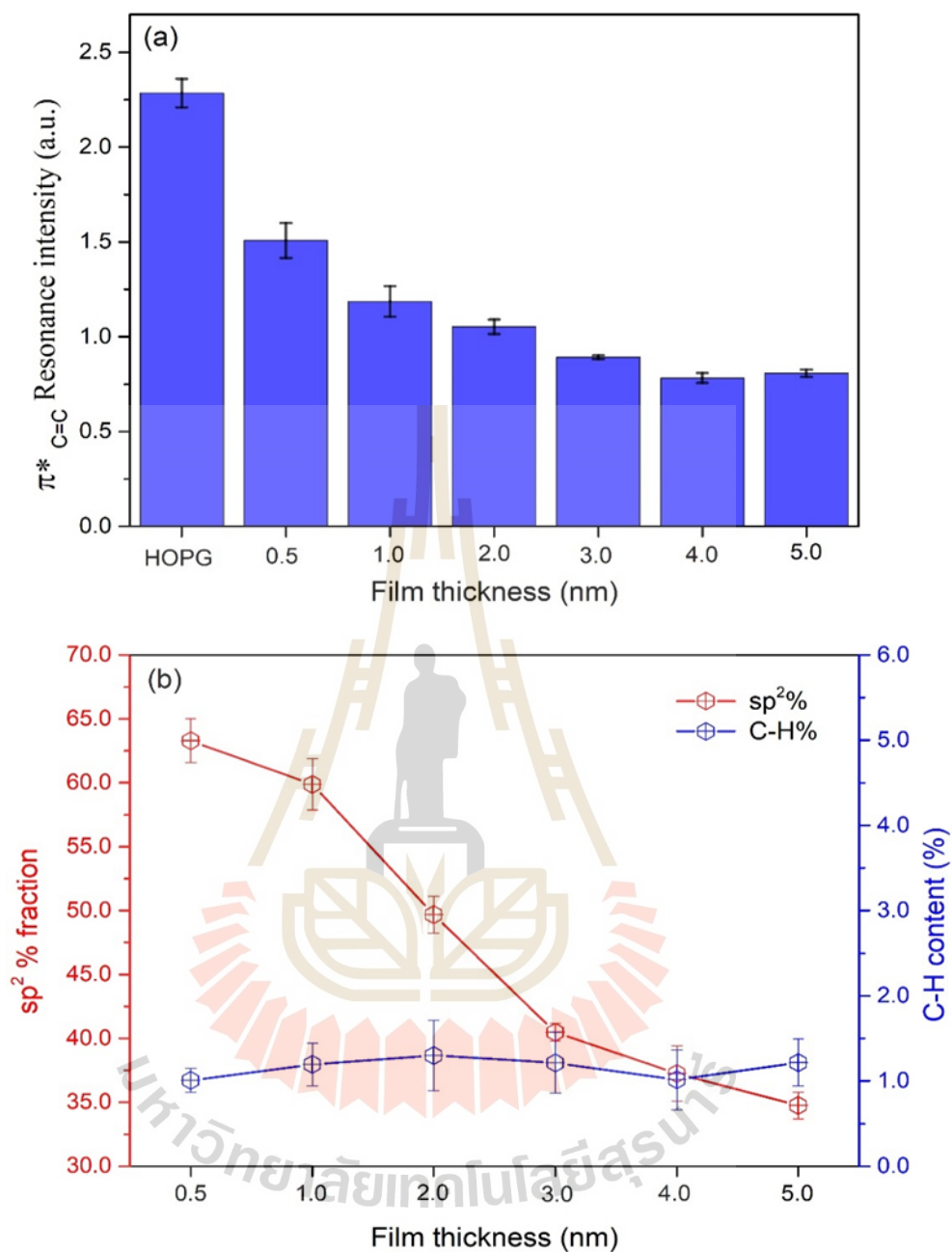


Figure 4.5 (a) the π^* resonance intensity and (b) the sp^2 fraction and C-H content were deduced from the NEXAFS spectra as a function of film thickness.

The second peak, shoulder peak, is described as the disorder (D) peak which is observed at a wavenumber of between 1330 and 1350 cm^{-1} . This peak is formed only by the breathing mode of sp^2 atoms in aromatic rings.

The intensity ratio of the D peak to the G peak (I_D/I_G) in amorphous carbon films has a substantial impact on the microstructure and can be used to assess the size of

sp² clusters. A relationship between the sp² clusters size (L) and I_d/I_g can be established as follows (Ferrari and Robertson, 2000).

$$\frac{I_d}{I_g} = CL^2 \quad (2)$$

Where C is a constant. It has a value of 0.0055 for the 532 nm excitation wavelength.

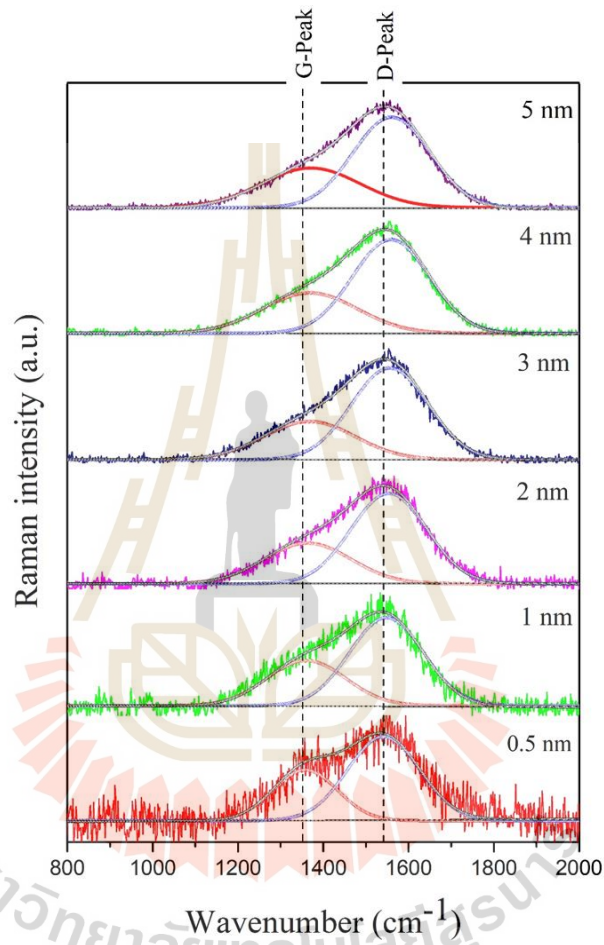


Figure 4.6 Normalized Raman spectra excited by a laser wavelength of 532 nm in the range of 800-2200 cm⁻¹ of the fabricated ultrathin ta-C overcoats.

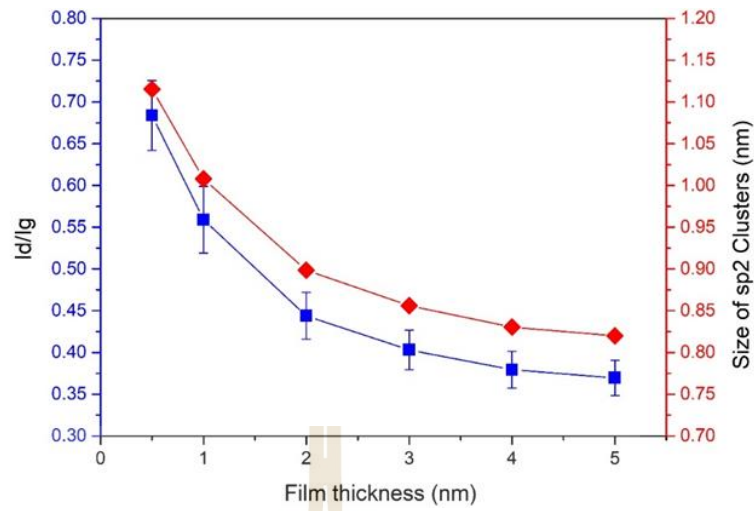


Figure 4.7 I_d/I_g ratio and size of sp^2 clusters dependent on the thickness of ta -C films, deposited by pulsed filtered cathodic vacuum arc.

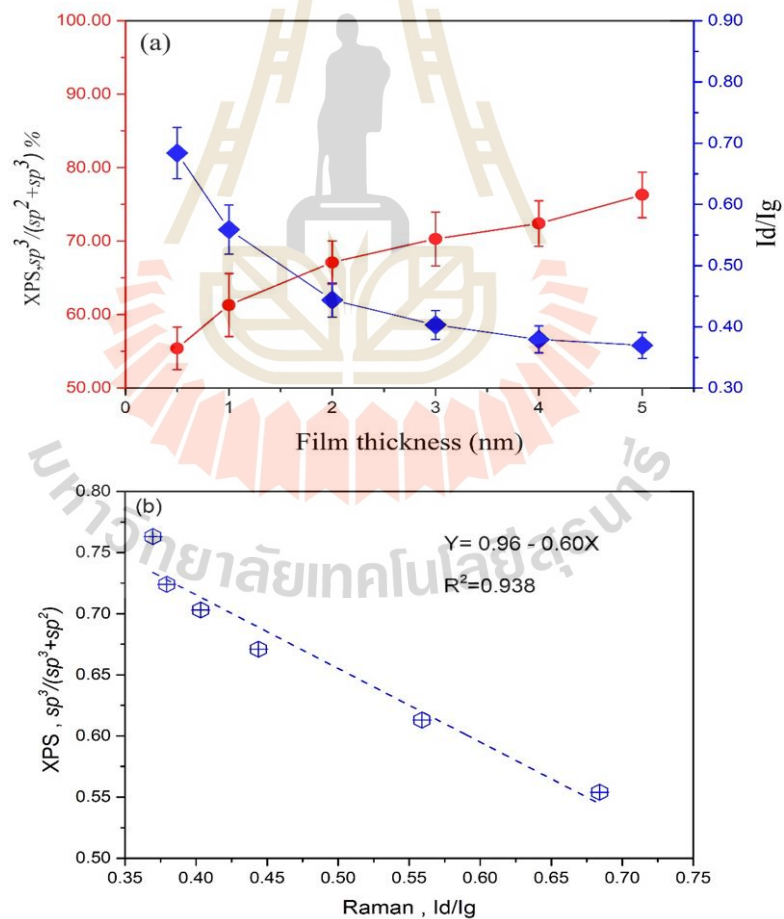


Figure 4.8 (a) Plots between $sp^3/(sp^2+sp^3)$ ratio estimated from XPS spectra and I_d/I_g ratio as a function of the ta -C overcoat thickness. (b) The correlation of $sp^3/(sp^2+sp^3)$ ratio and I_d/I_g ratio of ta -C overcoats.

Figure 4.7 illustrates the relationship between I_d/I_g and sp^2 cluster sizes and thickness of the fabricated *ta*-C overcoats. Both I_d/I_g and the size of sp^2 clusters decrease as the overcoat thickness increases. The I_d/I_g ratio decreases from 0.68 to 0.36 and the size of sp^2 clusters decreases from 1.12 to 0.82 nm as the overcoat thickness increased from 0.5-5 nm. The result is in good agreement with the earlier reports. Goohpattader et al. used constant ion energy for fabrication of DLC films and discovered that the size of sp^2 clusters reduced as the deposition time increased (Goohpattader et al., 2015). Figure 4.8(a) shows the plots of the $sp^3/(sp^2+sp^3)\%$ estimated from XPS spectra and the I_d/I_g ratio as a function of overcoat thickness and Figure 4.8(b) depicts the correlation between the I_d/I_g ratio and the $sp^3/(sp^2+sp^3)$ ratio estimated from XPS spectra. It was observed that the relation is a negative slope, and the R-square for the correlation is 0.94, indicating that the I_d/I_g ratio is inversely proportional to the $sp^3/(sp^2+sp^3)\%$ ratio.

The most significant observation of this study is that the migration of sp^2 sites to sp^3 sites occurs in a transition from rings to chains in the sp^2 configuration when the *ta*-C overcoat thickness increases. The results are consistent with Ferrari and Robertson's three-stage phenomenological method for the interpretation of Raman spectra of *ta*-C films at any excitation energy (Ferrari and Robertson, 2000).

However, ultra-thin DLC is used in magnetic recording hard disk drives to improve the wear durability of their head-disk interface (HDI), which relates to friction and is a tribology property. As a result, increasing the thickness of the ultrathin *ta*-C layer influences surface roughness and friction evolution (discuss in next section).

4.3 Tribological performances

The tribological properties of the fabricated ultrathin *ta*-C overcoats were determined by a ball-on-disk wear test. In the test, the samples were fixed while the counterface was in contact with the surface. This configuration is similar to the working condition of HDD and allows the estimation of COF (Dwivedi et al., 2021). The test was carried out more than 10000 cycles, which is much more than the HDD operational

lifetime (Dwivedi et al., 2015). The examined friction curves and the optical microscopic images captured after the test of the fabricated ultrathin *ta*-C overcoats with thicknesses ranging from 0.5 to 5.0 nm in comparison with a cleaned NiFe substrate and a Si-interlayer on the NiFe substrate are shown in Figure 4.9 and Figure 4.10 depicts, respectively. It is seen that the COFs of the NiFe substrate and the Si interlayer fluctuate with test cycles with an average value of 0.70 and 0.69, respectively. After the test, severe wear tracks and debris formations appeared in the optical images captured after the results of the test. The observed wear between the ball and the substrates was therefore related to the fluctuations in COF. On the other hand, the COF of the fabricated the *ta*-C overcoats with thicknesses ranging from 2.0 nm to 5.0 nm remained constant in the range of 0.18-0.27 during the test. This COF value is slightly lower than the COF value of approximately 0.3-0.5 reported in existing 0.27 nm commercial carbon overcoats (Dwivedi et al., 2015; Dwivedi et al., 2015). No visible wear track or debris was observed in the optical pictures taken following the test. However, as the thickness of the *ta*-C overcoats increased to 0.5 and 1.0 nm, the COF showed significant fluctuations with test cycle and their average values abruptly increased to 0.70 and 0.62, respectively. This resulted in a wear track being visible in the optical images taken after the test, as seen in Figure 4.10(c) and 4.10(d).

4.4 Discussion

Figure 4.11 presents the plot of R_D , the I_D/I_G ratio obtained from Raman spectroscopy, the sp^2 fraction estimated from NEXAFS, and the COF of the *ta*-C overcoats as a function of thickness. The plot clearly indicates that the sp^2 fraction of the *ta*-C overcoats is inversely proportional to their thickness. The sp^2 fraction increases as the overcoat thickness decreases, and suddenly increases when the overcoat thickness is reduced to 1 nm, which is consistent with the rise in I_D/I_G reported from Raman spectroscopy.

Several models, including the subplantation model (Davis et al., 1998; Lifshitz et al., 1994; Robertson, 2002), have been proposed to explain the formation of a *ta*-C film fabricated by the PFCVA technique. The PFCVA generates a plasma of highly

energetic carbon ions that are capable of embedding themselves in a growing film. The produced carbon ions can penetrate the surface, resulting in the densification of carbon in the subsurface and the formation of sp^3 hybridization. The formation of sp^3 hybridization is strongly determined by the carbon ion energy and growth temperature (Davis et al., 1998; Lifshitz et al., 1994).

The film is formed as three cross-sectional layers; interface layer, bulk layer, and surface layer (Casiraghi et al., 2004; Davis et al., 1998; Matlak and Komvopoulos, 2018). While the interface and surface layers have higher sp^2 fractions, the bulk layer has a higher sp^3 fraction. The spatially resolved cross-sectional electron energy loss spectroscopy (EELS) analysis has confirmed the presence of a thin surface layer with a high sp^2 fraction, with a thickness of between 0.4 nm and 1.3 nm for carbon ions with energies of 35 eV and 320 eV, respectively (Davis et al., 1998). It has also been demonstrated that the high sp^2 bonded surface layer does not arise after the film growth, but rather is present during the growth of the high sp^3 bonded bulk layer (Davis et al., 1998). As the film grows, the bottom part of the surface layer is converted into sp^3 hybridization by subsurface deposition process and the top of sp^2 bonded surface layer expand away from the substrate. Our result seems to be in good agreement with the assumption. It was expected that the ultrathin *ta*-C films with thicknesses of between 0.5-1.0 nm would mainly compose of surface and interface layers with high sp^2 fraction. As the deposition parameters, specifically ion beam energy and substrate temperature, were kept consistent in the growth process, the characteristics of the surface and interface layers would not change when varying the overcoat thickness. When the overcoat thickness increased, the dense bulk layer with high sp^3 fraction was formed and expanded, while the surface layers remained unchanged. As a result, the sp^3 fraction increased with thickness. It was also observed that the decrease of sp^2 fraction significantly reduced the COF of the overcoat.

The R_q , on the other hand, does not show a strong correlation with the sp^2 fraction of the overcoat. This observation contradicts to the previous findings that the roughness of *ta*-C films correlates with the amount of sp^2 atomic content. The lowest roughness occurs at the lowest sp^2 atomic content (Lifshitz et al., 1994; Shi et al., 1999; Shi et al., 1999).

In this work, the R_q of the ultrathin *ta*-C films was found to be strongly influenced by the morphology of the substrate. It tended to follow the surface roughness evolution for general cases (Casiraghi et al., 2005). This behavior has also been reported and explained by Zhong et al. (Zhong et al., 2008). In the first stage of the growth, the deposited carbon atoms arrive (condensation), migrate (diffusion), and aggregate into two-dimensional adatom islands (nucleation) on the surface. The deposited ions prefer to settle at adsorption sites on the bottom of the valley on the surface as their capture areas are greater than other positions, resulting in the smoothness of the surface (Ma et al., 2007; Zhong et al., 2008). It was observed in this work that after the deposition of the *ta*-C film with a thickness of 0.5 nm, the surface of the Si interlayer with R_q of 0.26 nm became smoother with R_q of 0.20 nm. As the surface becomes smoother, a series of islands is formed due to the aggregation of carbon atoms at the valley in the initial smoothness stage, resulting in quickly increased surface roughness. The R_q increased to 0.23 nm was observed for the film thickness of 1 nm. As the island coalesce to form a closed and continuous film, the surface roughness reaches the maximum and then decreases in the second stage. The surface roughness become constant in the third stage and gradually increase above a roughening transition. The R_q gradually decreased and became constant at approximately 0.13 nm for the film thickness greater than 2.0 nm. The observed evolution of surface morphology with thickness is also consistent with the structure of the film as it is shown that the bulk film with high sp^3 bonded carbon has not been completely formed for the thickness of 0.5-1.0 nm. This result suggests that the initial roughness may also affect the formation and evolution of high sp^3 fraction bulk layer with film thickness.

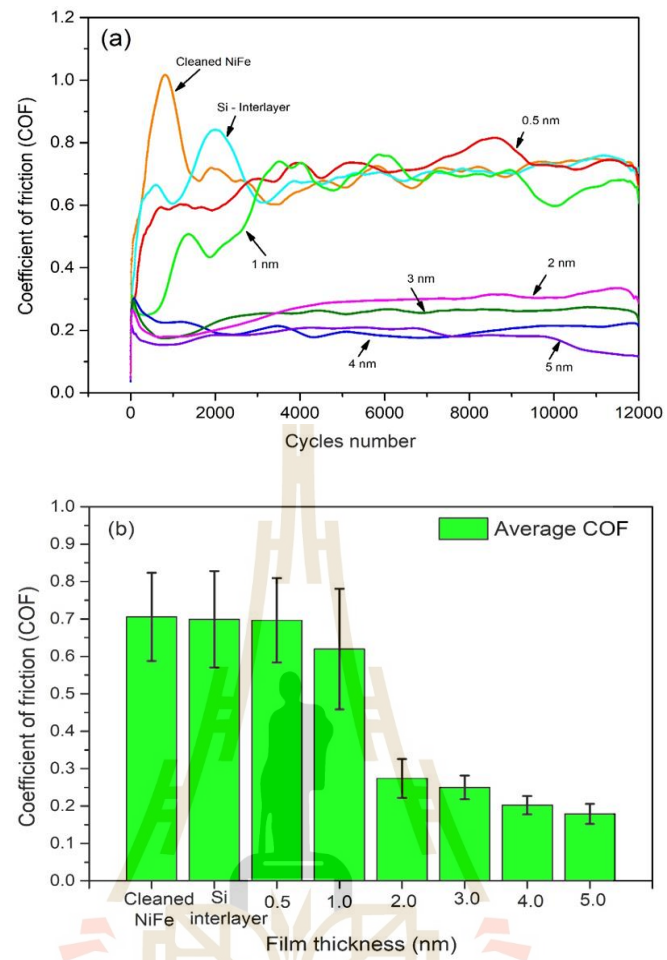


Figure 4.9 (a) Friction curves and (b) COF of the cleaned NiFe, Si-interlayer deposited, and fabricated *ta*-C overcoat with thicknesses of 0.5-5.0 nm.

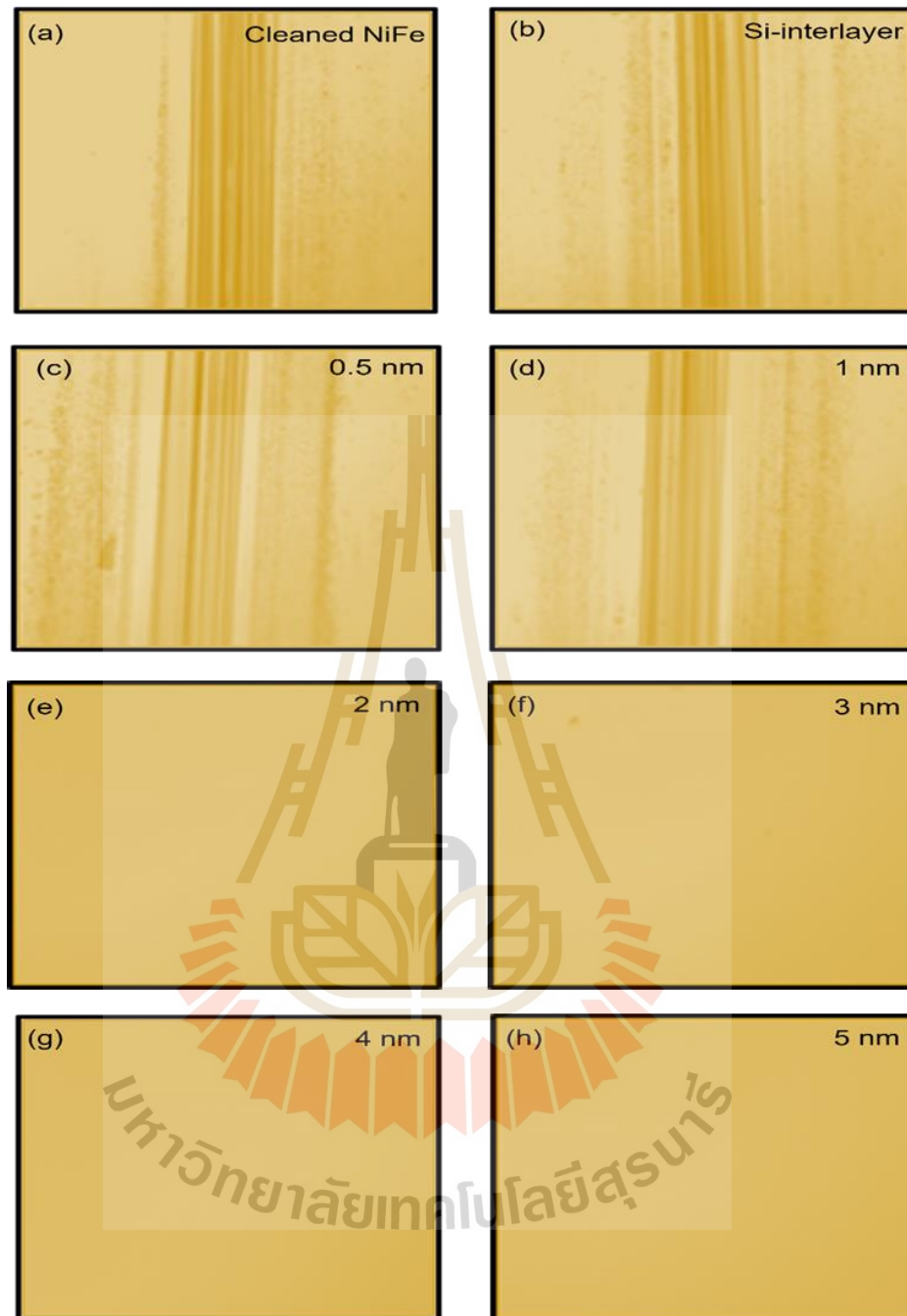


Figure 4.10 Optical images of a NiFe substrate, a Si interlayer, and *ta*-C overcoats with thicknesses of 0.5-5.0 nm after slide reciprocating tribological test.

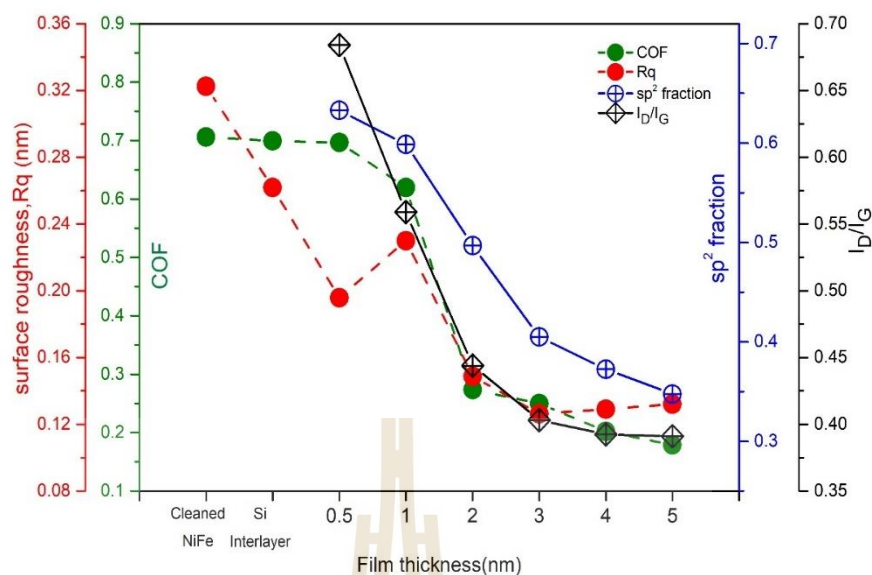


Figure 4.11 Plot of R_q , I_d/I_g ratio, sp^2 fraction estimated from NEXAFS, and COF as a function of ta -C overcoat thickness.

PART II- Influence of an interlayer on ultrathin ta -C overcoats

In this part, the influence of an interlayer on structure and tribological properties of ultrathin ta -C overcoat was studied. Two different interlayers, namely, Si and SiN_x with thicknesses of between 0.5-1.0 nm were applied between the surfaces of substrate and ta -C overcoat layer. The ultrathin overcoats were consequently characterized by in this study to determine the influence of the interlayer thickness on the structure of the film. Sputtering is used to deposit Si and SiN_x interlayers with thicknesses ranging from 0.5 to 1 nm, followed by deposition of PFCVA deposited 1.0 nm thick of ta -C on top of the Si and SiN_x layers. The deep characterization is detail as below.

4.5 Influence of interlayers on surface morphology

In this work, the Si and SiN_x interlayers with thickness of of 0.5 and 1nm were deposited on NiFe substrates by a sputtering technique. Consequently, ultrathin ta -C overcoats with a thickness of 1nm were deposited by the FCCVA technique. The

interlayers and *ta*-C overcoats were both produced in the same chamber vacuum without the need for vacuum breakdown. The thicknesses of all fabricated interlayers and *ta*-C overcoats were determined by WDXRF and are lists in Table 4.3.

Table 4.3 Thickness of interlayer and tetrahedral amorphous carbon.

Sample	WDXRF thickness (nm)		Sample	WDXRF thickness (nm)	
	Si	<i>ta</i> -C		SiN _x	Si
Clean NiFe	0.00	0.00	C10	0.00	0.91
5Si	0.64	0.00	5SiN _x	0.52	0.00
10Si	1.01	0.00	10SiN _x	1.02	0.00
5SiC10	0.59	0.97	5SiN _x C10	0.47	1.12
10SiC10	0.91	1.04	10SiN _x C10	0.90	1.04

As shown in Figure 4.12-4.13(a), the surface roughness of Si and SiN_x interlayer films was deposited at various thicknesses ranging from 0.5 to 1.0 nm that found the roughness of the samples 5Si, and 10Si was nearly identical ($R_q \sim 0.26$ nm). Similar to the surface roughness of samples 5SiN_x, and 10SiN_x was almost shown ($R_q \sim 0.27$ nm). When considering Si and SiN_x interlayer varied from 0.5 to 1.0 nm with a 1 nm thick *ta*-C overcoat that exhibited the roughness of samples 5SiN_xC10, and 10SiN_xC10 were estimated ($R_q \sim 0.19$ nm) and slightly lower than the samples 5SiC10, and 10SiC10 ($R_q \sim 0.22$ nm) and equivalent to a 1 nm thick *ta*-C coat without an interlayer C10 ($R_q \sim 0.21$ nm). The result indicates that film surface smoothens in atomic level and important low surface roughness in order to have better tribological and corrosion performances, and it is advantageous in the nanoscale regime since it allows for reducing the magnetic spacing in order to have higher storage densities (Casiraghi et al., 2005; Yeo, Dwivedi, et al., 2014).

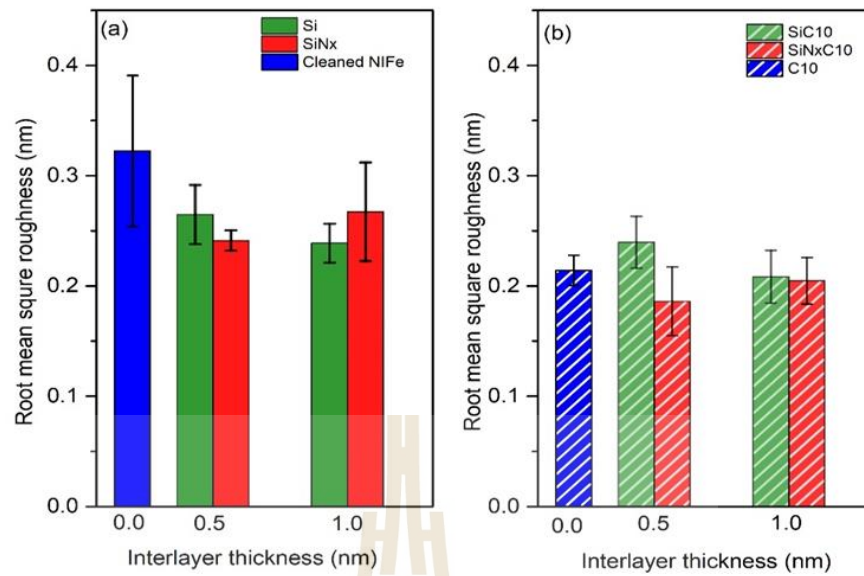


Figure 4.12 Average root means square surface roughness (R_q) of the NiFe substrate, the interlayer (a) 0.5-1.0 nm of Si and SiN_x interlayer without *ta*-C overcoat. (b) Varying 0.5-1.0 nm of Si and SiN_x interlayer with 1 nm *ta*-C overcoat.

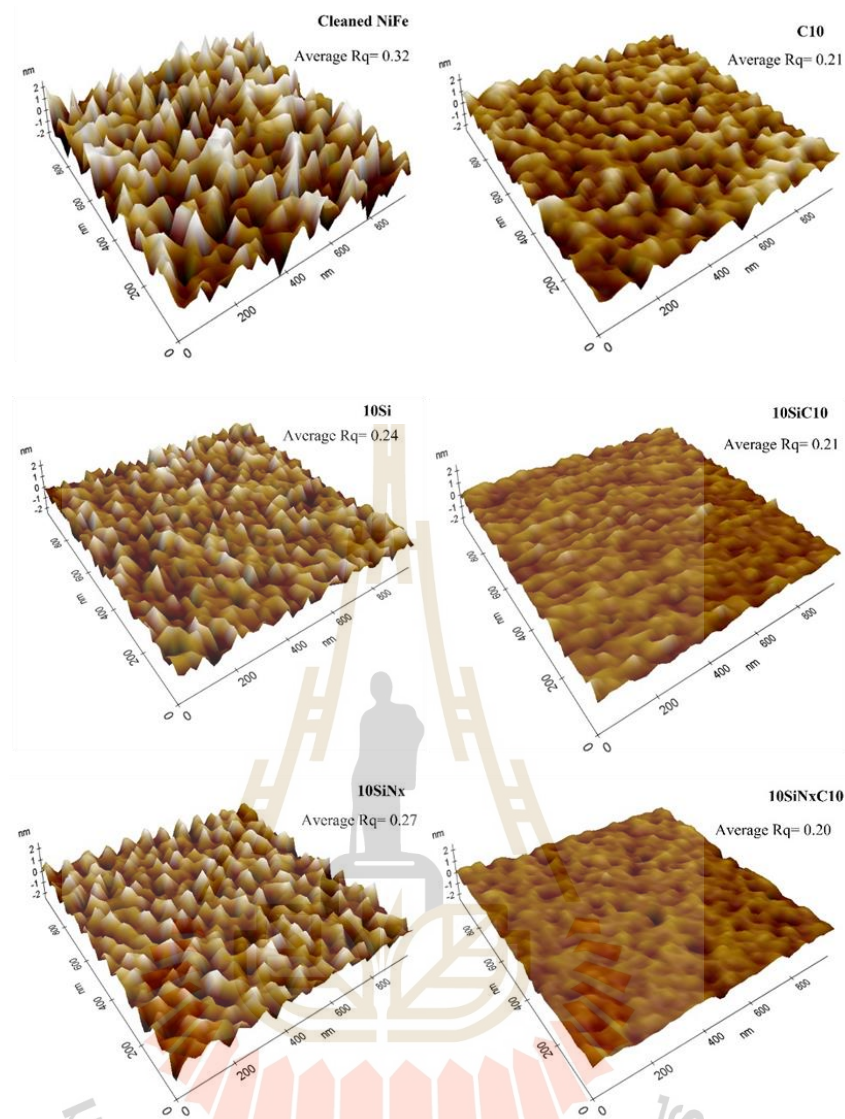


Figure 4.13 AFM images 3D scan size 1x1 μm area of cleaned NiFe substrate, 1 nm monolithic *ta*-C film (C10), 1 nm monolithic Si and SiN_x interlayer (10Si,10SiN_x), and composited layer 10SiC10 and 10SiN_xC10.

4.6 Tribological properties

The coefficients of friction (COF) values were determined during a reciprocating ball-on-disk tribological test for monolithic Si and SiN_x layers of 0.5-1 nm thickness, referred to sample as 5Si, 10Si, 5SiN_x, and 10SiN_x, respectively. While cleaned NiFe serving as a reference, as shown in Figure 4.16. The 1 nm overcoat thick *ta*-C deposited over interlayer with different Si and SiN_x thickness of 0.5 and 1 nm, referred to sample

as 5SiC10, 10SiC10, 5SiN_xC10, and 10SiN_xC10, respectively. While 1 nm thick *ta*-C sample is for reference as C10 sample. For the purpose of comparing their tribological behavior, all samples were examined under the same conditions.

As shown in Figure 4.14, the average coefficient of friction (COF) determined during the reciprocating tribology test and a variation of the COF for varying interlayer thicknesses, with and without *ta*-C coating, was determined throughout the test presented in the bar chart. Despite the fact that the thickness of monolithic Si and SiN_x without any protective coating ranged from 0.5 to 1 nm, the samples 5Si, 10Si, 5SiN_x, and 10SiN_x all exhibited high COF values of 0.73, with no statistically significant variation in COF between them. Because of this, it is proved that the coefficient of friction is independent of the thickness of the interlayers between Si and SiN_x. In conclusion, monolithic Si and SiN_x layers have poor tribological performance, as demonstrated in this study. However, the COF of the variant with Si and SiN_x overcoat with 1.0 nm thick *ta*-C film, the samples 5SiC10, 10SiC10, 5SiN_xC10, and 10SiN_xC10 showed values of 0.60, 0.57, 0.50, and 0.47, respectively. It can be seen as a result that indicated the tribological performance of the Si and SiN_x interlayers, when overcoated with a *ta*-C layers, improved by 9.1% and 24.2%, respectively, when compared to 1.0 nm of thin monolithic *ta*-C.

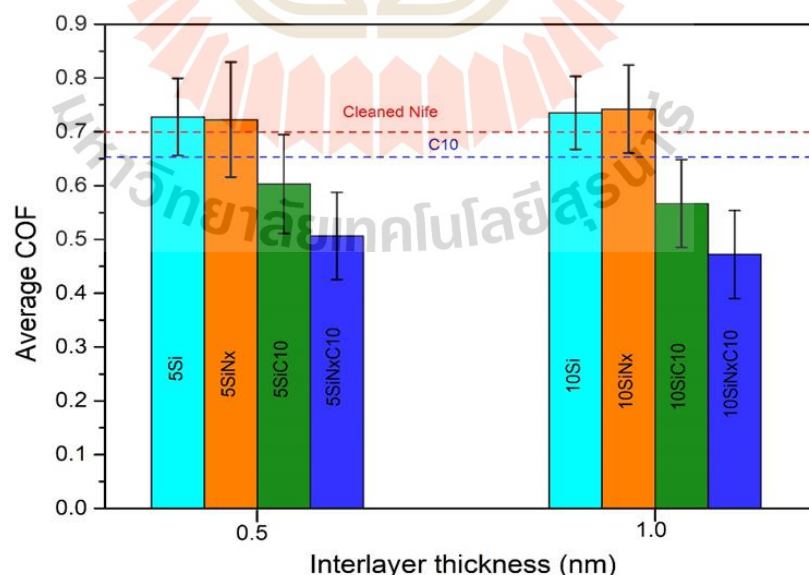


Figure 4.14 Dependence COF and interlayer thickness of Si and SiN_x with respect to number of cycles as obtained from ball-on-disk tribological tests.

To narrow down the comparison of tribological performance between Si and SiN_x with a 1.0 nm protective *ta*-C coating, the COF of samples 5SiC10 and 10SiC10 declined from 0.60 to 0.57, and the COF of samples 5SiN_x10 and 10SiN_xC10 followed the same pattern by decreasing from 0.51 to 47, respectively. It can be shown in Figure 4.14 that the COF decreases as a function of the thickness of the interlayer. Moreover, the COF of the SiN_x interlayer is less than that of the Si interlayer. In context of this findings, the effectiveness of *ta*-C deposition improvement in frictional characteristics is enhanced by the addition of Si or SiN_x underlayer. The enhanced tribological features afforded by SiN_x/*ta*-C and Si/*ta*-C bilayer overcoats can be attributed to the increased interfacial bonding, and the enhanced sp³ carbon hybridization can be discussed further in Raman and XPS.

4.7 Raman analysis

Raman spectroscopy is widely used to investigate the structure of amorphous carbon materials because of its non-destructive nature and sensitivity to translational symmetry (Ferrari et al., 2000). The visible Raman was taken using a laser at a wavelength of 532 nm to depth view into the microstructure of the *ta*-C overcoats. Figure 4.15 show the visible Raman spectra of samples 10C, 5SiC10, 10SiC10, 5SiN_xC10, and 10SiN_xC10 from the same deposition condition.

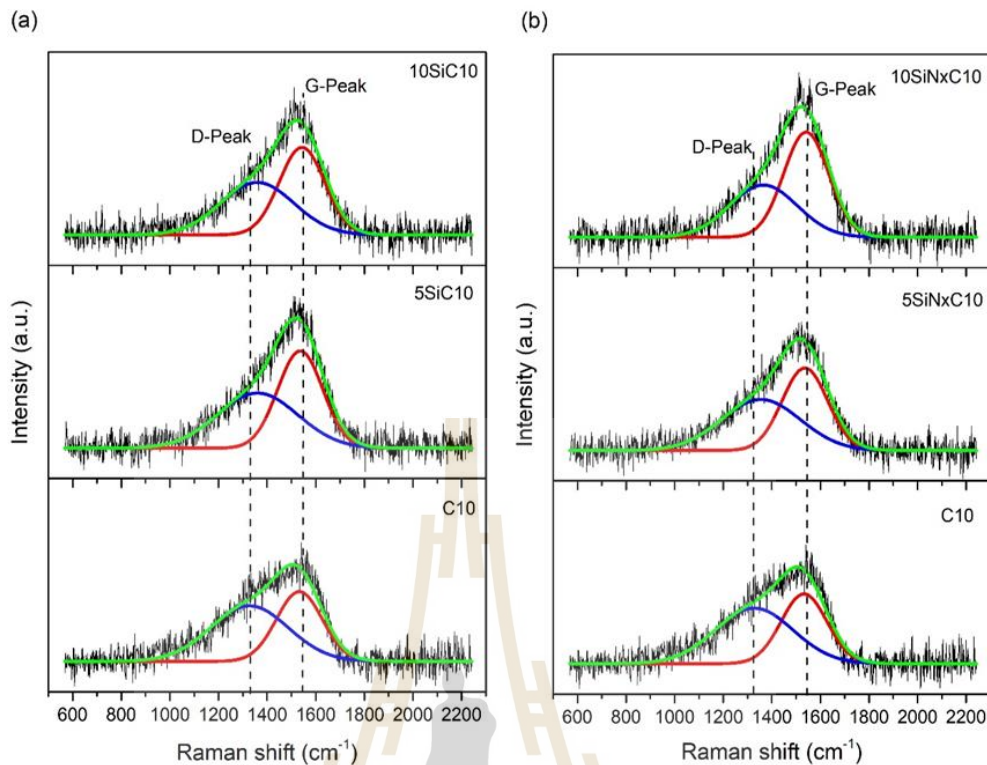


Figure 4.15 Raman spectra of DLC films with different interlayer thickness 0.0-1.0 nm of (a) Si and (b) SiN_x amorphous interlayer with 1 nm *ta*-C overcoat film, with the D and G peak.

As seen in Figure 4.15, Raman spectroscopy of DLC films with different Si and SiN_x interlayer thicknesses by varying 0.5-1.0 nm and overcoat with 1.0 nm *ta*-C film. The spectra were presented in the range of 1100-1800 cm⁻¹, which suggested that the samples possessed the typical DLC structural characteristic. The spectra of all samples were deconvoluted using two Gaussian distributions and linear background. The Raman spectra of the DLC film surface from the examined samples, with the characteristics D (disorder) and G (graphite) bands, show an average centered at ~1358 cm⁻¹ and ~1540 cm⁻¹, respectively. As is widely known, visible energy at 532 nm excitation, the sp² sites possess such a high cross-section that they dominate the spectra, which respond only to the configuration or order of the sp² sites. In contrast, the sp³ sites are invisible. Therefore, the G and D peaks are due to sp² sites. The G peak is due to the bond stretching of all pairs of sp² atoms in both rings and chains. The D peak is due to the breathing modes of sp² atoms in rings induced by disorder-activated aromatic modes of A1 symmetry (Ferrari et al., 2000; Ferrari et al., 2001). The spectra were deconvoluted

by carefully fitting the G peak and D peak. The G position and I_D/I_G ratio were extracted. Figure 4.16 represented the parameters regarding the G and D peak extracted from the Raman spectra as a function of the thickness of the Si and SiN_x interlayers increasing from 0 to 1.0 nm and overcoated by 1 nm thick *ta*-C films. The G peak and D peak intensity as I_D/I_G ratio that exhibited to decrease with an increasing interlayer thickness of both, despite the fact that the *ta*-C thickness remained constant, contrasted with the trend increasing of G position in spectra of *ta*-C films. As a result that the decrease in I_D/I_G ratio indicated an increase of sp^3 fraction (FC et al., 2006; Liu et al., 2013). The position of the G peak was also shown to be related to the sp^3 fraction. When the sp^3 fraction grew, the sp^2 fraction and size of the sp^2 cluster decreased, and the bond order increased, resulting in an increase in the Raman frequency. This meant that the upward shift of the G peak position corresponded to a high sp^3 content.

As evidenced by the I_D/I_G ratio trend, the presence of Si and SiN_x interlayers promotes the sp^3C bonding with the *ta*-C overcoat. However, the SiN_x interlayer generated lower I_D/I_G than Si-interlayer. To explore the bonding environment of the interfered region between the interlayer and *ta*-C layer in more insight.

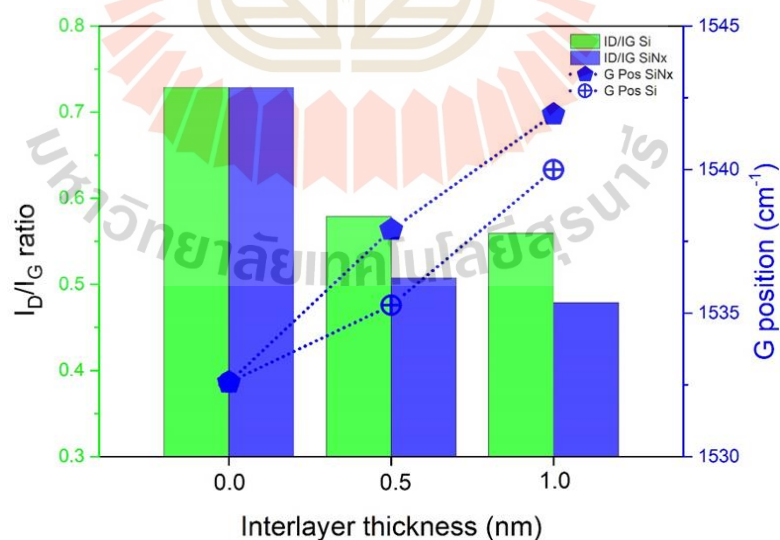


Figure 4.16 Variation of the I_D/I_G ratio and the G position as a function of the thickness of the Si and SiN_x interlayer varying from 0 to 1 nm.

4.8 Chemical and interfacial bonding analysis

It has been demonstrated that the synergistic effect of the SiN_x interlayers in the range of 0-1.0 nm with 1 nm *ta*-C thick overcoated layer can significantly improve the functional properties of friction durability when compared to monolithic *ta*-C and *Si/ta*-C of the same thickness has been demonstrated. It is therefore critical to understand the underlying cause of this augmentation by linking it to the chemical bonding of the substance. Overcoats containing carbon have to be studied to better understand their chemical structure and oxidation. XPS was used to examine chemical bonding inside the ultrathin overcoat layer. XPS analyses were also performed on the Si and SiN_x interface region with *ta*-C amorphous carbon overcoats as samples 5SiC10, 10SiC10, 5SiN_xC10, and 10SiN_xC10, as well as the C10 sample, which comprised of a monolithic 1 nm *ta*-C overcoat generated using the same PFCVA method. The purpose of sample C10 was to provide as a reference for comparison. To remove any background noise, executing Shirley's background subtraction correction was conducted before fitting the XPS core-level spectra of each element. Figure 4.17 shows the fitting of the C1s core level spectra was accomplished with a Gaussian-Lorentzian line shape, and all samples had four constituent peaks, which used to be consistent throughout all samples corresponding to the sp^2 bonding in carbon assigned to sp^2C at 284.2 ± 0.2 eV, sp^3 bonding in carbon assigned to sp^3C at 285.0 ± 0.2 eV, C-O bonding at 286.2 ± 0.1 eV, and C=O bonding at 288.0 ± 0.1 eV (Dwivedi et al., 2014; Rismani et al., 2012; Soin et al., 2012; Yeo et al., 2015; Yeo et al., 2014).

The presence of an additional peak at 283.3 ± 0.2 eV (Ferrari, 2004a; Ong et al., 2007) has been observed only in samples 5SiC10, 10SiC10, 5SiN_xC10 and 10SiN_xC10, which was assigned to C-Si bonding. In contrast, sp^2 carbon-nitride bonding assigned to $\text{sp}^2\text{C-N}$ at 286.7 ± 0.2 eV and sp^3 carbon-nitride bonding assigned to $\text{sp}^3\text{C-N}$ at 287.7 ± 0.2 eV (McCann et al., 2005; Yamamoto et al., 2001) have been detected only in samples 5SiN_xC10 and 10SiN_xC10. The formation of C-Si and C-N can be attributed to the interaction of C^+ ions with Si or SiN_x interlayer at *Si/ta*-C or SiN_x/ta -C interface. In meantime in 5SiN_xC10 and 10SiN_xC10 sample found C=O bonding shifted ~ 0.6 eV to higher binding energies corresponding to higher oxidation state.

The areas under the constituent peaks in all of the core level spectra derived for all of the samples were compared using the area ratio method, which compares the areas under the constituent peaks in the $C1s$ core level spectra. The $C1s$ core level spectra of composite $ta-C$, $Si/ta-C$, and $SiN_x/ta-C$ films shown in Table 5.2 are influenced by the chemical bonding and binding energies associated with the bonding configurations. As revealed by the XPS results, the introduction of the 0.5-1.0 nm Si and SiN_x interlayer between carbon and NiFe substrate causes a significant change in the chemical bonding of the $ta-C$ film by increasing the content of interfacial bonding between the $ta-C$ film and interlayer, increasing the sp^3C bonding fraction, and decreasing the amount of oxidation ($C-O$ and $C=O$) in $ta-C$ film. The bonding the fraction information, it was discovered that in terms of carbon bonding, increasing Si and SiN_x interlayer 0.5-1.0 nm thickness while keeping constant $ta-C$ thickness at 1.0 nm illustrates that sp^3 fraction or $sp^3C/(sp^3C+sp^2C)$ ratio increase as a function of interlayer thickness as shown in Figure 4.18. When compared without interlayer thickness or monolithic $ta-C$ film. The presence of Si and SiN_x interlayer enhanced the sp^3 bonding with the carbon layer.

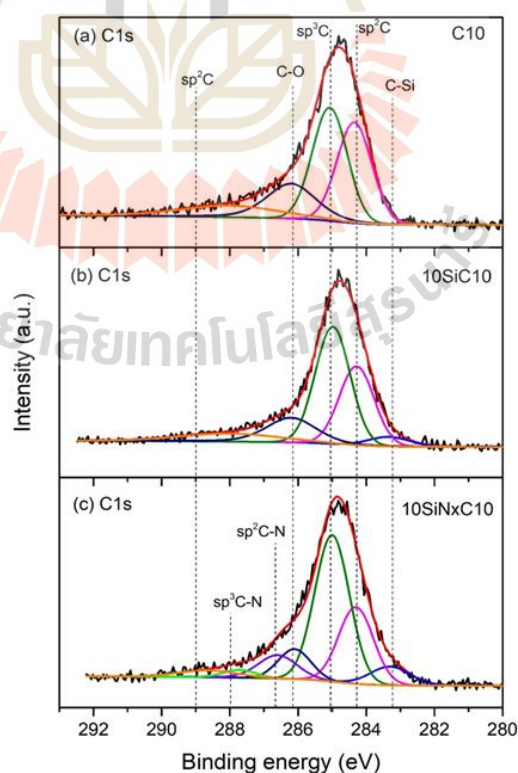


Figure 4.17 High resolution $C1s$ core level XPS spectra of as-deposited samples (a) $C10$, (b) $10SiC10$, and (c) $10SiN_xC10$.

Table 4.4 Chemical bonding and binding energies of the C bonding configurations for composite Si/*ta*-C and SiN_x/*ta*-C films.

Sample	Atomic concentration (at%)							
	Bond	C-Si	sp ² C	sp ³ C	C – O	sp ² C-N	sp ³ C-N	C=O
	B.E (eV)	283.3	284.2	284.9	286.2	286.7	287.7	288.0
C10		0	32.6	36.4	18.6	0	0	12.5
5SiC10		2.4	29.6	36.7	20.9	0	0	10.4
10SiC10		4.3	29.1	43.0	14.7	0	0	8.9
5SiN _x C10		3.5	28.4	39.4	10.7	11.1	1.1	5.8
10SiN _x C10		6.86	24.9	44.5	8.5	9.5	2.2	3.7

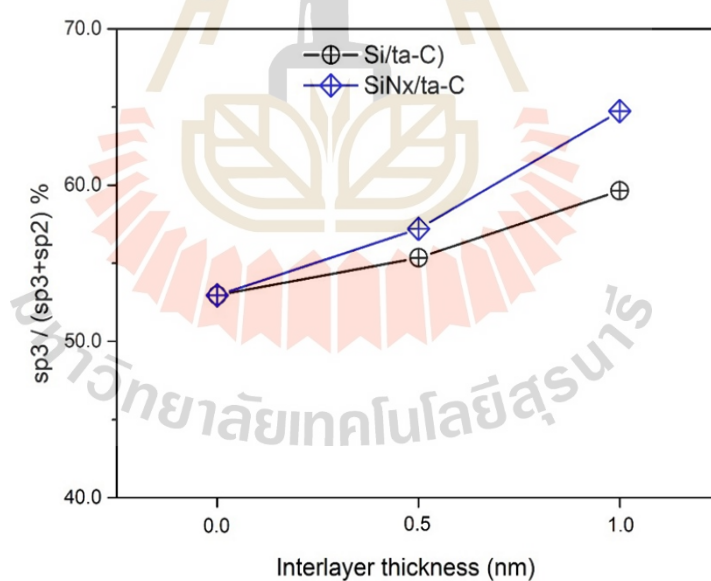


Figure 4.18 Relationship of sp³C/(sp³C+sp²C) fraction deconvoluted of C1s core level spectra of Si and SiN_x interlayer thickness overcoat with *ta*-C film.

Table 4.5 Binding energies (B.E) and associated atomic percentage in the Si and SiN_x interlayer XPS Si2p spectra.

Peak in Si interlayer	Si-Si	Si-C	Si-N	Si-O-C	Si-N-O /Si-O	SiO _x
BE (eV)	99.60	100.60	101.50	102.20	102.90	103.30
10SiC10	35.82	35.87	0	16.87	0	11.43
10SiN _x C10	19.80	21.53	38.24	0	20.44	0

To have a more profound knowledge of the interfacial bonding between carbon with silicon and carbon with nitrogen, the deconvoluted Si2p core level spectra of samples 10SiC10 and 10SiN_xC10 were analyzed using a variety of Gaussian-Lorentzian distributions correlating to the possible bonding sites within the interlayer region, i.e., Si-Si, Si-C, Si-O-C, SiO_x, Si-N, and Si-N-O. The approximated atomic fraction and bonding energy position for each peak are shown in Table 4.5.

Figure 4.21(a) represents the deconvolution of the Si2p core level spectrum of sample 10SiC10 (Si-interlayer with 1 nm *ta*-C thickness), which includes two notable peaks 99.7 eV and 100.6 eV, which are related to the Si element (Si-Si), silicon-carbide (Si-C), respectively (Gallis et al., 2005; Wang et al., 2004). According to the findings, about the Si atoms in the interlayer interacted with the C⁺ ions, resulting in the formation of the projected Si-C bonds. It was discovered that the Si2p spectrum of sample 10SiC10 also contained two minor peaks at higher binding energies of about 102.20 eV and 103.30 eV, which were designated to Silicon-Oxycarbide (Si-O-C) (Choi et al., 1998; Dwivedi et al., 2014; Önnby et al., 1997; Wang et al., 2004) and Si-O bonds (Choi et al., 1998; Liu et al., 2013), respectively. The presence of SiO_x related to the fact that during sputter etching and before to deposition of *ta*-C, silicon oxide was left behind in the structure of the interlayer, resulting in SiO_x bonds. Si-O-C bonds may be formed by C⁺ radicals reacting with these residuals. As a result of the interaction between the C⁺ ions, the Si interlayer, and the substrate, then SiO_x and Si-O-C bonds were most likely formed (Rismani et al., 2012). The deconvoluted Si2p peak of the sample 10SiN_xC10 (SiN_x-interlayer with 1 nm *ta*-C thickness), as shown in Figure 4.19(b), the presence of a strong Si-N peak and a dominant Si-C peak indicated that the interlayer of sample 10SiN_xC10 was largely composed of Si-N and Si-C bonds.

XPS analyses indicate that the incorporation of Si and SiN_x interlayers significantly alters the microstructure of the *ta*-C film by increasing the amount of interfacial bonding between the *ta*-C film and underlayers, such as Si-C bonding and C-N bonding, as well as by expanding the sp³ bonding content and decreasing the amount of oxidation in the *ta*-C film. As shown in Table 4.4 and Figure 4.19, the sp³C bonding fraction of PFCVA-deposited carbon films with and without the SiN_x and Si interlayers while maintaining the thickness of the *ta*-C films is significantly different in sp³ contents as 10SiN_xC10 > 10SiC10 > 5SiN_xC10 > 5SiC10 > C10, indicating a significant difference between the patterns. The results reveal that interlayer thickness has an effect on sp³C content, which reflects tribological performance by decreasing COF, which is consistent with the outcomes of the wear ball-on-disk experiment and I_D/I_G ratio Raman analysis shown in Figure 4.18. The results shown above are congruent with those obtained by Yeo et al. and Liu et al. in their respective studies (Liu et al., 2013; Yeo et al., 2014).

In summary, it is clear that the incorporation of a Si and SiN_x interlayer between the NiFe substrate and the *ta*-C film boosts the sp³ carbon bonding within the *ta*-C film while decreasing the sp² carbon clustering within the *ta*-C film, as demonstrated by wear ball-on-disk testing, Raman and XPS spectra. Additionally, the interlayer thickness of SiN_x material is more effective at increasing sp³C concentrations than the Si material.

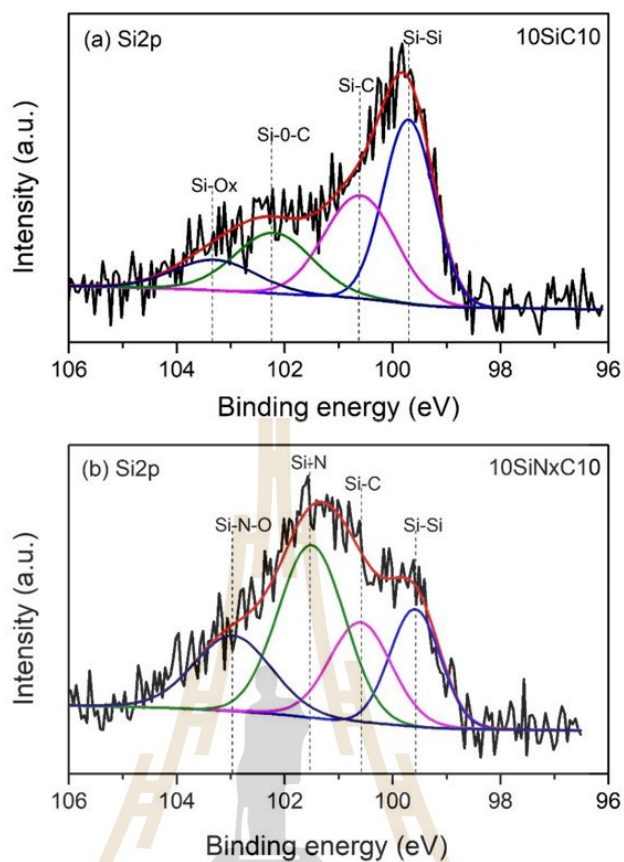


Figure 4.19 Deconvolution of Si_{2p} XPS spectra with Gaussian-Lorentzian of Si and SiN_x interlayer (a) 10SiC₁₀ and (b) 10SiN_xCl₀ with 1.0 nm *ta*-C overcoat.

CHAPTER V

CONCLUSIONS AND SUGGESTIONS FOR FUTURE WORK

This research work has been made to divide the essential conclusion of this Ph.D. thesis into two major sections, which are as follows:

The primary objective of this research was to investigate the structural characterization of ultrathin tetrahedral amorphous carbon overcoats for use in high area density magnetic recording. In recent works, the study results were reported, including a comprehensive investigation of the chemical structure of ultrathin *ta*-C overcoats with thicknesses ranging from 0.5 nm to 5.0 nm. In order to produce the *ta*-C overcoats, the IBD approach was applied to a NiFe alloy base substrate with a Si interlayer, followed by the PFCVA technique. This study determined overcoat thicknesses with precision using the WDXRF and HRTEM techniques, respectively. The surface morphology and chemical structure of the samples were investigated using a variety of techniques, including AFM, XPS, NEXAFS, and Raman spectroscopy. Aside from that, the reciprocating wear test was utilized to determine the tribological properties of the materials under examination. The AFM tests revealed that the synthesized ultrathin *ta*-C coating had an ultrasmooth surface with an R_q of less than 0.23 nm, indicating that PFCVA successfully fabricated an ultrathin *ta*-C film with a high level of efficiency. According to the results of the XPS examination, the overcoat had a high sp^3 bond fraction, with a range of 55.36-76.29% in the area of the investigation. Following the findings of the NEXAFS and Raman spectroscopy investigations, it was discovered that the sp^2 bonds fraction and I_D/I_G ratio increased with decreasing overcoat thickness and then increased rapidly when the overcoat thickness reached 1 nm. As a result, the value of COF increased. It is feasible to explain the relationship between the sp^2 bonds fraction and the total overcoat thickness using the subplantation model. The acquired results demonstrate that the PFCVA process when

used as a protective coating for high-density magnetic storage devices, limits the thickness of the *ta*-C overcoat that may be generated.

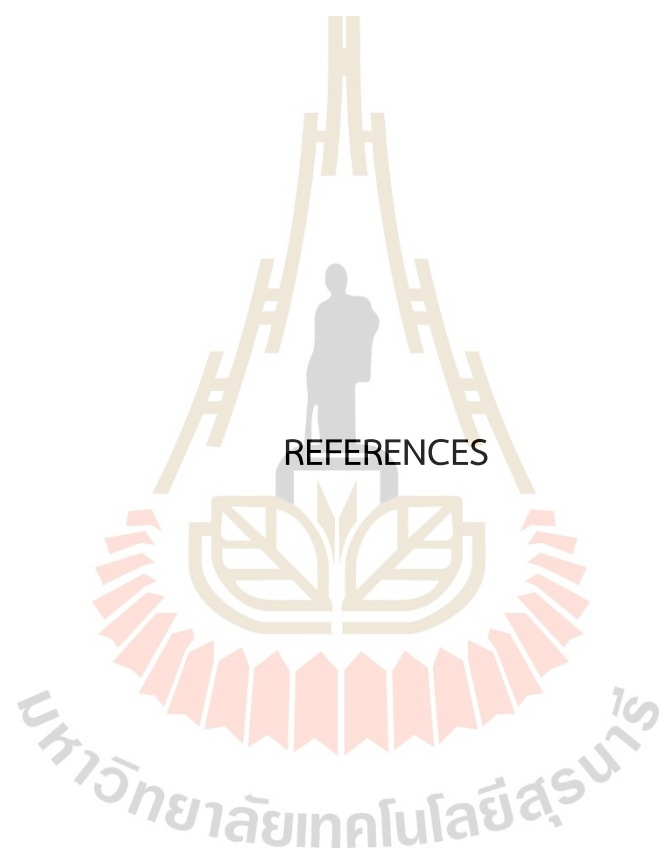
The secondary the influence of thin Si and SiN_x interlayer thickness on the structure of an ultrathin *ta*-C film has been investigated in this study. Through the use of sputtering, the interlayers of Si and SiN_x are deposited at varied thicknesses from 0.5 to 1.0 nm, followed by 1.0 nm of PFCVA deposited *ta*-C on top of the Si and SiN_x layers. The Si/*ta*-C and SiN_x/*ta*-C bilayer have a similar topographical scale and a smooth rough surface morphology. As far as tribological properties are tested on ball-on-disk, monolithic Si and SiN_x exhibit poor COF performance. On the contrary, bilayer Si/C and SiN_x exhibit enhanced tribological capabilities and a reduced COF, even when compared to monolithic *ta*-C 1.0 nm. It is crucial to highlight that the presence of SiN_x interlayer thickness can result in effective COF as a function of interlayer thickness.

Using Raman analysis, it was revealed that the I_D/I_G ratio reduced as the interlayer thickness of Si and SiN_x increased from 0.5-1.0 nm, even though the *ta*-C thickness remained constant with increasing interlayer thickness, corroborates with XPS results. The XPS analysis of the chemical composition of the *ta*-C film reveals that the Si and C-N bonding has transformed into Si-C bonding and Si-N bonding, especially depositing an interfacial SiN_x layer between the *ta*-C film and the NiFe substrate. As a result, evidence of an adhesive layer formed between the carbon overcoat and the interlayer can be found. When applied to a NiFe substrate, the advantage of SiN_x is that it acts as a protective layer, preventing the migration of water and oxygen from the NiFe substrate through the *ta*-C film. As a result, there is less oxidation in *ta*-C films, which indicates that sp³C bonding is being promoted. Considering how well the interlayer and benefit SiN_x contribute to the rise in sp³C content, it represents a promising potential candidate for producing great tribology, which is an important consideration when designing a high-density magnetic recording system with appropriate *ta*-C architecture.

Alternated carbon overcoat is utilized as a protective surface coating for magnetic storage technologies, such as HDD drives, which are positioned to benefit in the near future from the expanding demand for digital data storage due to its excellent

storage performance and inexpensive cost. However, significant efforts to develop existing HDD drive technology are still required to boost the areal densities in these systems beyond the scope of this study. The primary purpose of this research was to use *ta*-C films deposited with the FCVA technology, which can be investigated in ultrathin *ta*-C film, and to investigate the tribological behavior of the generated coating. Due to the effect of humidity, we are unable to assess wear resistance accurately.

Further investigation can be undertaken to explore the wear test in an oxygen-free environment that must be designed with and without humidity. This can be achieved by flushing or purging the test chamber with an inert gas, such as nitrogen or argon. Due to the inert and dry condition testing, neither oxygen nor water will be present to alter the surface dangling bonds. After the wear tests have been completed, the process can be repeated in the presence of water, and the surface can be inspected. By comparing the results of these two trials to those of the current study, it is feasible to identify whether the wear is caused by surface oxidation or adhesion. In the future, however, additional research can be conducted on the effect of oxidation on the wear of the writer-reader, which is covered by *ta*-C coatings at the head-disk interface.



REFERENCES

REFERENCES

- Abbas, G. A., Roy, S. S., Papakonstantinou, P. and McLaughlin J. A. (2005). Structural investigation and gas barrier performance of diamond-like carbon-based films on polymer substrates. *Carbon*, 43(2), 303-309.
- Aisenberg, S. and Chabot, R. (1971). Ion-Beam Deposition of Thin Films of Diamondlike Carbon. *Journal of applied physics*, 42(7), 2953-2958.
- Al Mahmud, K. A. H., Varman, M., Kalam, M. A., Masjuki, H. H., Mobarak, H. M. and Zulkifli, N. W. M. (2014). Tribological characteristics of amorphous hydrogenated (a-C:H) and tetrahedral (ta-C) diamond-like carbon coating at different test temperatures in the presence of commercial lubricating oil. *Surface and Coatings Technology*, 245, 133-147.
- Albrecht, T. R., Arora, H., Ayanoor-Vitikkate, V., Beaujour, J.-M., Bedau, D., Berman, D. and Dobisz, E. E. (2015). Bit-patterned magnetic recording: Theory, media fabrication, and recording performance. *IEEE Transactions on Magnetics*, 51(5), 1-42.
- Anders, A., Fong, W., Kulkarni, A. V., Ryan, F. W. and Bhatia, C. S. (2001). Ultrathin diamond-like carbon films deposited by filtered carbon vacuum arcs. *IEEE transactions on plasma science*, 29(5), 768-775.
- Anders, S., Ager III, J. W., Pharr, G. M., Tsui, T. Y. and Brown, I. G. (1997). Heat treatment of cathodic arc deposited amorphous hard carbon films. *Thin Solid Films*, 308, 186-190.
- Anders, S., Callahan, D. L., Pharr, G. M., Tsui, T. Y. and Bhatia, C. S. (1997). Multilayers of amorphous carbon prepared by cathodic arc deposition. *Surface and Coatings Technology*, 94, 189-194.

- ASTC. (2014). Advanced Storage Industry Consortium (ASTC). (2014). ASTC Technology Roadmap 2014 v8 [Online]. Available: Retrieved from http://www.idema.org/?page_id=2269.
- Baker Jr, B. B. and Kasprzak, D. J. (1993). Thermal degradation of commercial fluoropolymers in air. *Polymer degradation and stability*, 42(2), 181-188.
- Beghi, M. G., Ferrari, A. C., Teo, K. B. K., Robertson, J., Bottani, C. E., Libassi, A. and Tanner, B. K. (2002). Bonding and mechanical properties of ultrathin diamond-like carbon films. *Applied physics letters*, 81(20), 3804-3806.
- Bewilogua, K. and Hofmann, D. (2014). History of diamond-like carbon films-from first experiments to worldwide applications. *Surface and Coatings Technology*, 242, 214-225.
- Bhatia, C. S., Fong, W., Chen, C.-Y., Wei, J., Bogoy, D. B., Anders, S. and Stohr, J. (1999). Tribo-chemistry at the head/disk interface. *IEEE Transactions on Magnetics*, 35(2), 910-915.
- Bian, J., Song, Z., Zhang, Y. and Cheng, C. (2019). NiCoP nanopeapods embedded in carbon nanotube arrays as bifunctional catalysts for efficient overall water splitting. *Materials Today Nano*, 8, 100053.
- Binnig, G., Quate, C. F. and Gerber, C. (1986). Atomic force microscope. *Physical review letters*, 56(9), 930.
- Birrell, J., Gerbi, J., Auciello, O., Gibson, J., Gruen, D. and Carlisle, J. (2003). Bonding structure in nitrogen doped ultrananocrystalline diamond. *Journal of applied physics*, 93(9), 5606-5612.
- Bootkul, D., Supsermpol, B., Saenphinit, N., Aramwit, C. and Intarasiri, S. (2014). Nitrogen doping for adhesion improvement of DLC film deposited on Si substrate by Filtered Cathodic Vacuum Arc (FCVA) technique. *Applied Surface Science*, 310, 284-292.
- Brouwer, P. (2006). Theory of XRF. Almelo, Netherlands: PANalytical BV.

- Carpick, R. W. and Salmeron, M. (1997). Scratching the surface: fundamental investigations of tribology with atomic force microscopy. *Chemical reviews*, 97(4), 1163-1194.
- Casiraghi, C., Ferrari, A., Ohr, R., Chu, D. and Robertson, J. (2004). Surface properties of ultra-thin tetrahedral amorphous carbon films for magnetic storage technology. *Diamond and related materials*, 13(4-8), 1416-1421.
- Casiraghi, C., Ferrari, A., Ohr, R., Flewitt, A., Chu, D. and Robertson, J. (2003). Dynamic roughening of tetrahedral amorphous carbon. *Physical review letters*, 91(22), 226104.
- Casiraghi, C., Ferrari, A. and Robertson, J. (2005). The smoothness of tetrahedral amorphous carbon. *Diamond and related materials*, 14(3-7), 913-920.
- Casiraghi, C., Ferrari, A. C., Robertson, J., Ohr, R., Gradowski, M. v., Schneider, D. and Hilgers, H. (2004). Ultra-thin carbon layer for high density magnetic storage devices. *Diamond and related materials*, 13(4-8), 1480-1485.
- Casiraghi, C., Robertson, J. and Ferrari, A. C. (2007). Diamond-like carbon for data and beer storage. *Materials today*, 10(1-2), 44-53.
- Cemin, F., Bim, L., Menezes, C., da Costa, M. M., Baumvol, I., Alvarez, F. and Figueroa, C. (2015). The influence of different silicon adhesion interlayers on the tribological behavior of DLC thin films deposited on steel by EC-PECVD. *Surface and Coatings Technology*, 283, 115-121.
- Chen, C.-Y., Fong, W., Bogy, D. B. and Bhatia, C. S. (2000). Initiation of lubricant catalytic decomposition by hydrogen evolution from contact sliding on CH_x and CN_x overcoats. *Tribology Letters*, 8(1), 25-34.
- Chen, K.-W. and Lin, J.-F. (2009). The study of adhesion and nanomechanical properties of DLC films deposited on tool steels. *Thin Solid Films*, 517(17), 4916-4920.

- Chen, Q., Zeng, C., Xu, M., Yuan, H., Lv, H., Wang, Z. and Wang, X. (2019). Effect of SiN_x interlayer thickness on adhesion and friction properties of diamond-like carbon films. *Diamond and related materials*, 94, 186-193.
- Chen, Z., Zhao, J., Yano, T., Ooie, T., Yoneda, M. and Sakakibara, J. (2000). Observation of sp^3 bonding in tetrahedral amorphous carbon using visible Raman spectroscopy. *Journal of applied physics*, 88(5), 2305-2308.
- Chhowalla, M., Robertson, J., Chen, C., Silva, S., Davis, C., Amaratunga, G. and Milne, W. (1997). Influence of ion energy and substrate temperature on the optical and electronic properties of tetrahedral amorphous carbon (ta-C) films. *Journal of applied physics*, 81(1), 139-145.
- Choi, W., Ong, T., Tan, L., Loh, F. and Tan, K. (1998). Infrared and x-ray photoelectron spectroscopy studies of as-prepared and furnace-annealed radio-frequency sputtered amorphous silicon carbide films. *Journal of applied physics*, 83(9), 4968-4973.
- Chu, P. K. and Li, L. (2006). Characterization of amorphous and nanocrystalline carbon films. *Materials Chemistry and Physics*, 96(2-3), 253-277.
- Cramer, S., Eccles, T., Kutzler, F., Hodgson, K. O. and Mortenson, L. (1976). Molybdenum x-ray absorption edge spectra. The chemical state of molybdenum in nitrogenase. *Journal of the American Chemical Society*, 98(5), 1287-1288.
- Cuomo, J. J., Pappas, D. L., Lossy, R., Doyle, J. P., Bruley, J., Di Bello, G. W. and Krakow, W. (1992). Energetic carbon deposition at oblique angles. *Journal of Vacuum Science & Technology A: Vacuum, Surfaces, and Films*, 10(6), 3414-3418.
- Davis, C., Amaratunga, G. and Knowles, K. (1998). Growth mechanism and cross-sectional structure of tetrahedral amorphous carbon thin films. *Physical review letters*, 80(15), 3280.

- DeLongchamp, D. M., Lin, E. K. and Fischer, D. A. (2005). Organic semiconductor structure and chemistry from near-edge X-ray absorption fine structure (NEXAFS) spectroscopy. Paper presented at the Organic Field-Effect Transistors IV.
- Dienwiebel, M. and Bouchet, M. -I. D. B. (2018). Advanced analytical methods in tribology: Springer.
- Dischler, B., Bubenzer, A. and Koidl, P. (1983). Bonding in hydrogenated hard carbon studied by optical spectroscopy. *Solid State Communications*, 48(2), 105-108.
- Donnet, C. and Erdemir, A. (2007). Tribology of diamond-like carbon films: fundamentals and applications: Springer Science & Business Media.
- Donnet, C., Fontaine, J., Grill, A. and Le Mogne, T. (2001). The role of hydrogen on the friction mechanism of diamond-like carbon films. *Tribology Letters*, 9(3), 137-142.
- Dwivedi, N., Ott, A., Sasikumar, K., Dou, C., Yeo, R., Narayanan, B. and Dutta, T. (2021). Graphene overcoats for ultra-high storage density magnetic media. *Nature communications*, 12(1), 1-13.
- Dwivedi, N., Rismani-Yazdi, E., Yeo, R. J., Goohpattader, P. S., Satyanarayana, N., Srinivasan, N. and Bhatia, C. (2014). Probing the role of an atomically thin SiN_x interlayer on the structure of ultrathin carbon films. *Scientific reports*, 4(1), 1-10.
- Dwivedi, N., Satyanarayana, N., Yeo, R. J., Xu, H., Loh, K. P., Tripathy, S. and Bhatia, C. S. (2015). Ultrathin carbon with interspersed graphene/fullerene-like nanostructures: a durable protective overcoat for high density magnetic storage. *Scientific reports*, 5(1), 1-16.
- Dwivedi, N., Yeo, R. J., Satyanarayana, N., Kundu, S., Tripathy, S. and Bhatia, C. (2015). Understanding the role of nitrogen in plasma-assisted surface modification of

- magnetic recording media with and without ultrathin carbon overcoats. *Scientific reports*, 5(1), 1-13.
- Ean, Y. C., Jang, Y.-J., Kim, J.-K., Hsien, W. L. Y., Siambun, N. J. and Kim, S.-S. (2017). Effect of substrate bias on the tribological behavior of ta-C coating prepared by filtered cathodic vacuum arc. *International Journal of Precision Engineering and Manufacturing*, 18(5), 779-784.
- Endler, I., Leonhardt, A., Scheibe, H.-J. and Born, R. (1996). Interlayers for diamond deposition on tool materials. *Diamond and related materials*, 5(3-5), 299-303.
- Erdemir, A. and Donnet, C. (2006). Tribology of diamond-like carbon films: recent progress and future prospects. *Journal of Physics D: Applied Physics*, 39(18), R311.
- Erdemir, A., Eryilmaz, O. and Fenske, G. (2000). Synthesis of diamondlike carbon films with superlow friction and wear properties. *Journal of Vacuum Science & Technology A: Vacuum, Surfaces, and Films*, 18(4), 1987-1992.
- Erdemir, A., Eryilmaz, O., Nilufer, I. and Fenske, G. (2000). Effect of source gas chemistry on tribological performance of diamond-like carbon films. *Diamond and related materials*, 9(3-6), 632-637.
- Fallon, P., Veerasamy, V., Davis, C., Robertson, J., Amaratunga, G., Milne, W. and Koskinen, J. (1993). Properties of filtered-ion-beam-deposited diamondlike carbon as a function of ion energy. *Physical review B*, 48(7), 4777.
- Fallon, P. J., Veerasamy, V. S., Davis, C. A., Robertson, J., Amaratunga, G. A., Milne, W. I. and Koskinen, J. (1993). Properties of filtered-ion-beam-deposited diamondlike carbon as a function of ion energy. *Phys Rev B Condens Matter*, 48(7), 4777-4782.
- FC, T. and SL, T. (2006). Correlation between ID/IG ratio from visible raman spectra and sp^2/sp^3 ratio from XPS spectra of annealed hydrogenated DLC film. *Materials transactions*, 47(7), 1847-1852.

- Fedoseeva, Y. V., Pozdnyakov, G., Okotrub, A., Kanygin, M., Nastaushev, Y. V., Vilkov, O. and Bulusheva, L. (2016). Effect of substrate temperature on the structure of amorphous oxygenated hydrocarbon films grown with a pulsed supersonic methane plasma flow. *Applied Surface Science*, 385, 464-471.
- Ferrari, A., Kleinsorge, B., Morrison, N., Hart, A., Stolojan, V. and Robertson, J. (1999). Stress reduction and bond stability during thermal annealing of tetrahedral amorphous carbon. *Journal of applied physics*, 85(10), 7191-7197.
- Ferrari, A., Libassi, A., Tanner, B., Stolojan, V., Yuan, J., Brown, L. and Robertson, J. (2000). Density, sp^3 fraction, and cross-sectional structure of amorphous carbon films determined by X-ray reflectivity and electron energy-loss spectroscopy. *Physical review B*, 62(16), 11089.
- Ferrari, A. C. (2002). Determination of bonding in diamond-like carbon by Raman spectroscopy. *Diamond and related materials*, 11(3-6), 1053-1061.
- Ferrari, A. C. (2004). Diamond-like carbon for magnetic storage disks. *Surface and Coatings Technology*, 180, 190-206.
- Ferrari, A. C. and Robertson, J. (2000). Interpretation of Raman spectra of disordered and amorphous carbon. *Physical review B*, 61(20), 14095.
- Ferrari, A. C. and Robertson, J. (2001). Resonant Raman spectroscopy of disordered, amorphous, and diamondlike carbon. *Physical review B*, 64(7).
- Ferrari, A. C., Robertson, J., Beghi, M. G., Bottani, C. E., Ferulano, R. and Pastorelli, R. (1999). Elastic constants of tetrahedral amorphous carbon films by surface Brillouin scattering. *Applied physics letters*, 75(13), 1893-1895.
- Gago, R., Vinnichenko, M., Jäger, H., Belov, A. Y., Jiménez, I., Huang, N. and Maitz, M. (2005). Evolution of sp^2 networks with substrate temperature in amorphous carbon films: Experiment and theory. *Physical review B*, 72(1), 014120.
- Gallis, S., Huang, M., Efstathiadis, H., Eisenbraun, E., Kaloyeros, A. E., Nyein, E. E. and Hommerich, U. (2005). Photoluminescence in erbium doped amorphous silicon oxycarbide thin films. *Applied physics letters*, 87(9), 091901.

- Gangopadhyay, A. and Tamor, M. (1993). Friction and wear behavior of diamond films against steel and ceramics. *Wear*, 169(2), 221-229.
- García, J. A., Rivero, P. J., Barba, E., Fernández, I., Santiago, J. A., Palacio, J. F. and Rodríguez, R. J. (2020). A Comparative Study in the Tribological Behavior of DLC Coatings Deposited by HiPIMS Technology with Positive Pulses. *Metals*, 10(2), 174.
- Garcia, R. and Perez, R. (2002). Dynamic atomic force microscopy methods. *Surface science reports*, 47(6-8), 197-301.
- Giessibl, F. J. (2003). Advances in atomic force microscopy. *Reviews of modern physics*, 75(3), 949.
- Goohpattader, P. S., Dwivedi, N., Rismani-Yazdi, E., Satyanarayana, N., Yeo, R. J., Kundu, S. and Bhatia, C. S. (2015). Probing the role of C⁺ ion energy, thickness and graded structure on the functional and microstructural characteristics of ultrathin carbon films (< 2 nm). *Tribology International*, 81, 73-88.
- Gradowski, M., Ferrari, A., Ohr, R., Jacoby, B., Hilgers, H., Schneider, H.-H. and Adrian, H. (2003). Resonant Raman characterisation of ultra-thin nano-protective carbon layers for magnetic storage devices. *Surface and Coatings Technology*, 174, 246-252.
- Grossman, E., Lempert, G., Kulik, J., Marton, D., Rabalais, J. and Lifshitz, Y. (1996). Role of ion energy in determination of the sp³ fraction of ion beam deposited carbon films. *Applied physics letters*, 68(9), 1214-1216.
- Gurman, S. (1995). Interpretation of EXAFS data. *Journal of synchrotron radiation*, 2(1), 56-63.
- Hemraj-Benny, T., Banerjee, S., Sambasivan, S., Balasubramanian, M., Fischer, D. A., Eres, G. and Han, W. (2006). Near-edge X-ray absorption fine structure spectroscopy as a tool for investigating nanomaterials. *small*, 2(1), 26-35.
- Herrera-Gomez, A., Aguirre-Tostado, F., Sun, Y., Contreras-Guerrero, R., Wallace, R., Hisao, Y. and Flint, E. (2007). Quantification of pinhole density in ultrathin

- diamond-like carbon films. *Surface and Interface Analysis*, 39(12-13), 904-907.
- Huang, L., Hou, Y., Yu, Z., Peng, Z., Wang, L., Huang, J. and Li, Z. (2017). Pt/Fe-NF electrode with high double-layer capacitance for efficient hydrogen evolution reaction in alkaline media. *International Journal of Hydrogen Energy*, 42(15), 9458-9466.
- Huang, Y., Xiao, H., Ma, Z., Wang, J. and Gao, P. (2007). Effects of Cu and Cu/Ti interlayer on adhesion of diamond film. *Surface and Coatings Technology*, 202(1), 180-184.
- Hüfner, S. (2013). Photoelectron spectroscopy: principles and applications: Springer Science & Business Media.
- IDC. (2021). IDC Forecasts Solid Growth for the Hard Disk Drive and Solid State Drive Markets to Meet Increasing Demand for Data Storage Capacity. Retrieved from <https://www.idc.com/getdoc.jsp?containerId=prUS47975921>
- Inaba, H., Furusawa, K., Hirano, S., Sasaki, S., Todoroki, S., Yamasaka, M. and Endou, M. (2003). Tetrahedral amorphous carbon films by filtered cathodic vacuum-arc deposition for air-bearing-surface overcoat. *Japanese Journal of Applied Physics*, 42(5R), 2824.
- Ismail, K. and Ismail, K. (2015). Fabrication and characterisation of SERS substrates through photo-deposition of Gold Nanoparticles. no. November, 0-36.
- Jelínek, M., Smetana, K., Kocourek, T., Dvoránková, B., Zemek, J., Remsa, J. and Luxbacher, T. (2010). Biocompatibility and sp^3/sp^2 ratio of laser created DLC films. *Materials Science and Engineering: B*, 169(1-3), 89-93.
- Jeon, Y., Park, Y. S., Kim, H. J., Hong, B. and Choi, W. S. (2007). Tribological properties of ultrathin DLC films with and without metal interlayers. *JOURNAL-KOREAN PHYSICAL SOCIETY*, 51(3), 1124.
- Jiang, J. and Arnell, R. (2000). The effect of substrate surface roughness on the wear of DLC coatings. *Wear*, 239(1), 1-9.

- Jiang, J., Meng, W., Evans, A. and Cooper, C. (2003). Structure and mechanics of W-DLC coated spur gears. *Surface and Coatings Technology*, 176(1), 50-56.
- Johnston, S. and Hainsworth, S. V. (2005). Effect of DLC coatings on wear in automotive applications. *Surface engineering*, 21(1), 67-71.
- Kalin, M. and Vižintin, J. (2005). The tribological performance of DLC-coated gears lubricated with biodegradable oil in various pinion/gear material combinations. *Wear*, 259(7-12), 1270-1280.
- Kano, M. (2006). Super low friction of DLC applied to engine cam follower lubricated with ester-containing oil. *Tribology International*, 39(12), 1682-1685.
- Kasai, P. H. (1992). Perfluoropolyethers: intramolecular disproportionation. *Macromolecules*, 25(25), 6791-6799.
- Kennedy, M., Hoppe, S. and Esser, J. (2014). Lower friction losses with new piston ring coating. *MTZ worldwide*, 75(4), 24-29.
- Kief, M. and Victora, R. (2018). Materials for heat-assisted magnetic recording. *MRS Bulletin*, 43(2), 87-92.
- Koningsberger, D., Mojet, B., Van Dorssen, G. and Ramaker, D. (2000). XAFS spectroscopy; fundamental principles and data analysis. *Topics in catalysis*, 10(3), 143-155.
- Koningsberger, D. and Prins, R. (1988). X-ray absorption: principles, applications, techniques of EXAFS, SEXAFS, and XANES.
- Koshigan, K. D., Mangolini, F., McClimon, J. B., Vacher, B., Bec, S., Carpick, R. W. and Fontaine, J. (2015). Understanding the hydrogen and oxygen gas pressure dependence of the tribological properties of silicon oxide-doped hydrogenated amorphous carbon coatings. *Carbon*, 93, 851-860.
- Koskinen, J., Hirvonen, J.-P. and Keränen, J. (1998). Effect of deposition temperature and growth rate on the bond structure of hydrogen free carbon films. *Journal of applied physics*, 84(1), 648-650.

- Kulik, J., Lempert, G., Grossman, E., Marton, D., Rabalais, J. and Lifshitz, Y. (1995). sp^3 content of mass-selected ion-beam-deposited carbon films determined by inelastic and elastic electron scattering. *Physical review B*, 52(22), 15812.
- Latham, K. G., Simone, M. I., Dose, W. M., Allen, J. A. and Donne, S. W. (2017). Synchrotron based NEXAFS study on nitrogen doped hydrothermal carbon: Insights into surface functionalities and formation mechanisms. *Carbon*, 114, 566-578.
- Lau, W., Bello, I., Feng, X., Huang, L., Fuguang, Q., Zhenyu, Y. and Lee, S. T. (1991). Direct ion beam deposition of carbon films on silicon in the ion energy range of 15-500 eV. *Journal of applied physics*, 70(10), 5623-5628.
- Li, X., Ke, P., Zheng, H. and Wang, A. (2013). Structural properties and growth evolution of diamond-like carbon films with different incident energies: A molecular dynamics study. *Applied Surface Science*, 273, 670-675.
- Li, Y., Tang, Y., Yang, Q., Xiao, C. and Hirose, A. (2010). Growth and adhesion failure of diamond thin films deposited on stainless steel with ultra-thin dual metal interlayers. *Applied Surface Science*, 256(24), 7653-7657.
- LIBASSI, A. DENSITY AND SP^3 CONTENT IN DIAMOND-LIKE CARBON FILMS BY X-RAY.
- Lifshitz, Y. (1999). Diamond-like carbon-present status. *Diamond and related materials*, 8(8-9), 1659-1676.
- Lifshitz, Y., Kasi, S. and Rabalais, J. (1989). Subplantation model for film growth from hyperthermal species: Application to diamond. *Physical review letters*, 62(11), 1290.
- Lifshitz, Y., Kasi, S., Rabalais, J. and Eckstein, W. (1990). Subplantation model for film growth from hyperthermal species. *Physical review B*, 41(15), 10468.
- Lifshitz, Y., Lempert, G. and Grossman, E. (1994). Substantiation of subplantation model for diamondlike film growth by atomic force microscopy. *Physical review letters*, 72(17), 2753.

- Lifshitz, Y., Lempert, G., Grossman, E., Avigal, I., Uzan-Saguy, C., Kalish, R. and Rabalais, J. (1995). Growth mechanisms of DLC films from C⁺ ions: experimental studies. *Diamond and related materials*, 4(4), 318-323.
- Lifshitz, Y., Lempert, G., Rotter, S., Avigal, I., Uzan-Saguy, C. and Kalish, R. (1993). The influence of substrate temperature during ion beam deposition on the diamond-like or graphitic nature of carbon films. *Diamond and related materials*, 2(2-4), 285-290.
- Liu, D., Benstetter, G., Lodermeier, E. and Vancea, J. (2003). Influence of the incident angle of energetic carbon ions on the properties of tetrahedral amorphous carbon (ta-C) films. *Journal of Vacuum Science & Technology A: Vacuum, Surfaces, and Films*, 21(5), 1665-1670.
- Liu, F.-X. and Wang, Z.-L. (2009). Thickness dependence of the structure of diamond-like carbon films by Raman spectroscopy. *Surface and Coatings Technology*, 203(13), 1829-1832.
- Liu, F.-X., Yao, K.-L. and Liu, Z.-L. (2007). Substrate tilting effect on structure of tetrahedral amorphous carbon films by Raman spectroscopy. *Surface and Coatings Technology*, 201(16-17), 7235-7240.
- Liu, F., Ma, H. and Tang, C. (2013). Si seed layer thickness effect on the structure of ultrathin tetrahedral amorphous carbon films. *Surface and Coatings Technology*, 235, 117-120.
- Liu, L., Lu, F., Tian, J., Xia, S. and Diao, Y. (2019). Electronic and optical properties of amorphous carbon with different sp³/sp² hybridization ratio. *Applied Physics A*, 125(5), 1-10.
- Liu, Y., Erdemir, A. and Meletis, E. (1996a). An investigation of the relationship between graphitization and frictional behavior of DLC coatings. *Surface and Coatings Technology*, 86, 564-568.
- Liu, Y., Erdemir, A. and Meletis, E. (1996). A study of the wear mechanism of diamond-like carbon films. *Surface and Coatings Technology*, 82(1-2), 48-56.

- Liu, Y., Erdemir, A. and Meletis, E. (1997). Influence of environmental parameters on the frictional behavior of DLC coatings. *Surface and Coatings Technology*, 94, 463-468.
- Ma, T., Hu, Y., Wang, H. and Li, X. (2007). Effect of impact angle and substrate roughness on growth of diamondlike carbon films. *Journal of applied physics*, 101(1), 014901.
- Mabuchi, Y., Higuchi, T. and Weihnacht, V. (2013). Effect of sp^2/sp^3 bonding ratio and nitrogen content on friction properties of hydrogen-free DLC coatings. *Tribology International*, 62, 130-140.
- Mangolini, F., Krick, B. A., Jacobs, T. D., Khanal, S. R., Streller, F., McClimon, J. B. and Ohlhausen, J. A. (2018). Effect of silicon and oxygen dopants on the stability of hydrogenated amorphous carbon under harsh environmental conditions. *Carbon*, 130, 127-136.
- Mangolini, F., Li, Z., Marcus, M. A., Schneider, R. and Dienwiebel, M. (2021). Quantification of the carbon bonding state in amorphous carbon materials: A comparison between EELS and NEXAFS measurements. *Carbon*, 173, 557-564.
- Mangolini, F., McClimon, J. B. and Carpick, R. W. (2016). Quantitative evaluation of the carbon hybridization state by near edge X-ray absorption fine structure spectroscopy. *Analytical chemistry*, 88(5), 2817-2824.
- Mangolini, F., McClimon, J. B., Rose, F. and Carpick, R. W. (2014). Accounting for nanometer-thick adventitious carbon contamination in X-ray absorption spectra of carbon-based materials. *Analytical chemistry*, 86(24), 12258-12265.
- Marchon, B. and Olson, T. (2009). Magnetic spacing trends: from LMR to PMR and beyond. *IEEE Transactions on Magnetics*, 45(10), 3608-3611.
- Marchon, B., Pitchford, T., Hsia, Y.-T. and Gangopadhyay, S. (2013). The head-disk interface roadmap to an areal density of Tbit/in². *Advances in Tribology*, 2013.

- Martin, P. and Bendavid, A. (2001). Review of the filtered vacuum arc process and materials deposition. *Thin Solid Films*, 394(1-2), 1-14.
- Matlak, J. and Komvopoulos, K. (2018). Ultrathin amorphous carbon films synthesized by filtered cathodic vacuum arc used as protective overcoats of heat-assisted magnetic recording heads. *Scientific reports*, 8(1), 1-11.
- McCann, R., Roy, S., Papakonstantinou, P., Ahmad, I., Maguire, P., McLaughlin, J. and Goldoni, A. (2005). NEXAFS study and electrical properties of nitrogen-incorporated tetrahedral amorphous carbon films. *Diamond and related materials*, 14(3-7), 1057-1061.
- McCann, R., Roy, S., Papakonstantinou, P., Bain, M., Gamble, H. and McLaughlin, J. (2005). Chemical bonding modifications of tetrahedral amorphous carbon and nitrogenated tetrahedral amorphous carbon films induced by rapid thermal annealing. *Thin Solid Films*, 482(1-2), 34-40.
- McKenzie, D. R. (1996). Tetrahedral bonding in amorphous carbon. *Reports on Progress in Physics*, 59(12), 1611-1664.
- Mercer, C., Evans, A., Yao, N., Allameh, S. and Cooper, C. (2003). Material removal on lubricated steel gears with W-DLC-coated surfaces. *Surface and Coatings Technology*, 173(2-3), 122-129.
- Merlo, A. M. (2003). The contribution of surface engineering to the product performance in the automotive industry. *Surface and Coatings Technology*, 174, 21-26.
- Moseler, M., Gumbsch, P., Casiraghi, C., Ferrari, A. C. and Robertson, J. (2005). The ultrasoothness of diamond-like carbon surfaces. *Science*, 309(5740), 1545-1548.
- Novotny, V. and Staud, N. (1988). Correlation between environmental and electrochemical corrosion of thin film magnetic recording media. *Journal of The Electrochemical Society*, 135(12), 2931.

- Oguz Er, A., Chen, J. and Rentzepis, P. M. (2012). Ultrafast time resolved x-ray diffraction, extended x-ray absorption fine structure and x-ray absorption near edge structure. *Journal of applied physics*, 112(3), 031101.
- Ong, S.-E., Zhang, S., Du, H. and Sun, D. (2007). Relationship between bonding structure and mechanical properties of amorphous carbon containing silicon. *Diamond and related materials*, 16(8), 1628-1635.
- Önneby, C. and Pantano, C. G. (1997). Silicon oxycarbide formation on SiC surfaces and at the SiC/SiO₂ interface. *Journal of Vacuum Science & Technology A: Vacuum, Surfaces, and Films*, 15(3), 1597-1602.
- Pathem, B. K., Guo, X., Rose, F., Wang, N., Komvopoulos, K., Schreck, E. and Marchon, B. (2013). Carbon Overcoat Oxidation in Heat-Assisted Magnetic Recording. *IEEE Transactions on Magnetics*, 49(7), 3721-3724.
- Pharr, G. M., Callahan, D. L., McAdams, S. D., Tsui, T. Y., Anders, S., Anders, A. and Robertson, J. (1996). Hardness, elastic modulus, and structure of very hard carbon films produced by cathodic-arc deposition with substrate pulse biasing. *Applied physics letters*, 68(6), 779-781.
- PIERSON, H. O. (1993). Handbook of Carbon, Graphite, Diamond and Fullerenes Noyes Publications. Mill Road, Park Ridge NJ, 43, 26.
- Polaki, S., Kumar, N., Madapu, K., Ganesan, K., Krishna, N., Srivastava, S. and Tyagi, A. (2016). Interpretation of friction and wear in DLC film: role of surface chemistry and test environment. *Journal of Physics D: Applied Physics*, 49(44), 445302.
- Polo, M., Andujar, J., Hart, A., Robertson, J. and Milne, W. (2000). Preparation of tetrahedral amorphous carbon films by filtered cathodic vacuum arc deposition. *Diamond and related materials*, 9(3-6), 663-667.
- Praver, S., Nugent, K., Lifshitz, Y., Lempert, G., Grossman, E., Kulik, J. and Kalish, R. (1996). Systematic variation of the Raman spectra of DLC films as a function of sp²: sp³ composition. *Diamond and related materials*, 5(3-5), 433-438.

- Ray, S. C., Pong, W. and Papakonstantinou, P. (2016). Iron, nitrogen and silicon doped diamond like carbon (DLC) thin films: a comparative study. *Thin Solid Films*, 610, 42-47.
- Rismani, E., Samad, M. A., Sinha, S. K., Yeo, R., Yang, H. and Bhatia, C. S. (2012). Ultrathin Si/C graded layer to improve tribological properties of Co magnetic films. *Applied physics letters*, 101(19), 191601.
- Rismani, E., Sinha, S., Yang, H. and Bhatia, C. (2012). Effect of pretreatment of Si interlayer by energetic C⁺ ions on the improved nanotribological properties of magnetic head overcoat. *Journal of applied physics*, 111(8), 084902.
- Robertson, J. (1992). Properties of diamond-like carbon. *Surface and Coatings Technology*, 50(3), 185-203.
- Robertson, J. (1993). Deposition mechanisms for promoting sp³ bonding in diamond-like carbon. *Diamond and related materials*, 2(5-7), 984-989.
- Robertson, J. (2001). Ultrathin carbon coatings for magnetic storage technology. *Thin Solid Films*, 383(1-2), 81-88.
- Robertson, J. (2002). Diamond-like amorphous carbon. *Materials science and engineering: R: Reports*, 37(4-6), 129-281.
- Robertson, J. (2003). Requirements of ultrathin carbon coatings for magnetic storage technology. *Tribology International*, 36(4-6), 405-415.
- Robertson, J. (2005). Mechanism of sp³ bond formation in the growth of diamond-like carbon. *Diamond and related materials*, 14(3-7), 942-948.
- Robertson, J. (2008). Ultrathin carbon coatings for magnetic storage technology. *International Journal of Product Development*, 5(3-4), 321-338.
- Ronkainen, H. and Holmberg, K. (2008). Environmental and thermal effects on the tribological performance of DLC coatings. In *Tribology of diamond-like carbon films* (pp. 155-200): Springer.

- Roy, R. K. and Lee, K. R. (2007). Biomedical applications of diamond-like carbon coatings: a review. *J Biomed Mater Res B Appl Biomater*, 83(1), 72-84.
- Roy, S., McCann, R., Papakonstantinou, P., Maguire, P. and McLaughlin, J. (2005). The structure of amorphous carbon nitride films using a combined study of NEXAFS, XPS and Raman spectroscopies. *Thin Solid Films*, 482(1-2), 145-150.
- Roy, S., McCann, R., Papakonstantinou, P., McLaughlin, J., Kirkman, I., Bhattacharyya, S. and Silva, S. (2006). Near edge X-Ray absorption fine structure study of aligned π -bonded carbon structures in nitrogenated *ta*-C films. *Journal of applied physics*, 99(4), 043511.
- Rydning, D. R. J. G. J. (2018). The digitization of the world from edge to core. Framingham: International Data Corporation.
- Sainio, S., Wester, N., Aarva, A., Titus, C. J., Nordlund, D., Kauppinen, E. I. and Pitkänen, O. (2020). Trends in Carbon, Oxygen, and Nitrogen Core in the X-ray Absorption Spectroscopy of Carbon Nanomaterials: A Guide for the Perplexed. *Journal of Physical Chemistry C*.
- Salunkhe, P., AV, M. A. and Kekuda, D. (2020). Investigation on tailoring physical properties of Nickel Oxide thin films grown by dc magnetron sputtering. *Materials Research Express*, 7(1), 016427.
- Sánchez-López, J., Fernandez, A., Donnet, C. and Erdemir, A. (2008). Tribology of Diamond-Like Carbon Films: Fundamentals and Applications. In: Springer Press, New York.
- Scarselli, M., Castrucci, P. and De Crescenzi, M. (2012). Electronic and optoelectronic nano-devices based on carbon nanotubes. *Journal of Physics: Condensed Matter*, 24(31), 313202.
- Schabes, M. E. (2008). Micromagnetic simulations for terabit/in² head/media systems. *Journal of Magnetism and Magnetic Materials*, 320(22), 2880-2884.
- Schultrich, B. (2018). Tetrahedrally bonded amorphous carbon films I: basics, structure and preparation (Vol. 263): Springer.

- Sedlmair, J., Gleber, S.-C., Peth, C., Mann, K., Niemeyer, J. and Thieme, J. (2012). Characterization of refractory organic substances by NEXAFS using a compact X-ray source. *Journal of Soils and Sediments*, 12(1), 24-34.
- Seigler, M. A., Covington, M. W., Mallery, M. L., Zhou, H. and Itagi, A. V. (2013). Recording head for heat assisted magnetic recording. In: Google Patents.
- Sheeja, D., Tay, B., Lau, S. P., Shi, X. and Ding, X.-z. (2000). Structural and tribological characterization of multilayer *ta*-C films prepared by filtered cathodic vacuum arc with substrate pulse biasing. *Surface and Coatings Technology*, 132(2-3), 228-232.
- Shi, J., Shi, X., Sun, Z., Liu, E., Yang, H., Cheah, L. and Jin, X. (1999). Structural properties of amorphous silicon-carbon films deposited by the filtered cathodic vacuum arc technique. *Journal of Physics: Condensed Matter*, 11(26), 5111.
- Shi, X., Cheah, L., Shi, J., Sun, Z. and Tay, B. (1999). On the upper limit of content in tetrahedral amorphous carbon film. *Journal of Physics: Condensed Matter*, 11(1), 185.
- Silva, S., Robertson, J., Amaratunga, G., Rafferty, B., Brown, L., Schwan, J. and Mariotto, G. (1997). Nitrogen modification of hydrogenated amorphous carbon films. *Journal of applied physics*, 81(6), 2626-2634.
- Soin, N., Roy, S. S., Ray, S. C., Lemoine, P., Rahman, M. A., Maguire, P. D. and McLaughlin, J. A. (2012). Thickness dependent electronic structure of ultra-thin tetrahedral amorphous carbon (*ta*-C) films. *Thin Solid Films*, 520(7), 2909-2915.
- Stöhr, J. (2013). NEXAFS spectroscopy (Vol. 25): Springer Science & Business Media.
- Sumant, A. V., Gilbert, P., Grierson, D. S., Konicek, A. R., Abrecht, M., Butler, J. E. and Carpick, R. W. (2007). Surface composition, bonding, and morphology in the nucleation and growth of ultra-thin, high quality nanocrystalline diamond films. *Diamond and related materials*, 16(4-7), 718-724.

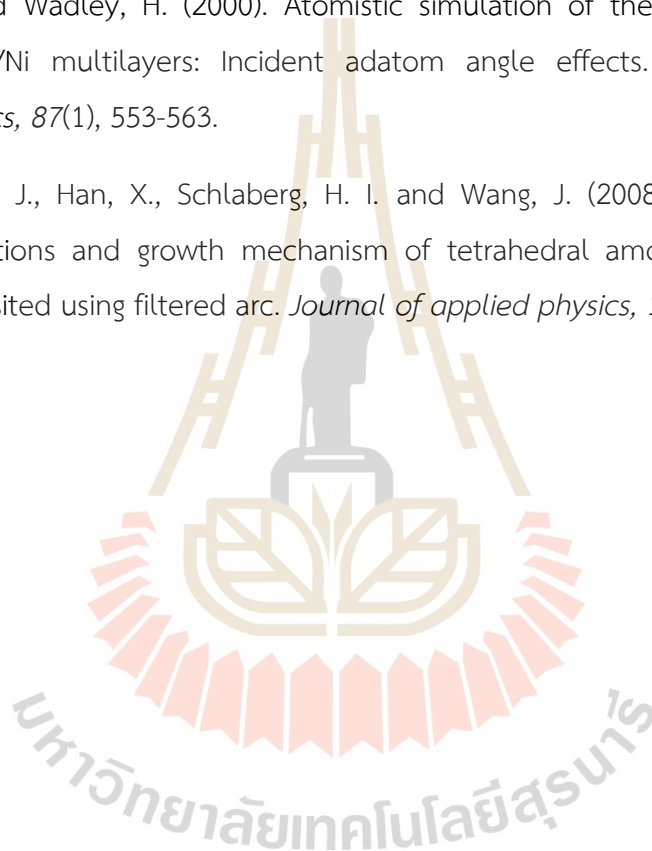
- Takahara, H. (2017). Thickness and composition analysis of thin film samples using FP method by XRF analysis. *Rigaku J*, 33, 17-21.
- Tan, A. (2007). Corrosion and tribological properties of ultra-thin DLC films with different nitrogen contents in magnetic recording media. *Diamond and related materials*, 16(3), 467-472.
- Tay, B., Shi, X., Cheah, L. and Flynn, D. (1997). Growth conditions and properties of tetrahedral amorphous carbon films. *Thin Solid Films*, 308, 199-203.
- Tay, B., Shi, X., Liu, E., Tan, H. and Cheah, L. (1999). Effects of substrate temperature on the properties of tetrahedral amorphous carbon films. *Thin Solid Films*, 346(1-2), 155- 161.
- Tay, B., Shi, X., Tan, H. and Chua, D. H. (1999). Investigation of tetrahedral amorphous carbon films using x-ray photoelectron and Raman spectroscopy. *Surface and Interface Analysis*, 28(1), 231-234.
- Tomcik, B., Osipowicz, T. and Lee, J. (2000). Diamond-like film as a corrosion protective layer on the hard disk. *Thin Solid Films*, 360(1-2), 173-180.
- Treutler, C. P. (2005). Industrial use of plasma-deposited coatings for components of automotive fuel injection systems. *Surface and Coatings Technology*, 200(5-6), 1969-1975.
- Upmanyu, A. K., Kapil, A., Mehta, D. and Kumar, S. (2021). Thickness measurement of low-Z films fabricated on thick substrate using EDXRF technique. *Vacuum*, 183, 109852.
- Van Grieken, R. and Markowicz, A. (2001). *Handbook of X-ray Spectrometry*: CRC press.
- Varanasi, S., Lauer, J., Talke, F., Wang, G. and Judy, J. (1997). Friction and wear studies of carbon overcoated thin films magnetic sliders: application of Raman microspectroscopy.
- Veeco Instruments Inc. (2012). NEXUS DLCXi Diamond-Like Carbon Deposition System.

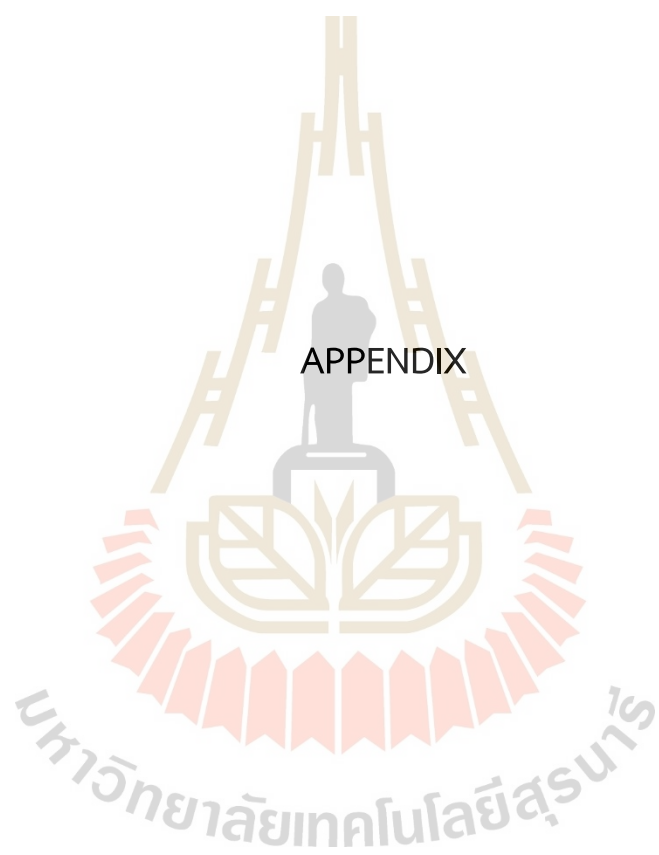
- Vetter, J. (2014). 60 years of DLC coatings: historical highlights and technical review of cathodic arc processes to synthesize various DLC types, and their evolution for industrial applications. *Surface and Coatings Technology*, 257, 213-240.
- Vieira, J., Oliveira Jr, F., Salvaro, D., Maffezzolli, G., de Mello, J. B., Vicente, A. and Cunha, R. (2020). Rheology and soft tribology of thickened dispersions aiming the development of oropharyngeal dysphagia-oriented products. *Current research in food science*, 3, 19-29.
- Voevodin, A., Phelps, A., Zabinski, J. and Donley, M. (1996). Friction induced phase transformation of pulsed laser deposited diamond-like carbon. *Diamond and related materials*, 5(11), 1264-1269.
- Wada, A., Ogaki, T., Niibe, M., Tagawa, M., Saitoh, H., Kanda, K. and Ito, H. (2011). Local structural analysis of a-SiC_x: H films formed by decomposition of tetramethylsilane in microwave discharge flow of Ar. *Diamond and related materials*, 20(3), 364-367.
- Wang, J., Jia, X., Wang, T., Geng, S., Zhou, C., Yang, F. and Li, Y. (2016). Synthesis and microwave absorption property of two-dimensional porous nickel oxide nanoflakes/carbon nanotubes nanocomposites with a threaded structure. *Journal of Alloys and Compounds*, 689, 366-373.
- Wang, L., Huang, X., Jiang, S., Li, M., Zhang, K., Yan, Y. and Xue, J. M. (2017). Increasing gas bubble escape rate for water splitting with nonwoven stainless steel fabrics. *ACS Applied Materials & Interfaces*, 9(46), 40281-40289.
- Wang, N. and Komvopoulos, K. (2011). Thermal stability of ultrathin amorphous carbon films for energy-assisted magnetic recording. *IEEE Transactions on Magnetics*, 47(9), 2277-2282.
- Wang, N. and Komvopoulos, K. (2012). Incidence angle effect of energetic carbon ions on deposition rate, topography, and structure of ultrathin amorphous carbon films deposited by filtered cathodic vacuum arc. *IEEE Transactions on Magnetics*, 48(7), 2220-2227.

- Wang, Y., Moitreyee, M., Kumar, R., Shen, L., Zeng, K., Chai, J. and Pan, J. (2004). A comparative study of low dielectric constant barrier layer, etch stop and hardmask films of hydrogenated amorphous Si-(C, O, N). *Thin Solid Films*, 460(1-2), 211-216.
- Watts, B., Thomsen, L. and Dastoor, P. (2006). Methods in carbon K-edge NEXAFS: Experiment and analysis. *Journal of Electron Spectroscopy and Related Phenomena*, 151(2), 105-120.
- Wei, C. and Yen, J.-Y. (2007). Effect of film thickness and interlayer on the adhesion strength of diamond like carbon films on different substrates. *Diamond and related materials*, 16(4-7), 1325-1330.
- WIKI, L. Plasma enhanced chemical vapor deposition.
- Wood, R., Williams, M., Kavcic, A. and Miles, J. (2009). The feasibility of magnetic recording at 10 terabits per square inch on conventional media. *IEEE Transactions on Magnetics*, 45(2), 917-923.
- Xu, S., Tay, B., Tan, H., Zhong, L., Tu, Y., Silva, S. and Milne, W. (1996). Properties of carbon ion deposited tetrahedral amorphous carbon films as a function of ion energy. *Journal of applied physics*, 79(9), 7234-7240.
- Yamamoto, K., Koga, Y. and Fujiwara, S. (2001). XPS studies of amorphous SiCN thin films prepared by nitrogen ion-assisted pulsed-laser deposition of SiC target. *Diamond and related materials*, 10(9-10), 1921-1926.
- Yamamoto, T., Hyodo, H., Tsuchitani, S. and Kaneko, R. (2003). Ultrathin amorphous carbon overcoats by filtered cathodic arc deposition. *IEEE Transactions on Magnetics*, 39(5), 2201-2204.
- Yeo, J. R. (2015). Ultrathin carbon-based overcoats for extremely high-density magnetic recording: National University of Singapore (Singapore).
- Yeo, R. J. (2017). Ultrathin carbon-based overcoats for extremely high-density magnetic recording: Springer.

- Yeo, R. J., Dwivedi, N., Rismani, E., Satyanarayana, N., Kundu, S., Goohpattader, P. S. and Tripathy, S. (2014). Enhanced tribological, corrosion, and microstructural properties of an ultrathin (< 2 nm) silicon nitride/carbon bilayer overcoat for high density magnetic storage. *ACS Applied Materials & Interfaces*, 6(12), 9376-9385.
- Yeo, R. J., Dwivedi, N., Zhang, L., Zhang, Z., Lim, C. Y., Tripathy, S. and Bhatia, C. S. (2015). Durable ultrathin silicon nitride/carbon bilayer overcoats for magnetic heads: The role of enhanced interfacial bonding. *Journal of applied physics*, 117(4), 045310.
- Yeo, R. J., Rismani, E., Dwivedi, N., Blackwood, D. J., Tan, H., Zhang, Z. and Bhatia, C. (2014). Bi-level surface modification of hard disk media by carbon using filtered cathodic vacuum arc: Reduced overcoat thickness without reduced corrosion performance. *Diamond and related materials*, 44, 100-108.
- Yin, Z.-Z., Huang, W., Song, X., Zhang, Q. and Zeng, R.-C. (2020). Self-catalytic degradation of iron-bearing chemical conversion coating on magnesium alloys-Influence of Fe content. *Frontiers of Materials Science*, 14(3), 296-313.
- Yu, X., Zhang, X., Wang, C.-b., Hua, M. and Wang, L.-g. (2004). A tribological study of tetrahedral amorphous carbon films prepared by filtered cathodic vacuum arc technique. *Vacuum*, 75(3), 231-236.
- Zhang, H.-S. and Komvopoulos, K. (2009a). Surface modification of magnetic recording media by filtered cathodic vacuum arc. *Journal of applied physics*, 106(9), 093504.
- Zhang, H.-S. and Komvopoulos, K. (2009b). Synthesis of ultrathin carbon films by direct current filtered cathodic vacuum arc. *Journal of applied physics*, 105(8), 083305.
- Zhang, L., Wei, X., Lin, Y. and Wang, F. (2015). A ternary phase diagram for amorphous carbon. *Carbon*, 94, 202-213.

- Zhong, M., Zhang, C. and Luo, J. (2008). Effect of substrate morphology on the roughness evolution of ultra-thin DLC films. *Applied Surface Science*, 254(21), 6742-6748.
- Zhong, M., Zhang, C., Luo, J. and Lu, X. (2009). The protective properties of ultra-thin diamond like carbon films for high density magnetic storage devices. *Applied Surface Science*, 256(1), 322-328.
- Zhou, X. and Wadley, H. (2000). Atomistic simulation of the vapor deposition of Ni/Cu/Ni multilayers: Incident adatom angle effects. *Journal of applied physics*, 87(1), 553-563.
- Zhu, J., Han, J., Han, X., Schlaberg, H. I. and Wang, J. (2008). sp^3 -rich deposition conditions and growth mechanism of tetrahedral amorphous carbon films deposited using filtered arc. *Journal of applied physics*, 104(1), 013512.





APPENDIX

มหาวิทยาลัยเทคโนโลยีสุรนารี

APPENDIX

PRESENTATIONS AND PUBLICATIONS

Abstract submitted for the 2018 ISAF-FMA-AMF-AMEC-PFM Joint Conference at Hiroshima (IFAAP Hiroshima2018)

Characterization of DLC ta-C films prepared by pulsed filtered cathodic arc using Raman spectroscopy and XPS

Warintorn Chatarata^{1,*}, Saroj Rujirawata¹, Rattikorn Yimmiruna² and Narong Chanlekb³

¹School of Physics, Institute of Science and NANOTEC-SUT COE on Advanced Functional Nanomaterials, Suranaree University of Technology, Nakhon Ratchasima 30000, Thailand.

²School of Energy Science and Engineering, Vidyasirimedhi Institute of Science and Technology, Rayong 21210, Thailand.

³Synchrotron Light Research Institute (Public Organization), Nakhon Ratchasima 30000, Thailand.

*Corresponding Author: macdatsf@gmail.com

Diamond-like carbon (DLC) are very promising materials for numerous applications. The growing of relevance of Tetrahedral carbon amorphous (ta-C) is mainly due to long-term stability of their outstanding properties. A full understanding of their thickness relate to local chemistry for improving their performance. The ta-C films were deposited on substrate. Silicon film was initially deposited as a seed layer on the substrate by using DC magnetron sputtering technique. The ta-C film was deposited on Si-layer via a pulsed filtered cathodic arc (PFCA) system. The thickness growth films monitor by X-Ray Fluorescence (XRF). This work reports the characteristic of ultra-thin tetrahedral amorphous carbon (ta-C) films deposited on Alumina wafers by PFCA. The film thicknesses are between 5-30 Å. The formation of film structure by visible Raman spectroscopy 514 nm excitation and results will also confirmed using XPS binding energy and XPS depth profile analysis. The variation of film characteristic and thickness is discussed.

References

- [1] FAN-Xin L., Zhen-Lin W., SURF COAT TECH 203 1829-1832(2009)
- [2] J. Robertson, Thin Solid Films 383 81-88(2001)
- [3] M.C. Polo, J.L. Andujar, Diam. Relat. Mater 9 663 - 667(2000)
- [4] C.Srisang, P.Asanithi, Applied Surface science 258 5605-5609 (2012)

Abstract submitted for the 5th International Conference on Smart Materials and Nanotechnology (SmartMat@2020) 1st-4th Dec 2020, Garden Cliff Resort & Spa Hotel, Pattaya, Thailand.

*The 5th International Conference on Smart Materials and Nanotechnology
(SmartMat@2020)
1st-4th December 2020, Garden Cliff Resort & Spa Hotel, Pattaya, Thailand*



Dependence of the tribology and microstructure properties of ultrathin
Tetrahedral amorphous carbon films (< 5 nm)

Warintorn Chatarat^{1,2*}, Narong Chanlek³, Chanan Euaruksakul³, Saroj Rujirawat³,
Rattikorn Yimmirun⁴,

¹ Research Network NANOTEC-SUT on Advanced Nanomaterials and
Characterization, School of Physics, Institute of Science,
Suranaree University of Technology, Nakhonratchasima, Thailand

² Seagate Technology, Nakhon Ratchasima, Thailand

³ Synchrotron Light Research Institute (Public Organization), Nakhonratchasima,
Thailand

⁴ Research Network of NANOTEC-VISTEC on Nanotechnology for Energy and
School of Energy Science and Engineering, Vidyasirimedhi Institute of Science
and Technology, Wangchan, Rayong, Thailand

*Email: warintorn.chatarat@seagate.com

Abstract

Tetrahedral amorphous carbon (ta-C) films coating have increased demand as protective hard coating for mechanical component due to their exceptional mechanical and tribological performance. Tribological durability properties of ultrathin ta-C films (thickness 0.2–2nm) deposited using filtered cathodic vacuum arc (FCVA) methods was evaluated using low-load reciprocating friction tests and x-ray photoelectron spectroscopy (XPS). Coefficient of friction (COF) notably increased at a certain film thickness were nearly equal to surface roughness and gradually drop down and settle when the ta-c film thickness was 1.0 nm or greater as corresponding to film thickness increasing. In contrast, the reciprocating wear time to failure (RW-TTF) rapid increase as non-linear of function of thickness, was observed. The structural properties are found to be strongly correlated with the C1s XPS spectra that clearly indicate the sp³ (C-C) bonding rapidly increase from 0.2- 1.0 nm thick ta-C films, slightly increase rate when the thickness of the DLC films was 2.0 nm or greater. It is concluded that tribology and microstructure properties depend on ultrathin ta-C thickness.

Keyword: Filtered cathodic vacuum arc, Ultrathin ta-C film, XPS, Tribology

Abstract submitted for The 5th International Conference on Applied Physics and Materials Applications & Applied Magnetism and Ferroelectrics (ICAPMA-JMAG-2021) Pattaya, Thailand.

The 5th International Conference on Applied Physics and Materials Applications & Applied Magnetism and Ferroelectrics (ICAPMA-JMAG-2021)



A tribology investigation of ultra ultrathin Tetrahedral amorphous carbon films (<3 nm) fabricated by the filtered cathodic vacuum arc technique

Warintorn Chatarat^{1,2*}, Narong Chanlek³, Prayoon Songsiririthigul³, Saroj Rujirawat³, Rattikom Yimnirun⁴, Thanun Chunjaemsri²

¹ Research Network NANOTEC-SUT on Advanced Nanomaterials and Characterization, School of Physics, Institute of Science, Suranaree University of Technology, Nakhonratchasima, Thailand

² Seagate Technology, Nakhon Ratchasima, Thailand

³ Synchrotron Light Research Institute (Public Organization), Nakhonratchasima, Thailand

⁴ Research Network of NANOTEC-VISTEC on Nanotechnology for Energy and School of Energy Science and Engineering, Vidyasirimedhi Institute of Science and Technology, Wangchan, Rayong, Thailand

*Email: warintorn.chatarat@seagate.com

Abstract

Along with its excellent mechanical and tribological performance, tetrahedral amorphous carbon (ta-C) films have become more widespread as protective hard coatings for mechanical components. Low-load reciprocating friction tests and x-ray photoelectron spectroscopy (XPS) were used to examine the tribological durability properties of ultrathin ta-C films (thickness 0.5–3nm) deposited by filtered cathodic vacuum arc (FCVA) approaches. When the ta-c film thickness reached 1.0 nm or larger, the coefficient of friction (COF) increased noticeably until it was about equal to surface roughness, then progressively decreased and settled as the film thickness grew. The reciprocating wear time to failure (RW-TTF), on the other hand, was found to rapidly grow as a non-linear function of thickness. The structural properties are found to be significantly associated with the C1s XPS spectra, which clearly show that sp³ (C-C) bonding rapidly increases from 0.5 to 1.0 nm thick ta-C films, with a minor rise rate when the DLC films are 2.0 nm or larger in thickness. The results show that ultrathin ta-C thickness affects tribology and microstructure parameters.

Keyword: 3~5 key words in common usage should be included. Multiple keywords should be separated by a comma.



Contents lists available at ScienceDirect

Materialia

journal homepage: www.elsevier.com/locate/mtla

Full Length Article



Structural characterization of ultrathin diamond-like carbon overcoats for high areal density magnetic recording

Warintorn Chatarat^{a,b,c}, Narong Chanlek^{a,d,*}, Chanan Euaruksakul^d, Hideki Nakajima^d,
Jesada Rusamiputi^b, Somlak Ittisanronnachai^e, Natthaphong Konkhunhot^f, Saroj Rujirawat^d,
Prayoon Songsiririthigul^{a,c}, Rattikorn Yimnirun^{e,g}

^a Research Network NANOTEC–SUT on Advanced Nanomaterials and Characterization, School of Physics, Institute of Science, Suranaree University of Technology, Nakhon Ratchasima, 30000, Thailand

^b Seagate Technology, Nakhon Ratchasima, 30170, Thailand

^c Thailand Center of Excellence in Physics, MHEsRI, Bangkok, 10400, Thailand

^d Synchrotron Light Research Institute (Public Organization), Nakhon Ratchasima, 30000, Thailand

^e School of Energy Science and Engineering, Vidyasirimedhi Institute of Science and Technology, Wangchan, Rayong, 21210, Thailand

^f Aviation Industrial Institute of Rajamangala University of Technology Isan, Rajamangala University of Technology Isan, Nakhon Ratchasima, 30000, Thailand

^g Research Network of NANOTEC–VISTEC (RNN) on Nanotechnology for Energy, Vidyasirimedhi Institute of Science and Technology (VISTEC), Wangchan, Rayong, 21210, Thailand

ARTICLE INFO

Keywords

Ultrathin overcoat
Pulsed filtered cathodic vacuum arc
Near edge X-ray absorption fine structure spectroscopy
Coefficient of friction

ABSTRACT

This paper reports a comprehensive study on chemical structures of ultrathin diamond-like carbon (DLC) overcoats for high areal density magnetic recording. The DLC overcoats were fabricated in a range of thicknesses between 0.5 and 5.0 nm with Si interlayer on NiFe substrates using a pulsed filtered cathodic vacuum arc (PFCVA) technique. The overcoat thicknesses were accurately determined by high-resolution transmission electron microscopy and wavelength dispersive X-ray fluorescence techniques. The surface morphology, chemical composition, microstructure, and tribological properties were systematically investigated by atomic force microscopy, X-ray photoelectron spectroscopy, near-edge X-ray absorption fine structure, Raman spectroscopy techniques, and a reciprocating wear test. The results showed that the surface morphologies of DLC overcoats were atomically smooth with a root mean square surface roughness below 0.23 nm. The DLC overcoats had high sp^3 bonds fraction. However, as the overcoat thickness was thinner than 1 nm, the sp^2 bonds fraction suddenly increased resulting in a significant increase in the coefficient of friction. The obtained results demonstrated the limitation of the thickness of the DLC overcoat fabricated by the PFCVA technique as a protective coating for high-density magnetic storage devices.

1. Introduction

Diamond-like carbon (DLC) films are a class of amorphous carbon films that contain a high fraction of tetrahedral sp^3 bonded carbon in their structure [1–5]. They have been extensively used as surface coating materials for a wide range of applications, such as cutting tools, automotive pistons and cylinders, and microelectromechanical systems (MEMS), due to their exceptional properties, including high hardness, high chemical inertness, ultra-smoothness, and high thermal stability [2,6,7]. In the magnetic storage industry, the ultrathin DLC films (< 5 nm) are commonly used as an overcoat to provide protection against

corrosion and mechanical wear for sliders, read/write heads, and magnetic recording media [8–11]. They are also proposed as an overcoat for new magnetic recording technologies, such as heat-assisted magnetic recording (HAMR), because of their resilience against structural degradations, graphitization, or oxidation, under the intense localized heating of a pulsed laser [12–14]. In the overcoat development, it is desirable to decrease the overcoat thickness as thin as possible, down to a few nanometers. The decrease in overcoat thickness reduces the head media spacing, the physical spacing between the head and media, hence, increasing the density and capacity of hard disk drives (HDDs). According to the industrial roadmap, the overcoat thickness has to be less

* Corresponding author.

E-mail address: narong@slri.or.th (N. Chanlek).

<https://doi.org/10.1016/j.mtl.2022.101650>

Received 9 October 2022; Accepted 7 December 2022

Available online 8 December 2022

2589-1529/© 2022 Acta Materialia Inc. Published by Elsevier B.V. All rights reserved.

than 1 nm to achieve the areal densities of 10 Tb/in² and higher in next generation HDD [15,16]. Therefore, the challenge is to decrease the overcoat thickness while retaining the tribological properties, such as high hardness and low friction.

Filtered cathodic vacuum arc (FCVA) is a promising technique for fabricating continuous, homogeneous, smooth, and ultrathin DLC overcoats [2,17–20]. The previous studies also reported that the FCVA can produce high thermal stability carbon overcoats which is promising for the HAMR technology [20]. However, as the thickness reaches the nanometer range, the fabricated overcoats may not be able to maintain their chemical bonding structure, especially their high sp³ bonds fraction, which directly associated with their mechanical properties, such as density, wear, corrosion, thermal stability, and hardness [2,21]. It is, therefore, both fundamentally and technologically important to understand the correlation between the overcoat thickness, chemical bonding structure and tribological properties. Despite the intensive studies on the growth of DLC films, the detailed investigations and reports on the structure of ultrathin DLC films with thickness below 2 nm are still limited [10,11,12].

In this paper, we present a comprehensive study on the chemical bonding structure and tribological properties of an ultrathin DLC film overcoat with thicknesses of between 0.5 and 5 nm using pulsed filtered cathodic vacuum arc (PFCVA). The ultrathin DLC films were deposited on NiFe substrates which are a common magnetic material for a slider pole in the HDD industry. A Si interlayer with a thickness of 0.5 nm was also introduced as an intermediate layer to reduce the internal stress and enhance the adhesive between an overcoat layer and substrate [2,18,22,23]. The thicknesses of the fabricated overcoat were accurately evaluated by using wavelength dispersive X-ray fluorescence (WDXRF) and high-resolution transmission electron microscopy (HRTEM). The surface morphology and chemical bonding structure were systematically examined using atomic force microscopy (AFM) techniques, X-ray photoelectron spectroscopy (XPS), near-edge X-ray absorption fine structure (NEXAFS), and Raman spectroscopy techniques. The tribological properties, especially coefficient of friction (COF), were also analyzed using the reciprocating wear test. The correlation between the chemical bonding structure and tribological properties as a function of the overcoat thickness was thoroughly studied. The results demonstrated the limitation of the thickness of the DLC overcoat fabricated by the PFCVA technique as a protective coating for high-density magnetic storage devices.

2. Material and methods

2.1. Fabrication

The ultrathin DLC overcoats were fabricated on NiFe substrates (Ni:80 at%, Fe:20 at%) using a PFCVA system (NEXUS DLC-Xi, Veeco Instrument Inc) at Seagate Technology, Nakhon Ratchasima, Thailand. The PFCVA deposition technique is described in detail elsewhere [24,25]. Highly pure graphite (Veeco Instrument Inc) with 99.999% purity was used as a carbon source. The deposition was carried out in the vacuum chamber with a base pressure of approximately 2.0×10^{-7} Torr. Prior to the deposition, the NiFe substrate was cleaned by using the radio frequency (RF) plasma sputter etching technique with Ar⁺ ions. The Si layer with a thickness of 0.5 nm was first deposited as an interlayer between the substrate and DLC film. In this work, the thickness of Si interlayer is limited by the coating system. The effect of Si interlayer on the structure of DLC films has been studied previously by Liu et al [23]. The carbon film was subsequently deposited using the PFCVA technique, which utilized energetic carbon ions from the graphite target. A 90°-bend solenoid was used to filter out neutrals and microscopic graphite particles, which are also emitted from the graphite arc. The substrate rotation method was used to enhance the uniformity. The deposition rate and thickness were controlled by the deposition pulse. A series of ultrathin DLC films with thicknesses varying from 0.5 to 5.0 nm

were fabricated using the same controlled deposition conditions.

2.2. Characterizations

The thicknesses of the fabricated overcoats were estimated using a WDXRF spectrometer (2830ZT, Malvern Panalytical). The analysis was performed under the pressure of 1.5×10^{-3} Torr without any additional sample treatment or preparation. The WDXRF spectra were analyzed using the Fundamental Parameter modeling, which is fully integrated into the super Q thin-film platform of the WDXRF spectrometer. More details on the WDXRF approach for determining film thickness and elemental composition are described elsewhere [26]. The thickness was also derived from the cross-sectional images taken using an HRTEM (JEM ARM200F NEOARM). The focus ion beam with an in-situ lift-out method was used to prepare cross-sectional specimens for HRTEM. The surface roughness of the films was examined using an AFM (Bruker, Innova Scanning Probe microscope). The measurements were carried out in contact mode in four different regions over a scan area of $1 \times 1 \mu\text{m}^2$.

The structure of the overcoats was studied using a visible Raman spectrometer (Renishaw InVia Reflex Raman). The Raman spectra were recorded in the region of 800 – 2200 cm⁻¹ using a 532 nm laser with a defocused laser beam power of 50 mW and spot size of approximately 2 μm. The line focus was performed to avoid sample degradation. The spectra were analyzed using Renishaw WIRE 5.0 software for background noise subtraction and Gaussian peak fitting. NEXAFS experiments were performed at Beamline 3.2Ub: Photoelectron Emission Microscopy (PEEM) at Synchrotron Light Research Institute (SLRI), Thailand. In this work, all NEXAFS spectra of the C K-edge signal were recorded the total electron yield (TEY) mode from the secondary electron in the photon energy range of 270 – 320 eV at room temperature and under a pressure of less than 1×10^{-8} Torr. The samples were irradiated with the monochromatic X-ray from a planar undulator at an incidence angle of 17° with electric field polarization in-plane with the surface. These absorption signals were firstly divided by a NEXAFS scan of a freshly flashed Si (100) wafer on the same photon energy range. The divided spectra were normalized in the way that the intensity in the pre-edge region (photon energy 270 – 280 eV) and the post-edge (continuum) region at 330 eV were set to zero and unity, respectively. In this method, variations in spectra intensity are caused only by chemical changes and are independent of the number density of absorption atoms. The NEXAFS spectra were analyzed by using Igor Pro 6.3 software. Highly Oriented Pyrolytic Graphite (HOPG) was used as a reference material [27,28] as the spectrum of a clean HOPG theoretically exhibits the electronic structure of sp² hybridized carbon. The chemical composition was also studied using a PHI5000 Versa probe XPS system (ULVAC-PHI, Japan). The monochromatic AlKα X-ray (1486.6 eV) with a spot size of 10 μm was used for excitation. No Ar⁺ ion beam etching or surface treatment was performed before the analysis. The high-resolution XPS spectra were recorded with a pass energy of 46.95 eV and a step increment of 0.05 eV. The spectra were analyzed using MultiPak software. The “Shirley-Type” background subtraction and mixed Gaussian-Lorentzian function were applied for curved fitting [29].

The tribological properties of the films were investigated using a ball-on-disk universal mechanical tester (CERT UMT-2, Bruker-UMT TriboLab). All tests were conducted in the open air at a temperature of 21 – 25°C and relative humidity of 40 – 50%. The test was carried out using a reciprocating slide with a continuous load of 50 mN and a constant speed of 200 rpm. The reciprocating coated substrate was in the lower position, and the stationary coated ball with a diameter of 9.5 mm was in the upper position. The stroke length and frequency of the sliding mechanism were 6 mm and 3.33 Hz, respectively. The COF of the films was estimated from the normal and friction force data.

3. Results

3.1. Thickness and surface morphology

Fig. 1 shows the cross-sectional HRTEM images of the ultrathin DLC overcoats fabricated on NiFe substrates with different thicknesses. The images show that the films were homogeneous and dense. An area between the NiFe substrate and the deposited layer is clearly distinguishable. However, it is difficult to distinguish a region between the deposited Si interlayer and ultrathin DLC overcoat, as they showed the same contrast images. This is due to the fact that both Si and DLC overcoat layers are amorphous [11]. The WDXRF approach used in this work, on the other hand, can detect the presence of the Si interlayer and estimate the thickness of both the deposited DLC overcoat and Si interlayer. The nominal thicknesses of deposited Si and ultrathin DLC (Si/DLC) overcoat layers measured from cross-sectional HRTEM images

and determined by the WDXRF method are presented in Table 1. The total coating thicknesses determined from cross-sectional HRTEM images are consistent with the results obtained from WDXRF spectra, as the

Table 1
Thicknesses of the fabricated DLC overcoats derived from WDXRF spectra and cross-sectional HRTEM images.

Overcoat	Deposition condition Pulse count	Measured thickness (nm)		
		WDXRF Si	DLC	HRTEM Si/DLC
0.5 nm	100	0.51	0.52	1.08
1.0 nm	200	0.51	1.06	1.83
2.0 nm	400	0.49	2.15	2.35
3.0 nm	600	0.47	3.35	3.76
4.0 nm	800	0.54	4.16	4.85
5.0 nm	1000	0.50	5.05	5.69

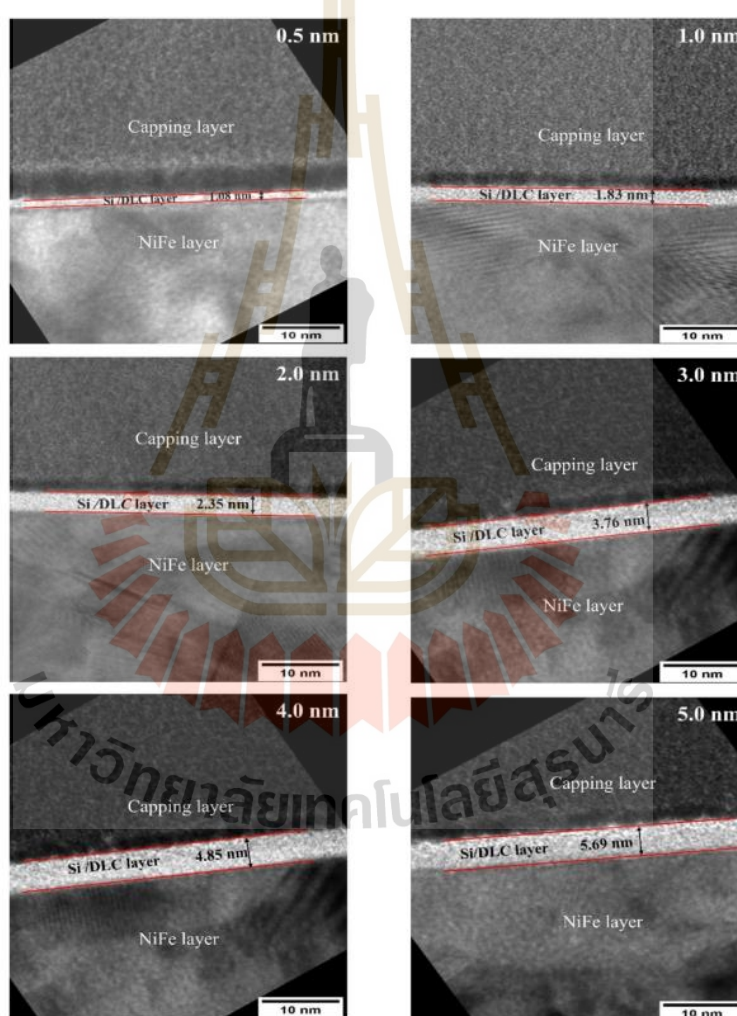


Fig. 1. Cross-section HRTEM images of the fabricated DLC overcoats with Si interlayers on NiFe substrates.

deposited Si interlayer is expected to be approximately 0.5 nm. This validates the accuracy of thickness measurement in this work by the WDXRF technique.

Fig. 2 presents the AFM images showing the surface morphologies of NiFe substrate, deposited Si interlayer, and fabricated ultrathin DLC overcoats. The results revealed that the surface of fabricated DLC overcoats is smooth and uniform over a large area. The root mean square surface roughness (Rq) was estimated to be in a range of between 0.13 and 0.23 nm, which is comparable to the values obtained in the previous studies on both ultrathin and thicker DLC films [2,30].

3.2. Chemical composition and structure

The structure of the ultrathin DLC overcoats was examined by the Raman spectroscopy technique. Fig. 3(a) shows the Raman spectra of the overcoats in a range of 1100–1800 cm^{-1} excited by a laser wavelength of 532 nm. All spectra showed a single broad peak centered at approximately 1560 cm^{-1} with a small shoulder at approximately 1360 cm^{-1} . This peak slightly shifted toward a lower wavelength and became broader when the overcoat thickness decreased. The spectra were fitted into two Gaussian peaks after linear background subtraction. The first peak at a wavenumber range of 1520–1580 cm^{-1} corresponds to the disorder (G) peak, which originated from the in-plane bond stretching motion of all aromatic (rings) and olefinic sp^2 carbon pairs (chains) [2, 31]. The second peak at a wavenumber range of 1340–1360 cm^{-1} known as the disorder (D) peak, is due to the breathing mode of sp^2 carbon in aromatic rings [4,32]. The G peak position and the intensity ratio of the D peak to the G peak (I_D/I_G) are strongly related to the sp^3 bonds fraction [23,31]. The upper shift of the G peak position reveals the increase of sp^2 clustering and decrease of sp^3 bonds fraction, whereas the decrease in the I_D/I_G ratio suggests the increase of sp^3 bonds fraction [31,33]. Fig. 3(b) shows the plot of the G peak position and estimated I_D/I_G ratio as a function of overcoat thickness. It was observed that the G peak shifted toward a lower wavenumber and the I_D/I_G ratio increased as the overcoat thickness decreased. This suggests the decrease of sp^3 bonds fraction with decreasing overcoat thickness.

The carbon hybridization states and bonding orientations were investigated using the NEXAFS technique. The analysis depth of NEXAFS technique is in a range of approximately 5 nm [27]. Fig. 4 shows the C K-edge NEXAFS spectra of HOPG and the fabricated ultrathin DLC overcoats. The HOPG spectrum had a similar shape to graphite spectra as described elsewhere [34,35]. All C K-edge spectra of the DLC overcoats exhibited two distinct characteristics, including a sharp pre-edge peak at approximately 285.5 eV and a broad photon energy peak between 290 and 320 eV. The pre-edge resonance at approximately 285.5 eV is due to the transition from C 1s orbital to unoccupied π^* orbitals. The broad peak covering photon energy between 290 and 320 eV was assigned to the σ^* band, which resulted from the overlapping of C 1s $\rightarrow \sigma^*$ transitions at sp^2 or/and sp^3 sites. The π^* resonance intensity can be considered a representative of sp^2 contents since it is well separated in energy from the rest of the resonance in the C K-edge spectra [12,36]. The normalized C K-edge NEXAFS spectra were analyzed with multiple resonance peaks formed by asymmetric Gaussian-Lorentzian mixed functions and the ionization step function using the approach previously described [37,38]. The peak at 285.5 eV originated from the C 1s $\rightarrow \pi^*$ transition for disordered C-C bonds and related to the fraction sp^2 bonds in the near-surface region [39–41]. The peak at 287.5 eV was assigned to the C 1s $\rightarrow \sigma^*$ transition for σ^* (C-H) bonds [41–43]. The shape peak at 288.8 eV corresponds to the C 1s $\rightarrow \sigma^*$ of C-Si and C-O [38,40,44,45]. The peaks at 291.6 eV and 295.8 eV are originated from the C 1s $\rightarrow \sigma^*$ transitions for C-C. The other peaks at 300.6 eV and 305.9 eV are due to C 1s $\rightarrow \sigma^*$ transitions for C=C and C=C/C=O [41,46,47]. In addition, the C-H bonds were observed in the spectra, similar to the previous report by Soin et al. [12].

The sp^2 fraction was estimated from the peak areas taken from the C K-edge spectra of ta-C overcoats and HOPG spectra using the equation

[45,48,49];

$$\text{sp}^2 \text{ fraction} = \frac{I_{\text{sam}}^{\pi^*}/I_{\text{sam}}(\Delta E)}{I_{\text{HOPG}}^{\pi^*}/I_{\text{HOPG}}(\Delta E)}$$

where $I_{\text{sam}}^{\pi^*}$ and $I_{\text{HOPG}}^{\pi^*}$ are the peak areas of the C 1s $\rightarrow \pi^*$ (C=C) transition of the sample and the HOPG, respectively. The $I_{\text{sam}}(\Delta E)$ and $I_{\text{HOPG}}(\Delta E)$ are the areas under the NEXAFS spectrum between 290.0 and 320.0 eV for the sample and HOPG, respectively, which were selected to represent the σ^* contribution to experimental data. Fig. 5 shows the plots of the estimated sp^2 fraction and π^* resonance peak intensity as a function of ta-C overcoat thickness. It was observed that the sp^2 fraction of the ta-C overcoat increased with decreasing thickness. The sp^2 fraction percentage dropped from 63% for a thickness of 0.5 nm to 34% for a thickness of 5.0 nm.

In contrast, the average C-H concentration was $1.2\% \pm 0.3\%$, independently of film thickness. Notably, this interaction between carbon and hydrogen atoms in the films can be attributed to surface contamination and hydrocarbon absorption via surface dangling bonds serving as defect sites mainly at the film's surface.

The chemical composition of the ultrathin DLC overcoats was also studied by XPS. The XPS (Fig. S1 in supplementary) results revealed the presence of C, O, and Si on the surface of all fabricated ta-C overcoats. In addition to C, O, and Si, the signals of Fe and Ni were observed for the overcoat thicknesses of less than 3.0 nm, and their intensity increased with decreasing overcoat thickness (Figs. S2 and S3 in supplementary). The presence of O could be attributed to surface contamination from exposure to the atmosphere [50]. The signal of Si originated from the deposited Si interlayer, and those of Fe and Ni were from the NiFe substrate. The observations of Si, Fe, and Ni signals confirm the accuracy of thickness measurement results as the analysis depth of the XPS technique is approximately between 3–5 nm [29].

Fig. 6(a) shows the high-resolution core level XPS spectra of the C1s peak of the ultrathin DLC overcoats. The C1s peaks of all spectra could be deconvoluted into five main peaks at the binding energies of 283.2 eV, 284.3 eV, 284.9 eV, 286.2 eV, and 287.9 eV corresponding to C-Si, sp^2 , sp^3 , C-O and C=O bonds, respectively [12,51–54]. The relative atomic percentages of each carbon bond were estimated from the peak intensities, and the results are reported in Table 2. The sp^3 bonds were found to be dominant in the structure, which is the characteristic of DLC films. Their relative atomic percentages are in the range of 36.64–64.90 at%, which corresponds to the sp^3 bonds fraction ($\text{sp}^3/(\text{sp}^3 + \text{sp}^2)$) of 55.36–76.29 at%. It was also observed that the sp^3 bonds fraction decreased, whereas the sp^2 , C-O, and C=O bonds fractions increased as the overcoat thickness decreased. The observation of C-Si bonds suggests the formation of chemical bonds between the carbon and silicon at the Si/DLC interface.

To investigate the interfacial bonding between the DLC overcoats and Si interlayer, the high-resolution core level XPS spectra of Si2p peak were fitted, as shown in Fig. 6(b). The Si2p peak of the ultrathin ta-C overcoats consisted of four main peaks at the binding energies of 99.40 eV, 100.97 eV, 102.22 eV, and 103.35 eV, which were assigned to Si-Si (Si element), Si-C (silicon-carbide), Si-O-C (silicon-oxy-carbide) and Si-O (silicon-oxide) bonds, respectively [51,55–58]. The observation of Si-C bonds suggests that a highly ionized plasma of energetic carbon ions generated by the PFCVA process can penetrate the DLC films and react (chemically bond) with the Si interlayer [18,52]. The presence of Si-O bonds could be attributed to a residual thin oxide layer on the Si interlayer prior to film growth. These residuals could also react with the energetic carbon ions and formed Si-O-C bonds [18,52]. The formation of Si-C and Si-O-C bonds between the DLC overcoat and Si-interlayer can enhance the adhesion between the carbon film and substrate [30, 52].

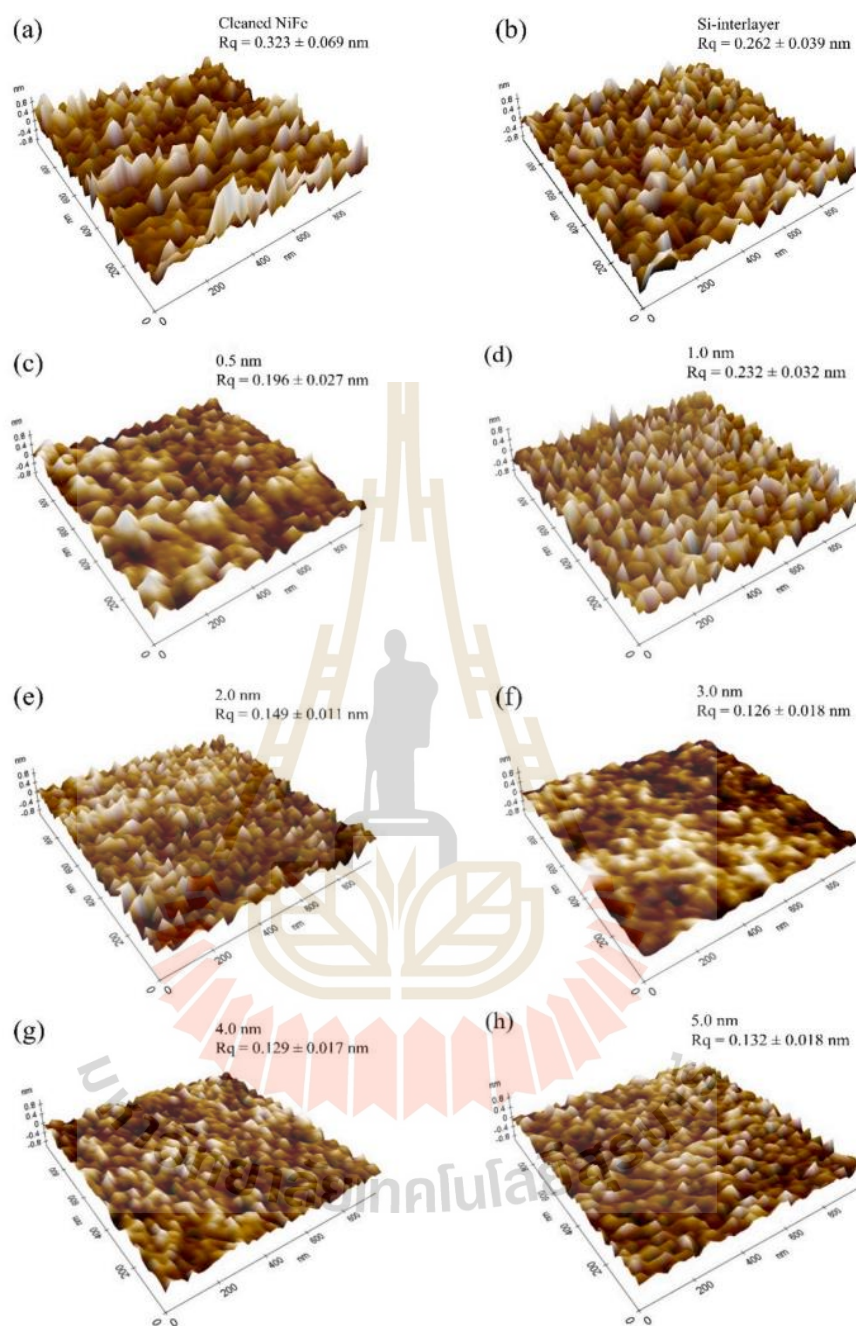


Fig. 2. AFM images showing the surface morphology of (a) cleaned NiFe substrate, (b) deposited Si-interlayer, and (c–h) fabricated DLC overcoats with thicknesses of 0.5 – 5.0 nm.

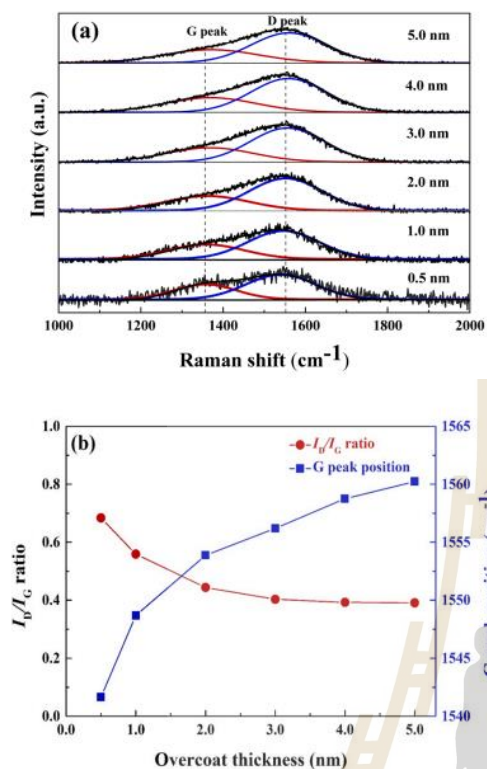


Fig. 3. (a) Raman spectra of the fabricated DLC overcoat with thicknesses of 0.5 – 5.0 nm and (b) plots of the G peak position and estimated ID/IG ratio as a function of DLC overcoat thickness.

3.3. Tribological properties

The ball-on-disk wear test was used to determine the tribological properties of the ultrathin DLC overcoats. In this test, the samples were fixed while the counterface was in contact with the surface. This setup is similar to the working condition of HDD, allowing for to determination of the COF [10]. The test was also conducted with more than 12000 cycles, which is much higher than the HDD operational lifetime. Fig. 7 shows the friction curves and optical microscopic images captured after the test of the fabricated ultrathin DLC overcoats with thicknesses of 0.5 – 5.0 nm compared with a cleaned NiFe substrate and Si-interlayer on the NiFe substrate.

It was observed that the COF of NiFe substrate and Si interlayer fluctuated with test cycles and had an average value of 0.70 and 0.69, respectively. Following the test, severe wear tracks and debris formations were observed in the optical images. The fluctuations in the COF were therefore attributed to significant wear between the ball and substrates. On the contrary, the COFs of the fabricated ta-C overcoats with thicknesses of between 2 – 5 nm were steady, and there was no visible wear track and debris in the optical images after the test. Their estimated COFs were in the range of 0.18 – 0.27. This COF value is lower than that of approximately 0.3 – 0.5 for current commercial carbon overcoats with a thickness of 0.27 nm [18,20]. However, as the DLC overcoats thickness decreased to 0.5 and 1.0 nm, the COFs showed strong fluctuation with the test cycle, and their average values suddenly

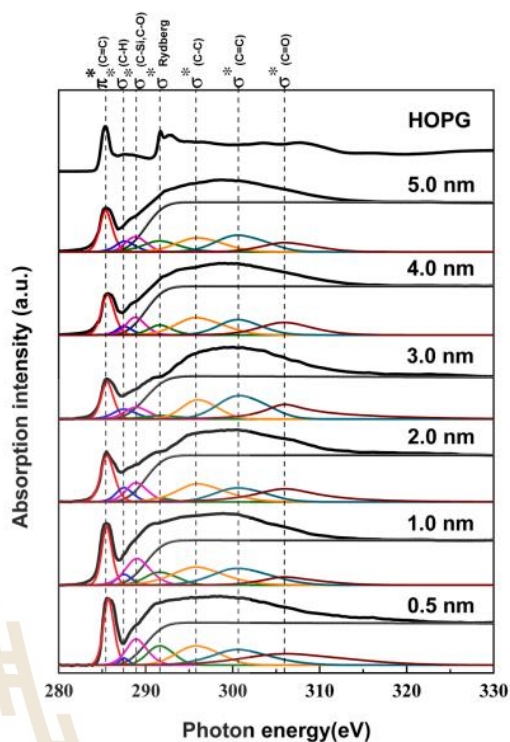


Fig. 4. Carbon K-edge NEXAFS spectra of HOPG and the fabricated DLC overcoats with thicknesses of 0.5–5.0 nm.

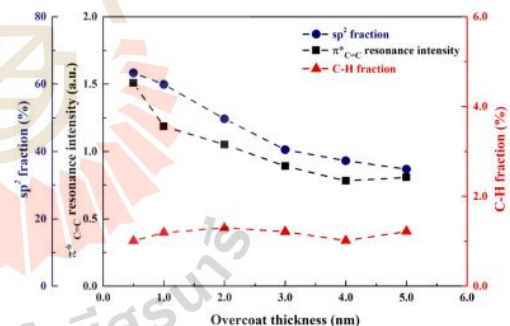


Fig. 5. The plot of the π^* resonance intensity, the sp^2 fraction, and C-H content deduced from the NEXAFS spectra as a function of ta-C overcoat thickness.

increased to 0.70 and 0.62, respectively. This resulted in a wear track observed in the optical images after the test.

3.3. Discussion

Fig. 8 shows the plot of Rq , I_D/I_G ratio estimate from Raman spectroscopy, sp^2 fraction estimated from NEXAFS, and COF of the DLC overcoats as a function of thickness. The plot shows that the sp^2 fraction

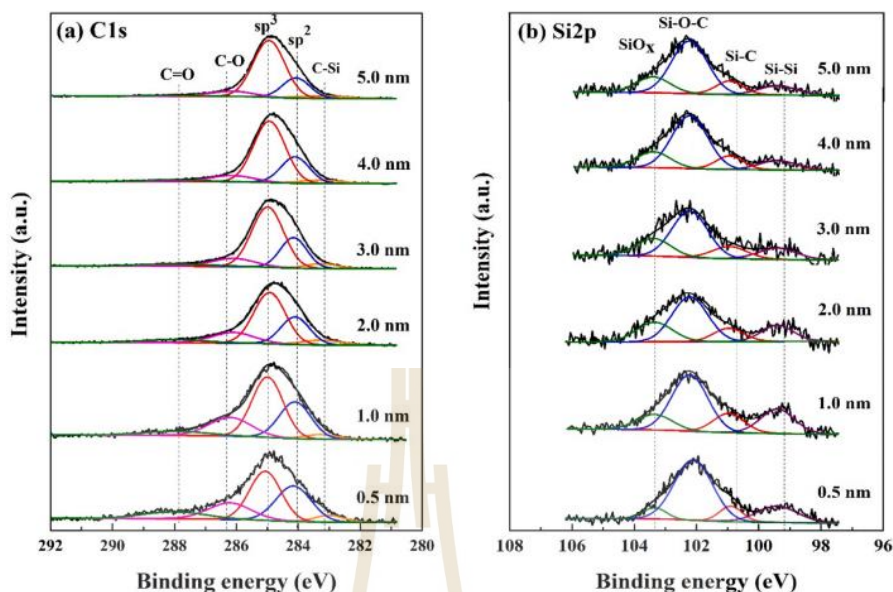


Fig. 6. High-resolution XPS spectra with deconvolution of (a) C1s and (b) Si2p peaks of the DLC overcoats with thicknesses of 0.5–5.0 nm.

Table 2

Relative atomic percentages of carbon bonds estimated from C1s peak.

Overcoat	Relative atomic percentage (%)					
	C-Si	sp ²	sp ³	C-O	C=O	sp ³ /(sp ³ + sp ²)
0.5 nm	5.16	29.55	36.64	18.16	10.49	55.36
1.0 nm	4.04	27.11	42.90	18.83	6.12	61.28
2.0 nm	6.19	24.15	49.24	14.54	5.88	67.09
3.0 nm	4.69	23.66	55.92	10.80	4.93	70.27
4.0 nm	4.46	23.24	60.96	8.17	3.17	72.27
5.0 nm	4.83	20.17	64.90	8.45	1.65	76.29

of the DLC overcoats strongly correlates to their thickness. It increases as the overcoat thickness decreases, which is consistent with the rise of the I_D/I_G ratio observed from Raman spectroscopy. The formation of a DLC film fabricated by the PFCVA technique can be explained by the subplantation model [3,59,60]. The PFCVA utilizes a plasma of highly energetic carbon ions that can embed themselves into a growing film. The generated carbon ions can penetrate the surface, leading to carbon densification in the subsurface and the formation of sp^3 hybridization. The formation of sp^3 hybridization is strongly determined by the carbon ion energy and growth temperature [3,60]. The film is grown in three cross-sectional layers: interface, bulk, and surface layers [3,14,30]. The interface and surface layers have a high sp^2 fraction, while the bulk layer possesses a high sp^3 fraction. The spatially resolved cross-sectional electron energy loss spectroscopy (EELS) study reported the existence of a thin surface layer with a high sp^2 fraction, which has a thickness varied from 0.4 nm and 1.3 nm for carbon ion energy of 35 eV and 320 eV, respectively [3,60]. It is also shown that the high sp^2 bonds surface layer does not form after the film growth but instead is present during the development of the high sp^3 bonded bulk layer [3]. As the film grows, the bottom part of the surface layer is converted into sp^3 hybridization by the subsurface deposition process, and the top of the sp^2 bonded surface layer expands away from the substrate. Our result seems to be in good agreement with the assumption. It was expected that the

ultrathin DLC overcoats with thicknesses of between 0.5–1.0 nm would mainly compose of surface and interface layers with high sp^2 fraction. As the deposition parameters, specifically ion beam energy and substrate temperature, were kept consistent in the growth process, the characteristics of the surface and interface layers would not change when the overcoat thickness was varied. When the overcoat thickness increased, the dense bulk layer with a high sp^3 fraction was formed and expanded, while the surface and interface layers remained unchanged. As a result, the sp^3 fraction increased with increasing thickness. The increase of sp^2 fraction with decreasing thickness has a strong correlation with the tribology properties of the overcoat. The rise of the sp^2 fraction and decrease of the sp^3 fraction reduces the toughness of the overcoat and significantly increase the COF [18].

The R_q of the ultrathin DLC films, alternately, was found to be strongly influenced by the morphology of the substrate. It tended to follow the surface roughness evolution for the general case [61]. This behavior has also been reported and explained by Zhong *et al.* [62]. In the first stage of the growth, the deposited carbon atoms arrive (condensation), migrate (diffusion), and aggregate into two-dimensional adatom islands (nucleation) on the surface. The deposited ions prefer to settle at adsorption sites on the bottom of valleys on the surface as their areas are more stable than other positions, resulting in the smoothness of the surface [62,63]. It was observed in this work that after the deposition of the DLC overcoat with a thickness of 0.5 nm, the surface of the Si interlayer with R_q of 0.262 nm became smoother with R_q of 0.195 nm. As the surface becomes smoother, a series of islands is formed due to the aggregation of carbon atoms at the valley in the initial smoothing stage, resulting in quickly increased surface roughness. The R_q increased to 0.227 nm was observed for the overcoat thickness of 1.0 nm. As the island coalesces to form a closed and continuous film, the surface roughness reaches the maximum and then decreases in the second stage. The surface roughness becomes constant in the third stage and gradually increases above a rough transition. The R_q gradually declined and became steady at approximately 0.126 nm for the overcoat thickness greater than 2.0 nm. The observed evolution of surface

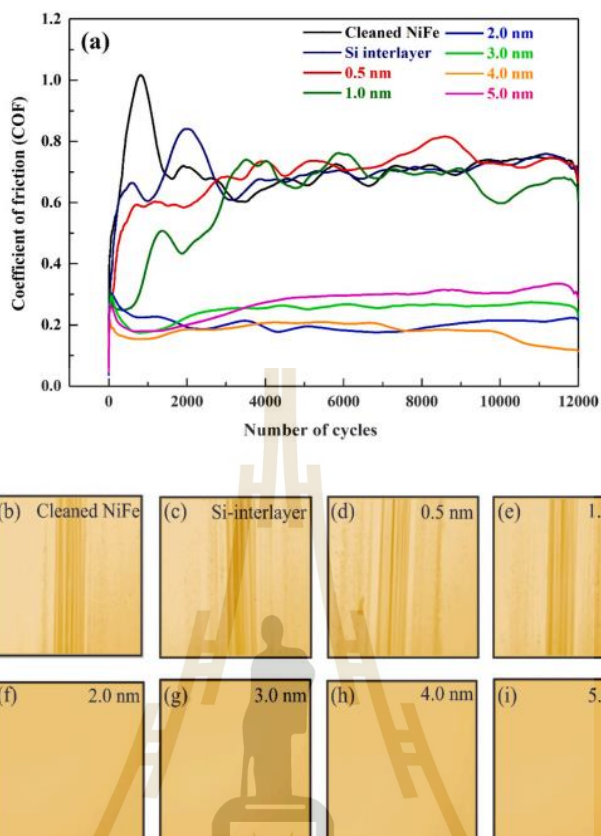


Fig. 7. (a) Friction curves and (b) – (i) optical images after the ball-on-disk test of NiFe substrate, Si-interlayer deposited on the substrate, and the DLC overcoats with thicknesses of 0.5 – 5.0 nm.

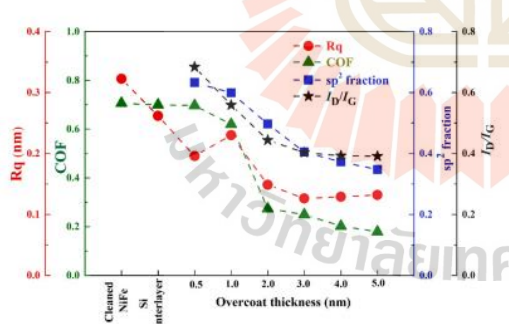


Fig. 8. The plot of Rq, I_D/I_G ratio, sp^2 fraction estimated from NEXAFS, and COF as a function of overcoats thickness.

morphology with thickness is also consistent with the overcoat structure as it is shown that the bulk overcoat with high sp^3 bonded carbon has not been completely formed for the thickness of 0.5–1.0 nm. This result suggests that the initial roughness may also affect the formation and

evolution of a high sp^3 fraction bulk layer with overcoat thickness.

4. Conclusions

This work reports a comprehensive investigation of the chemical structure, surface morphology, and tribology of ultrathin DLC overcoats with a thickness of between 0.5 – 5.0 nm using the PFCVA technique. The DLC overcoats were fabricated on a NiFe alloy base substrate with a Si interlayer. The overcoat thicknesses were accurately determined by the WDXRF and HRTEM techniques. The surface morphology and chemical structure were investigated by the AFM, XPS, NEXAFS, and Raman spectroscopy techniques. Additionally, the tribological properties were evaluated by the reciprocating wear test. The AFM results indicated that the fabricated ultrathin DLC overcoats had an ultra-smooth surface with an Rq of below 0.23 nm. The XPS revealed that the overcoats had high sp^3 bonds fraction in a range of 55.36 – 76.29%. The NEXAFS and Raman spectroscopy showed that sp^2 bonds fraction and I_D/I_G ratio increased with decreasing thickness and suddenly increased as the overcoat thickness reached 1 nm, indicating a rise in COF. The correlation between sp^2 bonds fraction and overcoat thickness fabricated in this work was explained by the subplantation model. The results demonstrated the limitation of the thickness of the DLC overcoat fabricated by the PFCVA technique as a protective coating for high-density

magnetic storage devices.

Declaration of Competing Interest

None.

Acknowledgments

This material is based upon work supported by Suranaree University of Technology (SUT), External Grants and Scholarships for Graduate Students (contact no. 74/2559), Seagate Technology (Thailand), and Synchrotron Light Research Institute (Public Organization), Thailand, National Nanotechnology Center (NANOTEC), National Science and Technology Development Agency (NSTDA), and Ministry of Higher Education, Science, Research, and Innovation (MHESI), Thailand, through its program of Research Network NANOTEC for partial financial support. The authors would like to express gratitude for the assistance of the staff at the BL3.2UB: PEEM and BL5.3: SUT-NANOTEC-SLRI XPS of the SLRI and Frontier Research Center (F.R.C.) at VISTEC.

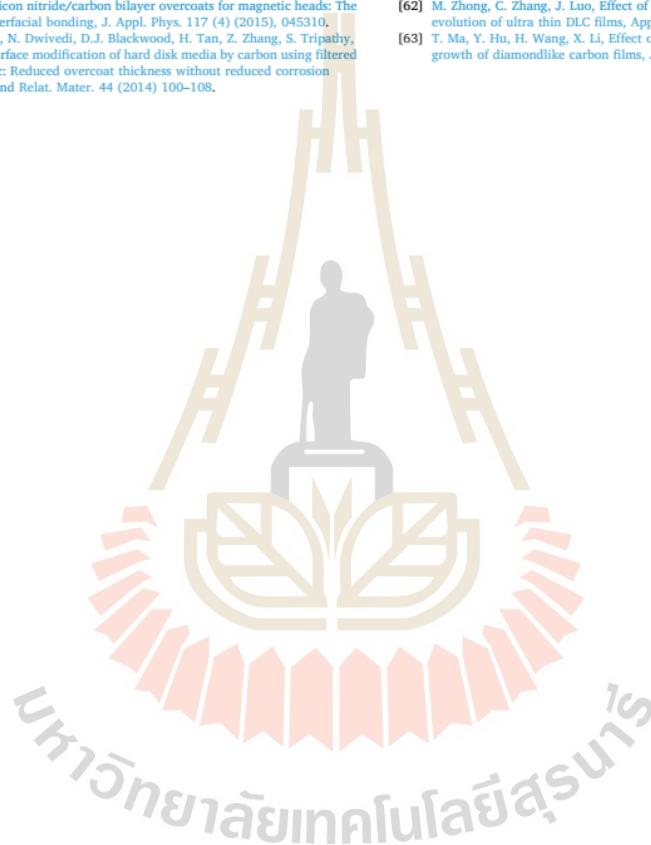
Supplementary materials

Supplementary material associated with this article can be found, in the online version, at doi:10.1016/j.mta.2022.101650.

Reference

- C. Casiraghi, J. Robertson, A.C. Ferrari, Diamond-like carbon for data and beer storage, *Mater. Today* 10 (1-2) (2007) 44–53.
- C. Casiraghi, A.C. Ferrari, J. Robertson, R. Ohr, M.v. Gradowski, D. Schneider, H. Hilgers, Ultra-thin carbon layer for high density magnetic storage devices, *Diamond Relat. Mater.* 13 (4-8) (2004) 1480–1485.
- C. Davis, G. Amarantunga, K. Knowles, Growth mechanism and cross-sectional structure of tetrahedral amorphous carbon thin films, *Phys. Rev. Lett.* 80 (15) (1998) 3280.
- A.C. Ferrari, J. Robertson, Resonant Raman spectroscopy of disordered, amorphous, and diamondlike carbon, *Phys. Rev. B* 64 (7) (2001).
- A.C. Ferrari, Diamond-like carbon for magnetic storage disks, *Surf. Coat. Technol.* 180 (2004) 190–206.
- M. Moseler, P. Gumbsch, C. Casiraghi, A.C. Ferrari, J. Robertson, The ultra-smoothness of diamond-like carbon surfaces, *Science* 309 (5740) (2005) 1545–1548.
- C.S. Lee, J.-K. Shin, K.Y. Eun, K.-R. Lee, K.H. Yoon, Defect density and atomic bond structure of tetrahedral amorphous carbon (ta-C) films prepared by filtered vacuum arc process, *J. Appl. Phys.* 95 (9) (2004) 4829–4832.
- N. Dwivedi, R.J. Yeo, Z. Zhang, C. Dhand, S. Tripathy, C.S. Bhatia, Direct observation of thickness and foreign interlayer driven abrupt structural transformation in ultrathin carbon and hybrid silicon nitride/carbon films, *Carbon* 115 (2017) 701–719.
- N. Wang, K. Komvopoulos, F. Rose, B. Marchon, Structural stability of hydrogenated amorphous carbon overcoats used in heat-assisted magnetic recording investigated by rapid thermal annealing, *J. Appl. Phys.* 113 (8) (2013), 083517.
- N. Dwivedi, A. Ott, K. Sasikumar, C. Dou, R. Yeo, B. Narayanan, U. Sassi, D. De Fazio, G. Soavi, T. Dutta, Graphene overcoats for ultra-high storage density magnetic media, *Nat. Commun.* 12 (1) (2021) 1–13.
- M. Zhong, C. Zhang, J. Luo, X. Lu, The protective properties of ultra-thin diamond like carbon films for high density magnetic storage devices, *Appl. Surf. Sci.* 256 (1) (2009) 322–328.
- N. Soin, S.S. Roy, S.C. Ray, P. Lemoine, M.A. Rahman, P.D. Maguire, S.K. Mitra, J. A. McLaughlin, Thickness dependent electronic structure of ultra-thin tetrahedral amorphous carbon (ta-C) films, *Thin. Solid. Films* 520 (7) (2012) 2909–2915.
- T.R. Albrecht, H. Arora, V. Ayanoor-Vitikkate, J.-M. Beaujour, D. Bedau, D. Berman, A.L. Bogdanov, Y.-A. Chapuis, J. Cushen, E.E. Dobisz, Bi-patterned magnetic recording: Theory, media fabrication, and recording performance, *IEEE Trans. Magn.* 51 (5) (2015) 1–42.
- J. Matlak, K. Komvopoulos, Ultrathin amorphous carbon films synthesized by filtered cathodic vacuum arc used as protective overcoats of heat-assisted magnetic recording heads, *Sci. Rep.* 8 (1) (2018) 1–11.
- B. Marchon, T. Pitchford, Y.-T. Hsia, S. Gangopadhyay, The head-disk interface roadmap to an areal density of Tbit/in², *Advances in Tribology* 2013, 2013.
- N. Wang, K. Komvopoulos, Thermal stability of ultrathin amorphous carbon films for energy-assisted magnetic recording, *IEEE Trans. Magn.* 47 (9) (2011) 2277–2282.
- H.-S. Zhang, K. Komvopoulos, Synthesis of ultrathin carbon films by direct current filtered cathodic vacuum arc, *J. Appl. Phys.* 105 (8) (2009), 083305.
- P.S. Goopattader, N. Dwivedi, E. Rismani-Yazdi, N. Satyanarayana, R.J. Yeo, S. Kundu, C.S. Bhatia, Probing the role of C+ ion energy, thickness and graded structure on the functional and microstructural characteristics of ultrathin carbon films (< 2 nm), *Tribol. Int.* 81 (2015) 73–88.
- E. Rismani, S. Sinha, H. Yang, C. Bhatia, Effect of pretreatment of Si interlayer by energetic C+ ions on the improved nanotribological properties of magnetic head overcoat, *J. Appl. Phys.* 111 (8) (2012), 084902.
- N. Dwivedi, N. Satyanarayana, R.J. Yeo, H. Xu, K.P. Loh, S. Tripathy, C.S. Bhatia, Ultrathin carbon with interspersed graphene/fullerene-like nanostructures: a durable protective overcoat for high density magnetic storage, *Sci. Rep.* 5 (1) (2015) 1–16.
- M.G. Beghi, A.C. Ferrari, K.B.K. Teo, J. Robertson, C.E. Bottani, A. Libassi, B. K. Tanner, Bonding and mechanical properties of ultrathin diamond-like carbon films, *Appl. Phys. Lett.* 81 (20) (2002) 3804–3806.
- F. Cemin, L. Bim, C. Menezes, M.M. da Costa, I. Baumvol, F. Alvarez, C. Figueroa, The influence of different silicon adhesion interlayers on the tribological behavior of DLC thin films deposited on steel by EC-PECVD, *Surf. Coat. Technol.* 283 (2015) 115–121.
- F. Liu, H. Ma, C. Tang, Si seed layer thickness effect on the structure of ultrathin tetrahedral amorphous carbon films, *Surf. Coat. Technol.* 235 (2013) 117–120.
- T. Yamamoto, H. Hyodo, S. Tsuchitani, R. Kaneko, Ultrathin amorphous carbon overcoats by filtered cathodic arc deposition, *IEEE Trans. Magn.* 39 (5) (2003) 2201–2204.
- J. Vetter, 60 years of DLC coatings: historical highlights and technical review of cathodic arc processes to synthesize various DLC types, and their evolution for industrial applications, *Surf. Coat. Technol.* 257 (2014) 213–240.
- H. Takahara, Thickness and composition analysis of thin film samples using FP method by XRF analysis, *Rigaku J.* 33 (2017) 17–21.
- J. Stöhr, NEXAFS spectroscopy, Springer Science & Business Media, 2013.
- F. Mangolini, J.B. McClimon, R.W. Carpick, Quantitative evaluation of the carbon hybridization state by near edge X-ray absorption fine structure spectroscopy, *Anal. Chem.* 88 (5) (2016) 2817–2824.
- S. Hüfner, Photoelectron spectroscopy: principles and applications, Springer Science & Business Media, 2013.
- C. Casiraghi, A. Ferrari, R. Ohr, D. Chu, J. Robertson, Surface properties of ultrathin tetrahedral amorphous carbon films for magnetic storage technology, *Diamond Relat. Mater.* 13 (4-8) (2004) 1416–1421.
- A.C. Ferrari, J. Robertson, Interpretation of Raman spectra of disordered and amorphous carbon, *Phys. Rev. B* 61 (20) (2000) 14095.
- F.-X. Liu, Z.-L. Wang, Thickness dependence of the structure of diamond-like carbon films by Raman spectroscopy, *Surf. Coat. Technol.* 203 (13) (2009) 1829–1832.
- A.C. Ferrari, Determination of bonding in diamond-like carbon by Raman spectroscopy, *Diamond Relat. Mater.* 11 (3-6) (2002) 1053–1061.
- J. Birrell, J. Gerbi, O. Auciello, J. Gibson, D. Gruen, J. Carlisle, Bonding structure in nitrogen doped ultrananocrystalline diamond, *J. Appl. Phys.* 93 (9) (2003) 5606–5612.
- B. Watts, L. Thomsen, P. Dastoor, Methods in carbon K-edge NEXAFS: Experiment and analysis, *J. Electron Spectrosc. Relat. Phenom.* 151 (2) (2006) 105–120.
- G.A. Abbas, S.S. Roy, P. Papakonstantinou, J.A. McLaughlin, Structural investigation and gas barrier performance of diamond-like carbon based films on polymer substrates, *Carbon* 43 (2) (2005) 303–309.
- F. Mangolini, Z. Li, M.A. Marcus, R. Schneider, M. Dienwiebel, Quantification of the carbon bonding state in amorphous carbon materials: A comparison between EELS and NEXAFS measurements, *Carbon* 173 (2021) 557–564.
- F. Mangolini, B.A. Krick, T.D. Jacobs, S.R. Khanal, F. Streller, J.B. McClimon, J. Hilbert, S.V. Prasad, T.W. Scharf, J.A. Ohlhausen, Effect of silicon and oxygen dopants on the stability of hydrogenated amorphous carbon under harsh environmental conditions, *Carbon* 130 (2018) 127–136.
- T. Hemraj-Benny, S. Banerjee, S. Sambasivan, M. Balasubramanian, D.A. Fischer, G. Eres, A.A. Puzosky, D.B. Geohegan, D.H. Lowndes, W. Han, Near-edge X-ray absorption fine structure spectroscopy as a tool for investigating nanomaterials, *Small* 2 (1) (2006) 26–35.
- Y.V. Fedoseeva, G. Pondnyakov, A. Okotrub, M. Kanygin, Y.V. Nastaushev, O. Vilkov, L. Bulshcheva, Effect of substrate temperature on the structure of amorphous oxygenated hydrocarbon films grown with a pulsed supersonic methane plasma flow, *Appl. Surf. Sci.* 385 (2016) 464–471.
- K.G. Latham, M.I. Simone, W.M. Dose, J.A. Allen, S.W. Donne, Synchrotron based NEXAFS study on nitrogen doped hydrothermal carbon: Insights into surface functionalities and formation mechanisms, *Carbon* 114 (2017) 566–578.
- A.V. Sumant, P. Gilbert, D.S. Grierson, A.R. Konicsek, M. Abrecht, J.E. Butler, T. Feygelson, S.S. Rotter, R.W. Carpick, Surface composition, bonding, and morphology in the nucleation and growth of ultra-thin, high quality nanocrystalline diamond films, *Diamond Relat. Mater.* 16 (4-7) (2007) 718–724.
- K.D. Koshigan, F. Mangolini, J.B. McClimon, B. Vacher, S. Bec, R.W. Carpick, J. Fontaine, Understanding the hydrogen and oxygen gas pressure dependence of the tribological properties of silicon oxide-doped hydrogenated amorphous carbon coatings, *Carbon* 93 (2015) 851–860.
- A. Wada, T. Ogaki, M. Niibe, M. Tagawa, H. Saitoh, K. Kanda, H. Ito, Local structural analysis of a-SiC:H films formed by decomposition of tetramethylsilane in microwave discharge flow of Ar, *Diamond Relat. Mater.* 20 (3) (2011) 364–367.
- F. Mangolini, J.B. McClimon, F. Rose, R.W. Carpick, Accounting for nanometer-thick adventitious carbon contamination in X-ray absorption spectra of carbon-based materials, *Anal. Chem.* 86 (24) (2014) 12258–12265.
- J. Sedlmair, S.-C. Gleber, C. Peth, K. Mann, J. Niemeier, J. Thieme, Characterization of refractory organic substances by NEXAFS using a compact X-ray source, *J. Soils Sediment.* 12 (1) (2012) 24–34.

- [47] D.M. DeLongchamp, E.K. Lin, D.A. Fischer, Organic semiconductor structure and chemistry from near-edge X-ray absorption fine structure (NEXAFS) spectroscopy, *Organic Field-Effect Transistors IV*, Int. Soc. Opt. Photon. (2005) 59400A.
- [48] S. Roy, R. McCann, P. Papakonstantinou, J. McLaughlin, I. Kirkman, S. Bhattacharyya, S. Silva, Near edge X-Ray absorption fine structure study of aligned π -bonded carbon structures in nitrogenated ta-C films, *J. Appl. Phys.* 99 (4) (2006), 043511.
- [49] M. Dienwiebel, M.-I.D.B. Bouchet, *Advanced Analytical Methods in Tribology*, Springer, 2018.
- [50] J. Lomon, P. Chaiyabin, T. Saisopa, K. Seawsakul, N. Saowiang, K. Promsakha, P. Poolcharuansin, N. Pasaja, A. Chingsungnoen, R. Supruangnet, XPS and XAS preliminary studies of diamond-like carbon films prepared by HiPIMS technique, *J. Phys. Conf. Ser.* (2018), 012048.
- [51] N. Dwivedi, E. Rismani-Yazdi, R.J. Yeo, P.S. Goohpattader, N. Satyanarayana, N. Srinivasan, B. Druz, S. Tripathy, C. Bhatia, Probing the role of an atomically thin SiN_x interlayer on the structure of ultrathin carbon films, *Sci. Rep.* 4 (1) (2014) 1–10.
- [52] E. Rismani, M.A. Samad, S.K. Sinha, R. Yeo, H. Yang, C.S. Bhatia, Ultrathin Si/C graded layer to improve tribological properties of Co magnetic films, *Appl. Phys. Lett.* 101 (19) (2012), 191601.
- [53] R.J. Yeo, N. Dwivedi, L. Zhang, Z. Zhang, C.Y. Lim, S. Tripathy, C.S. Bhatia, Durable ultrathin silicon nitride/carbon bilayer overcoats for magnetic heads: The role of enhanced interfacial bonding, *J. Appl. Phys.* 117 (4) (2015), 045310.
- [54] R.J. Yeo, E. Rismani, N. Dwivedi, D.J. Blackwood, H. Tan, Z. Zhang, S. Tripathy, C. Bhatia, Bi-level surface modification of hard disk media by carbon using filtered cathodic vacuum arc: Reduced overcoat thickness without reduced corrosion performance, *Diamond Relat. Mater.* 44 (2014) 100–108.
- [55] Y. Wang, M. Moitreyee, R. Kumar, L. Shen, K. Zeng, J. Chai, J. Pan, A comparative study of low dielectric constant barrier layer, etch stop and hardmask films of hydrogenated amorphous Si-(C, O, N), *Thin. Solid. Film.* 460 (1-2) (2004) 211–216.
- [56] W. Choi, T. Ong, L. Tan, F. Loh, K. Tan, Infrared and x-ray photoelectron spectroscopy studies of as-prepared and furnace-annealed radio-frequency sputtered amorphous silicon carbide films, *J. Appl. Phys.* 83 (9) (1998) 4968–4973.
- [57] C. Önneby, C.G. Pantano, Silicon oxycarbide formation on SiC surfaces and at the SiC/SiO₂ interface, *J. Vac. Sci. Technol. A: Vac. Surface. Film.* 15 (3) (1997) 1597–1602.
- [58] S. Gallis, M. Huang, H. Efstathiadis, E. Eisenbraun, A.E. Kaloyeros, E.E. Nyein, U. Hommerich, Photoluminescence in erbium doped amorphous silicon oxycarbide thin films, *Appl. Phys. Lett.* 87 (9) (2005), 091901.
- [59] J. Robertson, Diamond-like amorphous carbon, *Mater. Sci. Eng. R Rep.* 37 (4-6) (2002) 129–281.
- [60] Y. Lifshitz, G. Lempert, E. Grossman, Substantiation of subplantation model for diamondlike film growth by atomic force microscopy, *Phys. Rev. Lett.* 72 (17) (1994) 2753.
- [61] C. Casiraghi, A. Ferrari, J. Robertson, The smoothness of tetrahedral amorphous carbon, *Diamond Relat. Mater.* 14 (3-7) (2005) 913–920.
- [62] M. Zhong, C. Zhang, J. Luo, Effect of substrate morphology on the roughness evolution of ultra thin DLC films, *Appl. Surf. Sci.* 254 (21) (2008) 6742–6748.
- [63] T. Ma, Y. Hu, H. Wang, X. Li, Effect of impact angle and substrate roughness on growth of diamondlike carbon films, *J. Appl. Phys.* 101 (1) (2007), 014901.



CURRICULUM VITAE

Name: Warintorn Chatarat

Date of birth: August 1, 1973

Education:

2516 – Present Ph.D. in Physics. School of Physics, SUT

1993 – 1996 B.Sc. in Physics. Department of Physics, PSU

Publication:

W. Chatarat, N. Chanlek, C. Euaruksakul, H. Nakajima, J. Rusamiputi, S. Ittisanronnachai, N. Konkhunthot, S. Rujirawat, P. Songsiriritthigul, R. Yimnirun, MTLA 27 (2023) 101650

Position and Place of Work:

2016 – Present Senior manager engineering at Seagate Technology (Thailand) Ltd.

2010 – 2016 Staff process engineering at Seagate Technology (Thailand) Ltd.